Molecular Dynamics Simulation of Biomembrane Systems

by

Wei Ding

School of Engineering and Materials Science
Queen Mary University of London

Submitted in partial fulfillment of the
requirements of the Degree of Doctor of Philosophy

2017

Statement of Originality

I, Wei Ding, confirm that the research included within this thesis is my own work or that where it has been carried out in collaboration with, or supported by others, that this is duly acknowledged below and my contribution indicated. Previously published material is also acknowledged below.

I attest that I have exercised reasonable care to ensure that the work is original, and does not to the best of my knowledge break any UK law, infringe any third partys copyright or other Intellectual Property Right, or contain any confidential material.

I accept that the College has the right to use plagiarism detection software to check the electronic version of the thesis.

I confirm that this thesis has not been previously submitted for the award of a degree by this or any other university.

The copyright of this thesis rests with the author and no quotation from it or information derived from it may be published without the prior written consent of the author.

Signature:

Date: 21^{st}, September, 2017

Abstract

The fundamental structure of all biological membranes is the lipid bilayer. Attributed to the multifaceted features of lipids and its dynamical interaction with other membrane-integrated molecules, the lipid bilayer is involved in a variety of physiological phenomena such as transmembrane transportation, cellular signalling transduction, energy storage, etc. Due to the nanoscale but high complexity of the lipid bilayer system, experimental investigation into many important processes at the molecular level is still challenging. Molecular dynamics (MD) simulation has been emerging as a powerful tool to study the lipid membrane at the nanoscale. Utilizing atomistic MD, we have quantitatively investigated the effect of lamellar and nonlamellar lipid composition changes on a series of important bilayer properties, and how membranes behave when exposed to a high-pressure environment. A series of membrane properties such as lateral pressure and dipole potential profiles are quantified. Results suggest the hypothesis that compositional changes, involving both lipid heads and tails, modulate crucial mechanical and electrical features of the lipid bilayer, so that a range of biological phenomena, such as the permeation through the membrane and conformational equilibria of membrane proteins, may be regulated. Furthermore, water also plays an essential role in the biomembrane system. To balance accuracy and efficiency in simulations, a coarse-grained ELBA water model was developed. Here, the ELBA water model is stress tested in terms of temperature- and pressure-related properties, as well as hydrating properties. Results show that the accuracy of the ELBA model is almost as good as conventional atomistic water models, while the computational efficiency is increased substantially.

Contents

List of Figures

List of Tables

Acknowledgements

The work in the four years is concentrated in this thesis, but this is definitely not all for my PhD. I would like to thank everyone and everything occurred in the past four years, that helped my every bit progress.

I am most grateful to my supervisors, Dr Mario Orsi and Professor Wen Wang. I still remember the first talk we had, in the telephone interview that gave me the chance to come to London. I feel lucky to be supervised by both of you. Without your guidance and support, it would be impossible to finish the PhD. Your wisdom, patience, enthusiasm, and responsibility inspired me, and I will set what I learned from you as the role model in my entire life.

I appreciate the unforgettable time in London. This is due to the people whom I spent the time together with. Michalis, thank you for the unselfish help in the office, as well as in the trips to Trieste and Manchester; Ganesh, thank you for the fun in our daily talk, and your Indian snacks; also everyone else in the office, thanks for the wonderful workplace made up by all of you.

Finally, I dedicated this thesis to my family in China, especially my fiancée Linwei, for the valuable support and understanding.

Chapter 1

Introduction

The fundamental structure of all biological membranes is the lipid bilayer, which encapsulates cells as well as the cell nucleus and intracellular organelles. Figure 1.1 gives a schematic example of the plasma membrane [49]. The external environment and the cell interior are separated by the bimolecular layer formed by lipids. Other components such as proteins and carbohydrates are also embedded in the lipid membrane. At the first glance, the lipid bilayer may appear to be a simple dual-layer

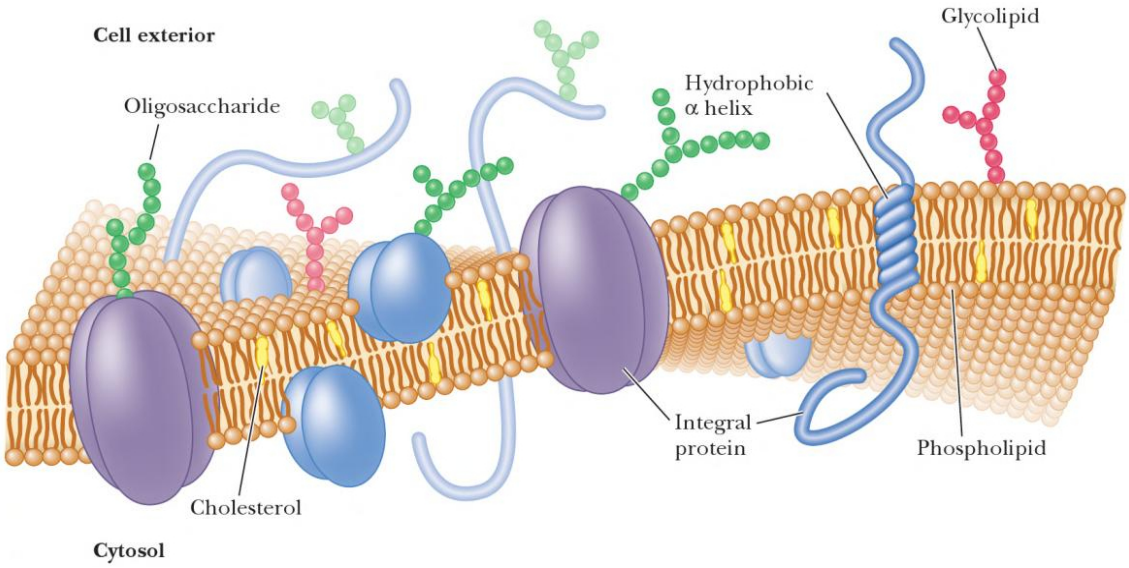

Figure 1.1: Schematic model of the biological membrane [49]. A lipid bilayer forms the basic structure, with membrane proteins embedded.

structure replicates regularly. Yet in reality, it is characterized by high dynamics and complexity. Notably, lipid membranes in their biological states are fluid soft interfaces, organized through the self-assembling process [228]. Compared to other biosystems, in contrast to the strong chemical forces that maintain typical protein or DNA chains, such an entropy-driven aggregation endues substantial disorder in the bilayer. Furthermore, an enormous lipid diversity is present in biomembranes. As a result, the function of a lipid bilayer is not only limited to cellular compartmentalization. Attributed to the multifaceted features of lipids and their dynamical interactions with other membrane-integrated molecules (such as enzymes, transporters, or signalling molecules), the lipid bilayer is also involved in a variety of physiological phenomena such as transmembrane transportation, cellular signalling transduction, energy storage, etc [81, 104, 197].

A comprehensive knowledge about the bilayer membrane is essential to understand the living world. Molecular-level structure and mechanics of lipid bilayers fundamentally determine the shape, stability, and metabolism of cells [350, 356]. The lipid membrane also represents as a platform on which numerous important biochemical processes are carried out [35, 189, 211]. The conformation, and thereby the functionality, of embedded membrane proteins can be influenced though their interactions with neighbouring lipid molecules. Furthermore, nonspecific properties of the assembled bilayer (such as the transmembrane lateral pressure distribution) can also modulate the functional state of membrane proteins [78, 211, 264, 364]. Regarding biomedical applications, the self-assembling machinery of lipid membrane systems has its potential for the design of drug-delivery techniques [309].

Driven by the many fascinating features of the lipid membrane, researchers have been actively trying to reveal the physics and biological functions of lipid bilayers. Extensive progress has been achieved in the emerging field of "lipidomics" in recent years. However, due to the nanoscale but high complexity of the lipid bilayer system, investigations into many important membrane-relevant phenomena at the molecular level is still challenging. On one hand, for an object that is only several nanometres thick and characterized by high disorder and heterogeneity, novel experimental techniques are required for quantitative measurements on many lipid bilayer properties. On the other hand, with the lateral length scale spanning up to a thousand nanometres [228], the existence of lipid diversity further widens the gap

between the laboratory understanding about model membranes and the real-world principles governing the biomembranes.

Thanks to the development of computer science and technology over the past decades, the molecular dynamics (MD) simulation technique has been emerging as a powerful tool to study the lipid membrane at the nanoscale [347, 355]. Briefly, atomistic MD simulation models a biomolecular system by describing each atom and interactions between atoms with a set of interaction potential equations and associated parameters based on known biochemistry information. This set of equations and parameters is typically called the "forcefield". Based on the forcefield and the classic Newtonian theory, a lipid membrane system can be simulated at appropriate temporal and spatial scales. From a well-designed molecular dynamics simulation, atomistic information and ensembled energetic or dynamics properties can be obtained, thus it can ideally complement laboratory investigations and predict properties that are not directly accessible by experiments.

One mystery about the biological membrane is why it is composed of such a diversity of lipid species and the lipid composition is dynamically regulated [227]. In particular, the natural inclusion of nonlamellar lipids in the overall lamellar biomembrane is of great research interests. Some local nonlamellar structures are required in biological processes such as cellular budding, fission or fusion [208]. Further hypotheses point to the modulating role of nonlamellar lipids through changes of key bilayer properties induced by them on functions of membranes and embedded proteins [227, 353]. However, molecular-scale insights of such mechanisms are lacking due to experimental challenges. Utilizing the MD simulation technique, we quantitatively investigated the effect of lamellar and nonlamellar lipid composition changes on a series of important bilayer properties. More specifically, the lamellar and nonlamellar families are represented by two prevalent lipid types, DOPC and DOPE, respectively. Obtained results are presented and discussed in Chapter 3. Another intriguing characteristics of lipids as biomembrane constituents is the unsaturation level in their hydrocarbon tails, which has been thought to contribute to the rigidity, micro-mechanics, and permeability of the lipid bilayer [120, 238, 375]. Especially when the membrane is exposed to a high pressure environment (which is of interest in understanding many biological processes such as barophilibility of deep-marine lifes as well as high-pressure pasteurization in the food industry [8, 175]), the response

of lipid membrane may depend on its unsaturation level. A quantitative study on this topic is presented in Chapter 4.

Beside lipids, water is also a non-negligible part of the biomembrane (as well as other biomolecular systems). Interactions between lipids and water molecules are thought to be responsible for the formation, maintenance, and dynamics of the bilayer structure [14, 15, 20]. In a typical atomistic-level simulation, water molecules usually account for a large proportion of total particle amount, thus contributing to a great extent to the behaviour of the simulated system and taking a majority of computational resources. To achieve higher efficiency and complexity, a great number of coarse-grained models have been developed [234, 296, 366], aiming at simplification while keeping as much accuracy as possible. Among them, the ELBA water model has been proved to successfully strike a balance between efficiency and the ability to reproduce bulk water fundamental properties [242, 248]. Extended work to further test the capability of the ELBA water model are presented in Chapter 5 and Chapter 6. Chapter 5 investigates into temperature-/pressure-related properties of the ELBA water, including the liquid density and self-diffusion coefficient at temperatures from 268 K to 378 K and pressures from 1 atm up to 4000 atm, and the isothermal compressibility, isobaric heat capacity, and thermal expansion at ambient conditions which reflect the response to pressure or temperature fluctuations. In Chapter 6, hydration features of the ELBA water as a direct solvent for atomistic solutes are studied. More specifically, ELBA is applied to solve representative $\alpha-$helical and $\beta-$hairpin structures directly (i.e. no additional or *ad hoc* scaling factors, intermediate regions, or extra sites are introduced), and then folding free energy landscapes of the two protein structures are measured and compared with performance of the all-atom TIP3P water model. The parallel tempering technique [338] is applied for the free energy calculation, technical details of which will be briefly reviewed in Section 2.2.

Publication details for the work presented in each Chapter are listed below:

- Chapter 3:

  Wei Ding, Michail Palaiokostas, Wen Wang, and Mario Orsi, Effects of Lipid Composition on Bilayer Membranes Quantified by All-Atom Molecular Dynamics. *The Journal of Physical Chemistry B*, 2015, 119 (49), pp 15263-

15274.

- Chapter 4:

  Wei Ding, Michail Palaiokostas, Ganesh Shane, Wen Wang, and Mario Orsi, Effects of high pressure on phospholipid bilayers. *The Journal of Physical Chemistry B*, accepted, 2017, DOI: 10.1021/acs.jpcb.7b07119.

- Chapter 5:

  Wei Ding, Michail Palaiokostas, and Mario Orsi, Stress testing the ELBA water model. *Molecular Simulation*, 2016, 42, 337.

- Chapter 6:

  Mario Orsi, **Wei Ding**, and Michail Palaiokostas, Direct mixing of atomistic solutes and coarse-grained water. *Journal of Chemical Theory and Computation*, 2014, 10, 4684.

Chapter 2

Background

2.1 Lipids and biomembranes

Lipids are defined as a group of substances that are water-insoluble but highly soluble in organic solvents [101], which cover a broad range of molecules exhibiting wide diversity in structure and biological function. In living organisms, these different categories of lipids appear mostly to be organized in the bilayer structure, contributing to the versatile mechanical, electrical and dynamical properties of biomembranes.

2.1.1 Membrane lipids classification

As membrane constituents, lipids can be classified into three major types: phospholipids, glycolipids and sterols. Firstly, the phospholipids, especially glycerophospholipids, are found to be the most abundant in natural membranes [356]. A phospholipid molecule is constructed based on a phosphate attached to different organic moieties, comprising various hydrophilic "head" groups (like phosphatidylcholine (PC), phosphatidylethanolamine (PE) or phosphatidic acid (PA)). On the other side, the phosphate is connected with a "platform" to which one or more hydrocarbon chains are linked, together forming the hydrophobic "tails" of the lipid. For glycerophospholipids (also known as phosphoglycerides), the platform is glycerol. If the platform is sphingosine, the phospholipid is known as sphingophospholipid. The hydrocarbon tails of the lipids can be also varied in terms of length and degree

of unsaturation[1], extending the diversity in the family of phospholipids. Figure 2.1a and 2.1b give two examples of glycerophospholipid and sphingophospholipid, respectively. In the work presented in this thesis, the phospholipid species is the main object studied, and hence it will be the main focus in the following sections.

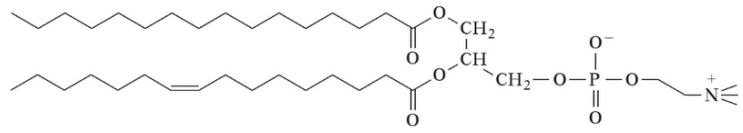

(a) Glycerophospholipid

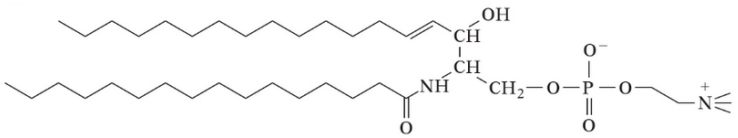

(b) Sphingophospholipid

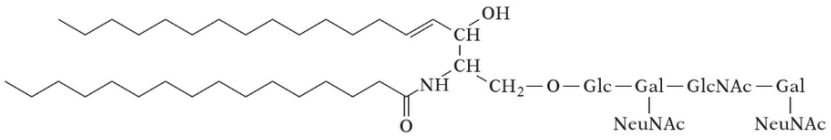

(c) Glycolipid

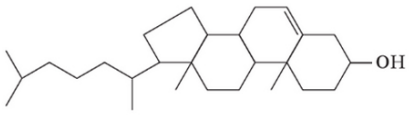

(d) Cholesterol

Figure 2.1: Structure of typical membrane lipids [197].

Glycolipids, as the name indicates, are sugar-containing lipids. Compared with phospholipids, their head groups are one or more sugar residues instead of the phosphatic one (see Figure 2.1c for a typical glycolipid, ganglioside). Sometimes, lipids in which the fatty acyl chains are directly linked with a sugar backbone can also be observed, which are usually named as saccharolipids [101]. In plasma membranes, glycolipids are always distributed in the outer leaflet, with the sugar residues oriented

[1]For lipid, unsaturation means that one or more double bonds occur in the fatty acid chain.

to the extracellular side and exposed in the aqueous environment. This feature provides physiological importance; for example, some specific glycosphingolipids as antigens on human red blood cell surface participate in the determination of the ABO blood types.

Sterols, out of which cholesterol (Figure 2.1d) is most commonly found in mammalian membranes, have a basic structure that is quite different from the phospholipid and the glycolipids. In a typical molecule in the sterol family, four fused hydrocarbon rings carry a hydroxyl group and a alkyl tail on specific carbons at either side [226]. In membrane bilayers, the hydroxyl group of sterols always orients towards outside and interacts with nearby lipid headgroups. As an indispensable substance for life activities, cholesterol helps modulate the phases of biomembrane, and affects its diffusivity [219]. It is also an essential component of lipid "rafts", membrane microdomains believed to favour specific protein-protein interactions resulting in the activation of signalling cascades [326].

2.1.2 Self-assembly of lipids

Despite belonging to a very diverse family of molecules, membrane lipids possess a critical common characteristic: they are amphipathic molecules, containing both a hydrophobic and a hydrophilic moiety [32]. This intrinsic characteristic enables them to be arranged as the bimolecular sheet structure, composed of two hydrophilic layers on each side of the bilayer interacting with water, and a hydrophobic domain in between. The formation of a bilayer can happen spontaneously in aqueous environment, through the peculiar "self-assembly" process. The hydrophobic effect, which is the tendency that the hydrophobic parts of molecules prefer to interact with each other rather than with water, is the main driving force for the bilayer self-assembling [341]. From the entropic point of view, the hydrogen-bonding network in pure water maximizes the system entropy. When lipid molecules are put into water, the hydrogen bonds in water suffers and local ordering of water molecules surrounding lipid molecules increases. The hydrophobic effect acts to drive the apolar parts of lipid molecules packed together to minimize contact with water. More specifically, the lipid tails are closely packed in the interior of the bilayer to avoid the area exposed to water where a maximized entropy state can be reached. Also there

are electrostatic interactions between the lipid heads and water molecules [227]. All these forces from different origins together make the membrane structure stable, self-sealing and extensive along the bilayer plane.

Nonetheless in fact, not all lipids assemble into the bilayer phase when dispersed in an aqueous phase. Taking the PE lipid, one of the most common membrane phospholipid, as an example, it can form the inverse non-lamellar structure in certain conditions, in which the lipid headgroups sequester an inner aqueous core and the hydrophobic domains are oriented outward [95]. To a first approximation, the formation of this structure can be understood through the amphiphile shape (or shape-structure) hypothesis [197, 353] of lipid polymorphism, as illustrated in Figure 2.2. In the hypothesis, the phases that lipids adopt are determined by the

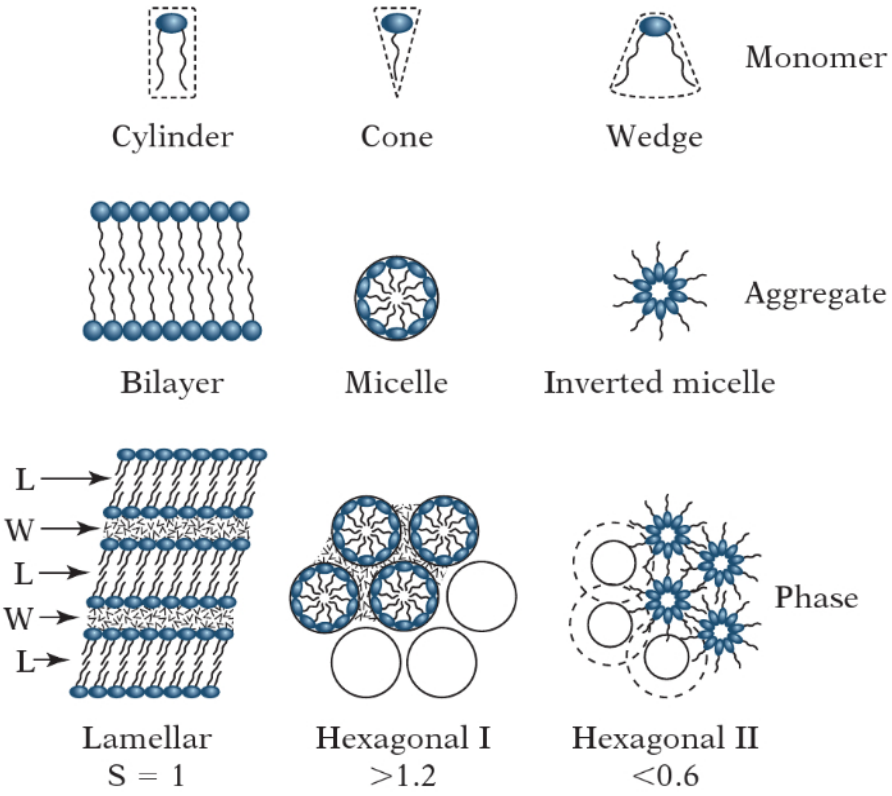

Figure 2.2: The lipid polymorphism explained by the amphiphile shape hypothesis [197]. S is the shape parameter; When $S = 1$, the lipid molecules are cylindrical and form lamellar phase (bilayer), and when $S > 1$ or $S < 1$, the lipids are organized into micelles, or inverse micelles.

effective shape of individual lipid molecules. Lipids like PC who self-assemble into lamellar phase have a cylindrical shape, in that the cross-sectional area of the headgroup is similar to that of the tail part. A shape parameter, S, can be defined as the ratio of the headgroup cross-sectional area a multiplied by the lipid length l to the lipid volume v ($S = \frac{a \cdot l}{v}$). If a lipid is conical ($S > 1$) or wedged ($S < 1$) shape, non-lamellar phases will be formed. Environment parameters, such as temperature, hydration level, and pH, also account for more completely defining the shape concept [342].

Experimentally, a phase diagram for a lipid type (or a mixed system) can be drawn to reflect how the lipid adopts different phases depending on temperature, hydration level, and so on. As an example, Figure 2.3 shows the phase diagram for DOPE. The inverse hexagonal (H_{II}) phase is formed at all water concentrations above

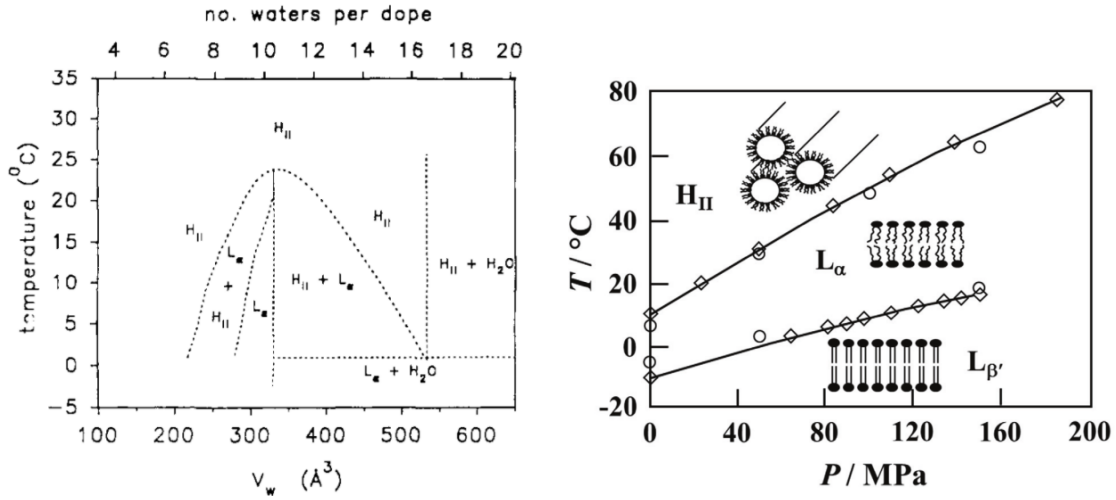

(a) (b)

Figure 2.3: Phase diagrams of DOPE-water system (a) as a function of temperature and water concentration [116], and (b) as a function of temperature and pressure [220]. Lipid phases: H_{II}: inverse hexagonal; L_α: lamellar liquid-crystalline (fluid-like); L_β: lamellar gel.

22°C, and below that an lamellar liquid-crystalline (L_α) phase occurs at intermediate water concentrations (Figure 2.3a) [116]. Then if in excess water, the transition from L_α phase to H_{II} phase happens at high temperatures and low pressures; also an additional lamellar $L_\alpha - to - L_\beta$ transition is exhibited at even lower temperatures (Figure 2.3b) [220]. Generally speaking, increasing the temperature will increase

the conformational disorder in the hydrocarbon chains of lipids, which tends to expand the interfacial area per lipid and leads to a tendency in a bilayer to bend towards the water region; increasing the water content tends to increase the repulsion between headgroups, which forces the chains to deviate away from their preferred conformational state and leads to a tendency to bend towards the chain region.

Biologically, the most important phase is the L_α phase, which is characterised by high disorder in the hydrocarbon chain region. It is important to note that real biological membranes contain both lamellar and non-lamellar lipids. Frustrated desire to form non-lamellar structures are stored in the membrane, and this can be related with the elastic properties of the bilayer [317, 345]. In this regime, entropic fluctuations may drive phase transitions or structural changes, at an elastic energy cost determined by curvature elastic properties, which can be directly related to the transmembrane lateral pressure (or stress) profile [211].

Given the existence of non-lamellar lipids in biological membranes, a question naturally arises: what is the reason for the presence of the non-lamellar membrane lipids? Since the composition of lipids is observed to vary across organisms and to be tightly regulated [353], the non-lamellar lipids are believed to play functional roles in biological membranes. One straightforward explanation is that they can be used to form local non-bilayer structures such as cellular budding, fission and fusion, which have been found experimentally [208, 324]. Another possible role of non-lamellar lipids might be that they can indirectly participate in influencing some biomembrane processes, through modulating some non-specific properties, for instance the lateral pressure profile and the electrostatic potential inside the membrane [54, 368]. Details about these two important transmembrane properties will be presented in following sections.

2.1.3 Lipid composition in biomembranes

As stated above, a broad range of diversity of lipids can be found in biomembranes, and the specific lipid composition in the bilayer can potentially have significant influences on cell activities. Generally, the lipid composition can be different in sharp contrast in different species, cells, and even evolving from time to time depending on external environments [45]. For example, cholesterol is present in mammalian

plasma membranes with a range from 20% to 50%, but is universally absent in prokaryotes [228, 335]. Considering only glycerophospholipids, combinations of different aliphatic tails and headgroups permits variation up to a thousand lipid types [83].

Effects of the lipid head: literature review on PC/PE mixtures

Among phospholipids, phosphatidylcholine (PC) is the most prevalent, accounting for 40%-50% of the total phospholipids [83, 195]. Phosphatidylethanolamine (PE), which ranges from 20% to 45% of the total phospholipids depending on located tissues or organs, is the next most abundant non-lamellar type [37, 177]. The membrane composition of lamellar/non-lamellar lipids is suggested to play significant roles in modulating the membrane functions by influencing some crucial nonspecific membrane properties. As the most commonly representative lamellar and non-lamellar lipids in biological membrane, PC (phosphatidylcholine) and PE (phosphatidylethanolamine) have intrigued many membrane researchers. Experimentally, Curran *et al.* performed a series of tests about the effect on the folding of an integral membrane protein bR (bacteriorhodopsin) from the PC/PE composition, finding a significant reduction in folding efficiency when the ratio of PE (with the same acyl chain as the host PC) was increased [71]. This dependence of bR folding to lipid composition was later attributed to the increase in curvature stress induced by the presence of PE [11]. But conversely, an opposite effect by addition of PE was found on the DGK (diacylglycerol kinase), another multi-α-helical integral membrane protein similar to bR, by Seddon *et al.* [316]. Similar variation of the effect from the non-lamellar lipid PE in membrane has been also found on β-barrel proteins (OmpA, outer membrane protein A precursor [174] and OpA, opacity-associated Protein A [86]). From these results, which are only a small sample from the entire collection of the investigation about PC/PE composition effects, it is already clear that, to identify the correlation between the membrane composition and the membrane properties that contribute to internal-membrane processes is of great importance to gain full understanding about those life processes.

Molecular dynamics simulation is very helpful to complement the general understanding on membrane properties. However, the application of molecular simulation

to the PC/PE mixed bilayer has been reported in only a few studies, since the simulational time required to investigate some important phenomena in mixed lipid bilayers is very long, and issues exist with the accuracy of PE force fields [80]. Properties like lateral pressure and dipole potential for PC/PE mixtures have been reported by a coarse-grained simulation study [251], but atomistic level results are still lacking.

2.1.4 Features of the lipid bilayer

Lateral pressure profile

The lateral pressure profile, $\Pi(z)$, where z is the spatial coordinate along the membrane normal direction, describes the pressure distribution in the membrane due to depth-dependent inhomogeneous interactions [54, 240]. As illustrated in Figure 2.4, the lateral pressure profile in lipid bilayer can be explained as follows: at the membrane-water interface, there is a strong inward (negative) pressure since the system attempts to limit the contact between water and hydrocarbon (γ_{phob}); this negative pressure is balanced by the repulsion between the hydrocarbon tails in the central region (π_{ch}); at the headgroup region, there is also a repulsive pressure due to steric and electrostatic interactions as well as hydration effects (π_{HG}) [51]. In practice, it has been found that the magnitude of $\Pi(z)$ at headgroup region

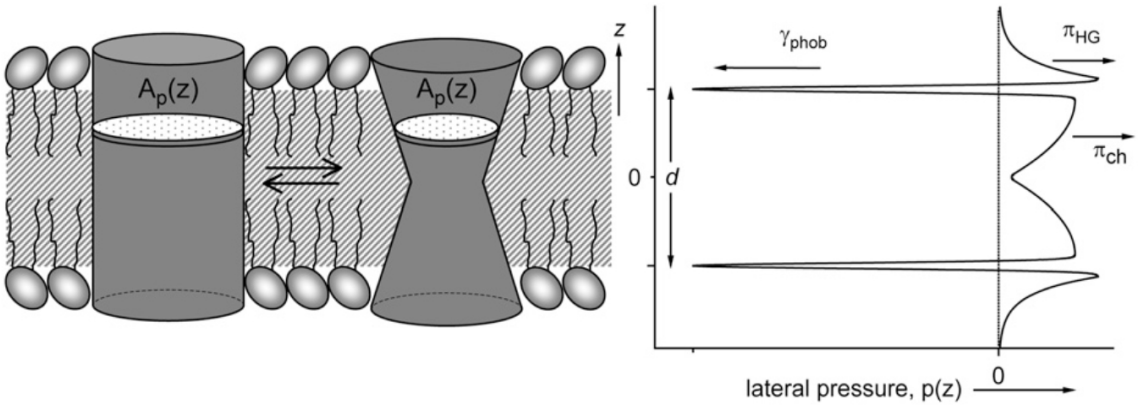

Figure 2.4: Schematic of the lateral pressure profile in lipid membrane [209]. π_{HG} and π_{ch} denote the integrated contribution of the lipid headgroups and chains, and γ_{phob} represents the hydrophobic interfacial tension.

is at the range of hundreds bar, and can reach about -1000 bar at the interfacial region. With such huge changes taking place within nanometres, the lateral pressure from membrane lipids is suggested to have a significant influence on the folding and conformational change, and consequently the function of membrane proteins.

Extensive research trying to reveal the connection between the lateral pressure profile and the membrane protein functionality has been done since the late 1990s when Cantor proposed that the change in lateral pressure profile can account for the dependence of protein conformation on membrane lipid composition [50, 51, 54]. The function of many membrane proteins, like MscL (mechanosensitive channel) [223, 267], KcsA (potassium crystallographically-sited activation channel) [352], rhodopsin [38], CTP (phosphocholine cytidylyltransferase) [318] and others, have been demonstrated to be related with the lateral pressure change. However, in these experimental studies, the lateral pressure profile itself was never measured but was only studied indirectly. The reason is that, compared with some of its associated properties such as the elastic moduli or spontaneous curvature that can be directly gauged, the lateral pressure profile is extremely difficult to access experimentally, when one realizes the tiny spatial scale of membrane and the necessity to maintain the membrane structure. So far, the only experiments [165, 344] trying to quantitatively gauge the lateral pressure profile in lipid membrane used pyrene moieties as probe to sense the local pressure change. By inserting di-pyrenyl PCs with different tail lengths into the target membrane, fluorescence signals can be detected. But even so, only the relative pressure changes in the chain region can be obtained, and the accuracy of the experimental data is disputed [82].

To calculate $\Pi(z)$ for a simulated bilayer system, pressure tensors (or stress tensors) are computed first, and by definition, the lateral pressure profile is [240, 251]:

$$\Pi(z) = \frac{P_{\mathrm{xx}}(z) + P_{\mathrm{yy}}(z)}{2} - P_{\mathrm{zz}}(z) \tag{2.1}$$

where $P_{\mathrm{xx}}(z)$, $P_{\mathrm{yy}}(z)$ and $P_{\mathrm{zz}}(z)$ are the three diagonal elements of the pressure tensor. In practice, the simulation box is first discretized into thin slabs parallel to the xy plane. For a typical bilayer system with homogenity along the xy plane, the tangential pressures are expected to converge to identical values, that is, $P_{\mathrm{xx}}(z) = P_{\mathrm{yy}}(z)$, hence only either of the two is strictly needed for the calculation. However,

both of them are usually calculated and the average of the two was used, thus improving the calculation precision. The normal component $P_{zz}(z)$ was assumed constant and equal to the external pressure at all slabs. This is a fundamental requirement by the mechanical equilibrium [359].

Here it should be noted that the microscopic pressure tensor is not uniquely defined. Tracing back to the very origin, the pressure tensor $\boldsymbol{P}$ is defined by the infinitesimal force $\mathrm{d}\boldsymbol{F}$ acting across an infinitesimal surface $\mathrm{d}A$ which is located at $\boldsymbol{r}$:

$$\mathrm{d}\boldsymbol{F}(\boldsymbol{r}) = -\mathrm{d}A \cdot \boldsymbol{P}(\boldsymbol{r}) \tag{2.2}$$

When it comes to a non-local force between two particles, how the force is reduced to a local $\mathrm{d}\boldsymbol{F}(\boldsymbol{r})$ is ambiguous, and depending on the arbitrary choice of an integration contour. Two definitions, one due to Irving and Kirkwood (I-K) [152] and other due to Harasima [135], are the most popular. The I-K contour is defined as the straight line connecting the particle pair, while the Harasima contour depends on the choice of coordinate system and in turn depends on the symmetry of the system. Considering the planar surface with Cartesian coordinates, the Harasima contour is the route along and normal to the surface $\mathrm{d}A$ (see Figure 2.5). Thus, for a

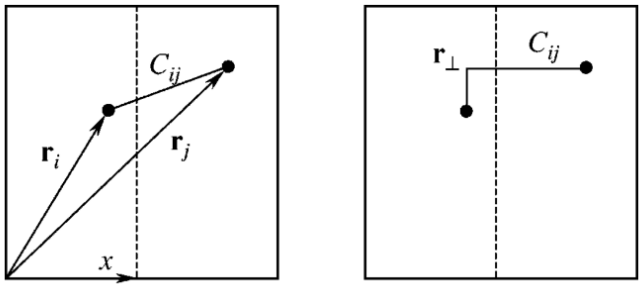

Figure 2.5: Integration contour C_{ij} for pressure tensor defined by Irving-Kirkwood method (left) and Harasima method (right) [131].

given $\mathrm{d}A$ only those pairs of particles for which their connecting line passes through $\mathrm{d}A$ contribute to the local force in the I-K method, while the Harasima method includes all interactions between particles in a neighbourhood volume of $\mathrm{d}A$ and those particles on the other side of $\mathrm{d}A$. Mathematically, it could be proved that the normal component of pressure tensor from the two methods are equivalent,

$P_{zz}^{IK}(z) = P_{zz}^{H}(z)$, but the tangential ones are not [131]. Here comes the ambiguity of $\Pi(z)$ calculated by different methods. However, the integral of the tangential components ends up with identical values, implying that both methods yield the same results of quantities not depending on local profiles of $\Pi(z)$, for example, the surface tension of the bilayer.

Dipole potential

The dipole potential, Ψ_d, is the intramembrane electrostatic potential originating from the dipolar components of the lipids, as well as the water dipoles at the membrane-water interface region [70, 368]. It is distinctive from another two membrane electrical potentials also frequently discussed. One is the surface potential (Ψ_s in Figure 2.6), due to the accumulation of charges in adsorbed ions at the interface, or charged head groups of phospholipids (such as phosphatidylserine lipids, PL). The magnitude of Ψ_s in biological membranes is typically tens of millivolts, and it decays away from the membrane surface exponentially in about 1 nm. The other is the transmembrane potential ($\Delta\Psi$ in Figure 2.6) led by the ion concentration difference at the two sides of the membrane, which is resulted from the selective transport of ions by membrane proteins. In biological systems, $\Delta\Psi$ is usually on the order of tens of millivolts as well, and is famous for the regulation of voltage-gated membrane channels. Different from Ψ_s, the dipole potential Ψ_d arises from the dipolar alignment (or the partial charge redistribution) on the lipid molecules, which means that even for a membrane consisted of overall neutral lipids like PC and PE, Ψ_d still exists, and the dipolar alignment depends on the lipid residue structures such as the unsaturation level of hydrocarbon chains, nature of the headgroup, and the linkage in between [272, 333]. Water, as a dipolar molecule, have also been thought to strongly influence Ψ_d [117, 368]. Sometimes, the term "electrostatic potential" is used to describe Ψ_d, especially when Ψ_s does not exist for a non-charged lipid membrane, or to describe the overall intrinsic transmembrane potential when the two are not differentiated.

The dipole potential of lipid membranes was first discovered in the study of the carrier mechanism of ion transport [192]. It was found that the fat-soluble ions could diffuse directly across lipid membranes and if comparing two structurally similar

ions (corresponding to the similar diffusion coefficients), the electrical conductivity of membrane with anions (TPB^-, tetraphenylborate) added in the aqueous phase is 10^5 times higher than with cations (TPP^+, tetraphenylphosphonium) at the same concentration. This highly significant difference was attributed to the different partition coefficient between the membrane and water phases for opposite charged ions, thus it was hypothesized that the inner membrane must be positively charged, that is, a positive potential difference exists between the membrane interior and the surface region.

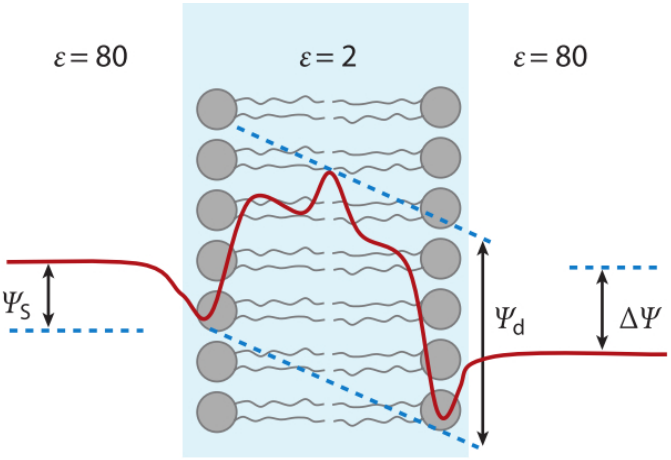

Figure 2.6: Membrane-related electrostatic potentials [368]. Ψ_d, Ψ_S, $\Delta\Psi$ and ε denote the dipole potential, surface potential, transmembrane potential and the dielectric constant in the medium.

This hypothesis was further clarified and proved in the following decades of studies [40, 108, 141], and the functional role of the dipole potential has been drawing membrane researcher's attentions. The magnitude of Ψ_d has been estimated in the order of hundreds of mV [168, 368]. Noticing that Ψ_d drops over a ~4-nm thick membrane, an enormous electric field in the range of $10^7 - 10^9$ V/m will be generated. Such a large force may drastically influence many biological processes in membrane, like the modulation of the protein function [202, 303, 334], the insertion and folding of some amphiphilic peptides [69], the partition and translocation of macromolecules [7], and membrane fusion [68]. However, similar to the lateral pressure profile, the dipole potential is also hardly accessible experimentally. Some methods have been developed to estimate the bilayer membrane dipole potential, but

are not satisfying. The planar lipid bilayer method [108, 310] indirectly measures the membrane conductance in the presence of hydrophobic ions, but errors are brought out because the hydrophobic ions are always too large to be strictly taken as an ideal detecting charge. Another one is the lipid monolayer method [40, 186], which lets lipids spread on an air-water interface to form a lipid monolayer and then measures the potentials by electrodes. Unfortunately, this method also has inevitable drawbacks. Even provided we can accept the monolayer to be equivalent to half a bilayer, the air-water surface potential is introduced in the measurement, the magnitude of which is not known.

2.2 The molecular dynamics simulation technology

Molecular dynamics (MD) is a computational simulation technique to study the equilibrium and transport properties of many-body systems, by solving the time-evolving motions of the interacting particles in the system following the laws of classical mechanics. As a statistical mechanics method, MD simulation connects the microscopic states (momentum, potential energy) and the macroscopic physical quantities (temperature, pressure, etc.).

For a molecular system with N particles, its Hamiltonian (i.e. the total energy) can be written as sum of the kinetic energy and the potential energy

$$\mathcal{H}(\boldsymbol{p}, \boldsymbol{r}) = \sum_{i}^{N} \frac{\boldsymbol{p}_i^2}{2m_i} + U(\boldsymbol{r}_1, \ldots, \boldsymbol{r}_N), \tag{2.3}$$

where $\{\boldsymbol{p}_i | i = 1, \ldots, N\}$ and $\{\boldsymbol{r}_i | i = 1, \ldots, N\}$ are the momentum and coordinates, m_i the mass of the ith atom ($i = 1, \ldots, N$). From this, a trajectory of the system varying with time is generated by integrating Newton's law of motion in time steps Δt. Several numerical integrating algorithms are available to solve the equations of motion in an energy-conservative and time-reversible manner [107, 292, 363]. For instance, the leap-frog algorithm among many others updates the trajectory using coordinates $\boldsymbol{r}$ at each temp step and velocities $\boldsymbol{v}$ halfway in between time steps,

given the acceleration $\boldsymbol{a}$ from forces:

$$\boldsymbol{r}(t+\Delta t) = \boldsymbol{r}(t) + \Delta t \cdot \boldsymbol{v}(t+\frac{1}{2}\Delta t), \tag{2.4}$$

$$\boldsymbol{v}(t+\frac{1}{2}\Delta t) = \boldsymbol{v}(t-\frac{1}{2}\Delta t) + \Delta t \cdot \boldsymbol{a}(t), \tag{2.5}$$

Current widely-used integrating algorithms including leap-frog, velocity-Verlet, etc., are mostly equivalent for typical molecular dynamics simulations in terms of computational requirements, as the integration part is usually trivial compared to the force calculations.

Once an MD simulation is set up, many thermodynamic properties can be calculated. In a canonical ensemble, where the atom number N, system volume V, and temperature T are fixed, each state $(\boldsymbol{p}, \boldsymbol{r})$ is weighted by the Boltzmann factor:

$$\rho(\boldsymbol{p}, \boldsymbol{r}, T) = \frac{e^{-\beta \mathcal{H}(\boldsymbol{p},\boldsymbol{r})}}{\int e^{-\beta \mathcal{H}(\boldsymbol{p},\boldsymbol{r})} \mathrm{d}\boldsymbol{p}\mathrm{d}\boldsymbol{r}}. \tag{2.6}$$

where $\beta = 1/k_B T$ and k_B is the Boltzmann constant; then the equilibrium average of some quantity G is expressed in terms of phase-space integrals involving the potential function $U(\boldsymbol{r}_1, \ldots, \boldsymbol{r}_N)$:

$$\langle G \rangle = \frac{\int G(\boldsymbol{r}_1, \ldots \boldsymbol{r}_N)\, e^{-\beta U(\boldsymbol{r}_1, \ldots \boldsymbol{r}_N)}\, \mathrm{d}\boldsymbol{r}_1 \cdots \boldsymbol{r}_N}{\int e^{-\beta U(\boldsymbol{r}_1, \ldots \boldsymbol{r}_N)}\, \mathrm{d}\boldsymbol{r}_1 \cdots \boldsymbol{r}_N}. \tag{2.7}$$

In MD simulation, based on the ergodic hypothesis, the average $\langle G \rangle$ can be calculated over a series of M measurements during the evolving of a single system:

$$\langle G \rangle = \frac{1}{M} \sum_{\mu=1}^{M} G_(\boldsymbol{r}_1, \ldots \boldsymbol{r}_N) \tag{2.8}$$

Assuming the sampling for a quantity is sufficient, this form of averaging from the dynamics of a single system will be identical with the one shown in equation 2.7 over an ensemble of independent systems. This is the fundamental hypothesis for the molecular dynamics simulation, and its adequacy has been proved by countless antecedent simulation results.

In the following sub-sections, fundamental aspects on how the dynamics of the

simulated system is integrated, including the general interaction potentials, computational conventions and measurement of thermodynamics properties, are introduced [27, 292, 347, 355].

2.2.1 Interaction potentials

To simulate any system, it is necessary to describe the interactions between the constituent particles. With no quantum effects taken into consideration, atoms in MD simulations are usually represented as point masses interacting through forces that are defined by a set of potentials accounting for different types of interactions. The set of potential functions and corresponding parameters is called the force field. In molecular systems, the force field comprises potential energy terms describing nonbonded interactions between any pair of atoms, like van der Waals and electrostatics forces, and intramolecular covalent interactions such as bond, angle and dihedral terms.

The Lennard-Jones potential describes the pairwise interatomic forces generically as

$$U_{\mathrm{LJ}}(r) = 4\varepsilon \left[\left(\frac{\sigma}{r}\right)^{12} - \left(\frac{\sigma}{r}\right)^{6} \right] \tag{2.9}$$

where r is the distance between the pair, with the parameter ε governing the strength of the interaction and σ defining a length scale (Figure 2.7). The Lennard-Jones potential provides the two principal features of the general nonbonded interaction: the resistance to compression at close range, and on the other hand the attraction over a range of separations.

In atomic level modelling, the electrostatic interaction is typically described by empirical partial charges distributed on atoms, thus the potential energy $U_{\mathrm{C}}(r)$ is defined by Coulomb's law for a pair of point charges Q_i and Q_j whose distance is r:

$$U_{\mathrm{C}}(r) = \frac{Q_i Q_j}{4\pi\epsilon_0 r} \tag{2.10}$$

with ϵ_0 the dielectric constant in free space.

Regarding the intramolecular bonded interactions, the bonding stretches and angles, and the improper angles are usually described as harmonic oscillators, while

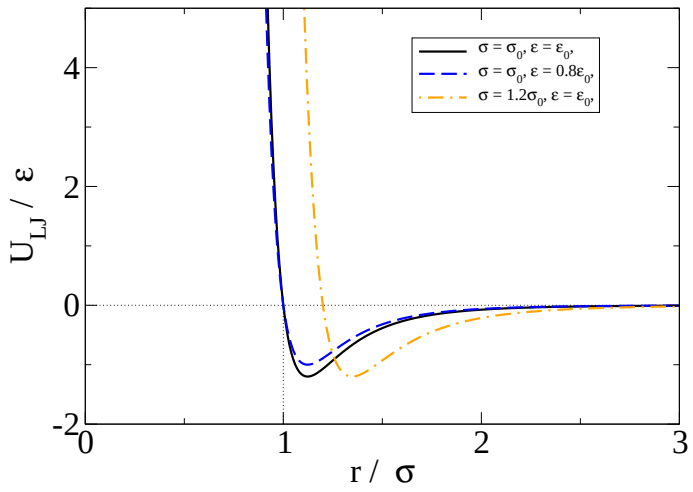

Figure 2.7: The Lennard-Jones potential: ε and σ define the model. ε_0 and σ_0 are the reference values, based on which the change in ε and σ leads to the change in the potential.

dihedrals as a suitable cosine expansion:

$$U_{\text{Bonded}} = \sum_{\text{bonds}} \frac{1}{2} k_b \left(l - l_0\right)^2 + \sum_{\text{angles}} \frac{1}{2} k_\theta \left(\theta - \theta_0\right)^2 + \sum_{\text{impropers}} \frac{1}{2} k_\xi \left(\xi - \xi_0\right)^2 + \sum_{\text{dihedrals}} k_\phi \left[1 + \cos\left(n\phi - \phi_0\right)\right] \tag{2.11}$$

where k_b, k_θ, k_ξ and k_ϕ are the force constant for bonds, angles, impropers and dihedrals; n is the dihedral multiplicity; l_0, θ_0, ξ_o, ϕ_0 are the corresponding reference values.

Based on these most fundamental potential forms, various types of force fields are practically derived. More complex potential functions may be extended in occasional cases, for instance, when the orientation of particles need to be considered. Moreover, given these universal interaction forms, the precise parameters varies in different models aiming for different systems and calibrated to different objectives. Meanwhile, for computational cost reasons, a subset of models in less confined mesoscopic scales are developed. United-atom (UA, hydrogens grouped with heavy atoms) and coarse-grained (CG, atoms grouped as macroparticles) can reach longer time and length scales with the drawbacks of losing some details. A brief review

on different force-fields is presented in 2.3.1 and 2.3.2.

2.2.2 Long-range nonbonded interactions

Lennard-Jones interactions

In practice, the theoretically infinite Lennard-Jones interaction is usually calculated only within a given distance, to keep the computation to a reasonable level. Since the potential energy between a pair of particles decays rapidly with increasing interparticle distance, proper truncation of the long-range potential is acceptable without bringing gross errors. To apply a cut-off radius r_c, beyond which the potential will be disregarded, is straightforward but problematic. The potential at r_c becomes discontinuous, hence the force is no longer conservative and artefacts are generated during the simulation. To tackle this problem, "switching functions" are often used in practical algorithms, which switches the force off smoothly at a vicinity of r_c.

Coulomb interactions

From Equation 2.10, we know the electrostatic interaction decays as r^{-1}, which is slow that the long-range interaction cannot be simply omitted. Also, commonly in biomolecular systems, particles carry charges or polarization happens, in which cases the Coulomb forces are not negligible even beyond relatively long distance. Numerical Ewald summation methods [187] are commonly used to solve the long-range electrostatic interaction. In practical computations, the particle charges are mapped to a 3-d mesh to calculate the potential and then interpolate the electric field back to the particles. By applying Fast Fourier Transform (FFT), the computational cost can be reduced to the scale of $N \log(N)$.

More specifically, Coulomb interactions between a charged particle and all other particles in the simulation box, as well as all their periodic images infinitely, are considered in the Ewald sum method. The series of the summation of all these interactions is converging slowly (in r^{-1} according to Equation 2.10). A mathematical solution is to impose two Gaussian charge distributions on each point charge with equal magnitudes and of opposite signs, and then compute them separately in the

real space and reciprocal space. In this way, the calculation is converging much more rapidly, but still computationally expensive, especially the one in reciprocal space which is normally in the scale of N^2 [268]. Further employment of FFT on the basis of the classic Ewald summations can speed-up the computation to the order of $N \log(N)$. In order to perform FFT, each of the charges in the system needs to be redistributed onto mesh points, and this treatment is called the particle-mesh method [142]. A compromise is needed here that only closely surrounding points are used while energies and forces further away will be interpolated, so as to reproduce the effect the original charge as much as possible and to obtain a great acceleration.

Variants of the particle-mesh method are further developed, including the original particle-particle particle-mesh (PPPM) method developed by Hockney and Eastwood [142]. In the PPPM method, particles close to each other are summed together and charges are assigned on mesh points with approximations that mainly depend on the order of the assignment (i.e. how many mesh points the charge of one particle is distributed onto). Also, a mesh-based electrostatic potential is reconstructed with a so-called "influence function" to minimize the difference with the original continuum potential. Another popular algorithm is the particle-mesh-Ewald (PME) method [73], which sticks to the continuum Coulomb Green function (the Fourier transformed Coulomb potential in reciprocal space), without mesh-based adjustment for the discrete FFT. Combined is the Lagrange interpolation for the charge assignment. The seemingly simple scheme of PME method cancels certain discretization errors [85]. Both PPPM and PME are inevitably less accurate in theory than the classic Ewald sum, but already satisfy the typical needs in a simulation; they are implemented in different MD packages and are adopted as an integral element of different force fields [1, 30, 307].

2.2.3 Periodic boundary conditions

Molecular dynamics simulation systems contain a relatively small amount of particles, compared with Avogadro's number which represents the real-life scale. In such microscopic systems, from which what we are interested in is the typical state of interior atoms, the boundary effect will introduce severe artefacts if a system is simply taken as particles placed in a closed container. Therefore, the periodic

boundary condition is always applied to not only bound the system but also get rid of the effects of physical walls. The initial system is replicated infinitely to surround itself, which means whenever a atom moving out through a boundary face, it re-enters the system immediately through the opposite face. But in this way, another problem will come out: all the infinite images of any given particle would be considered in the interaction calculations, including the interactions between their images and themselves. To avoid this, the minimum image convention is normally adopted: each atom of the main simulation cell interacts only with the nearest image of any other particle.

2.2.4 Thermostats and barostats

In most applications, the simulation is meaningful at constant temperature, thus a canonical NVT ensemble should be generated; when constant pressure is desired, the NpT condition is needed. A series of methods are available to control the temperature and pressure of the system (i.e. a thermostat and barostat):

The temperature of a molecular system is related to the kinetic energy (which will be detailed in Section 2.2.5). **Langevin thermostat** [313] belongs to the family of stochastic methods. The basic idea is to apply a frictional force and a stochastic force to the momenta to control the temperature. It can be proved mathematically that the distribution function of the momenta under the Langevin thermostat is still a normal distribution, therefore a canonical ensemble is kept. However, the dynamics of the system is disturbed since the random force causes an extra diffusion term on the momenta. The **velocity-rescale thermostat** [46] also produces a stochastic dynamic, by reassigning the velocity from an appropriate Maxwellian distribution. The reassignment process is on randomly-selected molecules at pre-set time intervals. A rigorous canonical ensemble is also generated. The **Nosé-Hoover thermostat** [145] introduce an additional degree of freedom as a thermal reservoir. A fictitious "mass of the reservoir part is also introduced to construct the overall equations of motion of the extended system. The "mass controls the energy flow between the real system and the reservoir, and thus determines the temperature fluctuations. The **Berendsen thermostat** [31] is a weak-coupling method. The way to maintain the temperature is to couple the system to an external heat bath

that is fixed at a constant temperature. The bath supplies or extracts thermal energy from the system as appropriate at certain time steps, and velocities of the particles in the simulated system are rescaled. The change rate of the temperature is proportional to the difference between the system and the heat bath, and a time constant controls how strong the coupling is. In this way, the system temperature decays smoothly towards the target temperature, but the disadvantage is that the canonical ensemble is not kept and temperature fluctuations are not realistic.

Since the pressure is related to the virial (which usually changes more quickly than the internal energy), a greater fluctuation is often expected for pressure. A simulation maintains its pressure by changing the volume. Similar spirits of the thermostat methods described above can be applied for pressure control. With the **Berendsen barostat** [31], the system is coupled to a pressure bath, analogous to a heat bath. The rate of change of pressure is controlled by a coupling constant, and the system volume and coordinates are scaled so that the system pressure decays towards the desired value. The **Parrinello-Rahman barostat** [263] treats each pressure tensor independently as an additional degree of freedom in the extend system scheme. Here, the additional degrees of freedom can be considered as pistons acting on the system, where the mass of the piston determines oscillations of the volume change. The equation of motions is in a similar form as the Nosé-Hoover thermostat, but with the variable being the system volume and slightly more complex due to non-orthogonality in the three dimensions.

Generally, stochastic methods (including the Langevin thermostat and velocity-rescale thermostat) and extended system methods (the Nosé-Hoover thermostat/barostat and the Parrinello-Rahman barostat) generate a canonical ensemble while the weak-coupling methods not, but stochastic methods disturb the dynamics and extended system methods oscillates. Practical focuses in the simulation need to be considered for the choice of thermostat and barostat, such as what are the properties interested in and whether the simulation is in non-equilibrium conditions or not.

2.2.5 Thermodynamic measurements

After a system begins to evolve following the force field potentials and other specific constraints, thermodynamic properties can be calculated from the trajectories of the

particles in the system. Measurements in MD simulations are averaged over time, typically after an initial equilibration stage. The calculation for the very fundamental quantities are introduced below.

Energies The total energy of a system is the sum of the potential energy and kinetic energy. The total potential energy is simply obtained as the potential energies of all the pair interactions; the instantaneous kinetic energy of a N-particle system is:

$$\mathcal{K} = \frac{1}{2}\sum_{i=1}^{N}(m_i {\boldsymbol{v}_i}^2) \tag{2.12}$$

where m_i, $\boldsymbol{v}_i$ are the mass and velocity of the i-th particle. Here, particles are only considered as point masses, which is the case for ordinary atomistic simulations.

Temperature Given the kinetic energy, the instantaneous temperature $\mathcal{T}$ can be calculated according to the equipartition theorem as

$$\mathcal{T} = \frac{2\mathcal{K}}{k_B \cdot DOFs} \tag{2.13}$$

where k_B is the Boltzmann constant and DOFs means the total number of the degrees of freedom in the system ($3N - N_{constrains}$ for the point mass system).

Pressure The pressure $\mathcal{P}$ can be defined from the virial expansion

$$\mathcal{P}V = nk_B\mathcal{T} + \mathcal{W} \tag{2.14}$$

with n the number of atoms, V the system volume and $\mathcal{W}$ the "internal viral". For pair-potentials, $\mathcal{W}$ is

$$\mathcal{W} = \frac{1}{3}\sum_{i}\sum_{j>i}\boldsymbol{r}_{ij}\boldsymbol{f}_{ij}, \tag{2.15}$$

therefore the instantaneous pressure is

$$\mathcal{P} = \rho k_B\mathcal{T} + \frac{1}{3V}\sum_{i}\sum_{j>i}\boldsymbol{r}_{ij}\boldsymbol{f}_{ij} \tag{2.16}$$

with ρ the system density.

2.2.6 Parallel tempering technique for protein folding free energy

With a standard MD simulation, efficient sampling of the conformational space of many important biological processes (such as protein folding, self-assembly of lipids) remains a great challenge [150], because the system tends to stay trapped in one specific local minimum-energy state at low temperatures. To overcome such energy-minima problem, sampling-enhanced simulations have been designed so that random walks in the energy space may be realized. The parallel tempering method (also called replica exchange method, or replica Monte Carlo method) is one successful example among many proposed techniques [33, 98, 338].

Generally, the idea of parallel tempering is to simulate a series of replicas of the studied system in parallel, in the canonical ensemble at a range of temperatures, and then during the simulation neighbouring replicas are swapped based on a balancing acceptance criterion. In such a process, those high temperature replicas more easily cross energy barriers thus visit the phase space more exhaustively, while those low temperature replicas stay in a local region of the phase space. By allowing the systems to exchange configurations at different temperatures, the system at a lower temperature (which is usually the one of interest) is enabled to reach a broader configuration space. The origin of parallel tempering could be traced back to 1986, when Swendsen and Wang [369] introduced a replica Monte Carlo method to partially exchange configuration informations between replicas of a system. Then Sugita and Okamoto developed the parallel tempering formulation for a MD simulation [338], and following that, the parallel tempering technique has been widely applied to study free energy landscape problems, especially in the topic of protein folding [98, 312]. The folding free energy contour map for a series of proteins were determined using parallel tempering, and folding mechanisms and intermediate state structures were also revealed [113, 384, 386]. In addition, parallel tempering has been applied to facilitate NMR structure refinement [63].

Technically, for a generalized ensemble for parallel tempering which consists of M replicas at different temperatures T_m ($m = 1, \ldots, M$), the meta state X of this

ensemble is a collection of all M states $x_j = (\boldsymbol{p}, \boldsymbol{r})$ $(j = 1, \ldots, M)$. Since the replicas are non-interacting to each other, the weight factor for the state X is given by the product of Boltzmann factors for each replica based on Equation 2.6:

$$\rho_{PT}(X) = \exp(\sum_{j}^{M} \beta_j \mathcal{H}(\boldsymbol{p}, \boldsymbol{r})). \tag{2.17}$$

At certain steps of the simulation, swap between a pair of replicas is attempted, and in order to maintain the equilibrium canonical distribution functions, a balance condition on the transition probability $\Pi(X \to X^{'})$ is imposed:

$$\rho_{PT}(X)\Pi(X \to X^{'}) = \rho_{PT}(X^{'})\Pi(X^{'} \to X), \tag{2.18}$$

i.e.,

$$\frac{\Pi(X \to X^{'})}{\Pi(X' \to X)} = \frac{\rho_{PT}(X^{'})}{\rho_{PT}(X)} = e^{(\beta_k - \beta_l)(\mathcal{H}(\boldsymbol{p}^l, \boldsymbol{r}^l) - \mathcal{H}(\boldsymbol{p}^k, \boldsymbol{r}^k))}, \tag{2.19}$$

where k and l are the two replicas that we are attempting to swap. Here comes the Metropolis criterion to satisfy the balance condition of the swapping:

$$\Pi(X \to X^{'}) = \begin{cases} 1 & for\ \Delta \leq 0, \\ e^{-\Delta} & for\ \Delta \leq 0, \end{cases} \tag{2.20}$$

where $\Delta = (\beta_k - \beta_l)(U(\boldsymbol{r}^l) - U(\boldsymbol{r}^k))$. Whether the swap between replicas k and l is accepted is determined based on the probability. The Hamiltonian $\mathcal{H}(\boldsymbol{p}, \boldsymbol{r})$ reduces to $U(\boldsymbol{r})$ in both Monte Carlo simulations (which is natural), and MD simulations (where velocities are rescaled in a swap). Suppose now the pair of replicas is swapped:

$$X = (\ldots, x_k^k, \ldots, x_l^l, \ldots) \to X^{'} = (\ldots, x_k^l, \ldots, x_l^k, \ldots), \tag{2.21}$$

where the superscript and subscript label the replica and the temperature, respectively. Written in more details,

$$\begin{aligned} x_k^k = (\boldsymbol{p}^k, \boldsymbol{r}^k) \to x_k^{l^{'}} = (\boldsymbol{p}^{l^{'}}, \boldsymbol{r}^l), \\ x_l^l = (\boldsymbol{p}^l, \boldsymbol{r}^l) \to x_l^{k^{'}} = (\boldsymbol{p}^{k'}, \boldsymbol{r}^k). \end{aligned} \tag{2.22}$$

This is equivalent mathematically to exchange the two corresponding temperatures of replica k and l:

$$\begin{aligned} x_k^k = (\boldsymbol{p}^k, \boldsymbol{r}^k) \rightarrow x_l^{k'} = (\boldsymbol{p}^{k'}, \boldsymbol{r}^l), \\ x_l^l = (\boldsymbol{p}^l, \boldsymbol{r}^l) \rightarrow x_k^{l'} = (\boldsymbol{p}^{k'}, \boldsymbol{r}^k). \end{aligned} \tag{2.23}$$

The equivalence is important in practice because swapping only the temperature is much more cost-saving in communication than swapping the two full set of coordinates and momenta.

2.3 Force fields for simulating the biomembrane system

The development of a realistic membrane model (i.e. the force field) is challenging, considering the complex structure and dynamics of the biomembrane system. All-atom models that explicitly treat each atom in a molecular system have been employed for simulating biological macromolecules for decades [99, 163], now facilitating the study of many biophysical phenomena in the nanosecond to microsecond temporal scale with considerable accuracy. This is achieved based on the fast computer power growth and algorithmic improvement, but coarse-grained models have also gained popularity by neglecting some atomistic details in order to allow for a significant increase in both temporal and spatial scales [198, 218, 251]. Early coarse-grained models were developed to simplify protein folding simulations [235, 371], where protein side chains were replaced by spheres or a 2-dimensional square lattice to reduce degrees of freedom while the main features in the system are selectively retained. In the past decades, needs of coarse-graining in various scenarios have been exploited such as to reduce the dimensionality of the free-energy landscape [302], to renormalize long-timescale processes [183, 378], etc. In between the full atomistic and the coarse-grained level, united-atom approaches are also widely used especially for lipid simulations: non-polar hydrocarbon groups are reduced to single particle which could speed-up the simulation by abandoning the relatively large number of aliphatic hydrogens in all-atom systems. Here, we present a brief literature review

for atom-level (all-atom or united-atom) lipid force fields and coarse-grained water force fields, which are within the focused scope of this thesis.

2.3.1 A brief review on atom-level lipid force fields

The first MD simulation of a lipid bilayer with an explicit solvent can be traced back to 1988, in a study on a sodiumdecanoate/decanol/water system [99]. Lipid chain order parameters and diffusion constants were calculated with full atomic detail. Since that, a tremendous number of lipid force fields has been developed. Among them, the GROMOS families [60, 315], CHARMM [171, 200], and AMBER/GAFF [55, 156] have become the most popular ones. In these lipid models, the treatment of the potential energy function (which is the core of any force field to describe the simulated system) are majorly common based on the fundamental nonbonded Lennard-Jones potential (Equation 2.9) and a collection of intramolecular potentials (Equation 2.11) to describe bonds, angles, distortions, etc., while they differ in other aspects including the parameterization, treatment of solvation, etc. Below we summarize the basics of several representative atom-level lipid force fields in some details.

GROMOS lipid force field The original GROMOS (Groningen Molecular Simulation) force field is not fully atomistic, where united-atom representations are used for non-polar hydrocarbon groups in lipid tails. Further modifications, such as optimizations of non-bonded and torsion interactions, have been applied to improve the performance [237]. The parameterization of early GROMOS force fields is applied on solvation free energies for alkanes, to obtain parameters for aliphatic carbon atoms. In the latest version of GROMOS, the GROMOS53A5 and GROMOS53A6 force fields, an extended set of polar groups were targeted for parameterization [48]. Validation studies [198, 276] have shown that the GROMOS53A6 parameter set improves the fluidity of DPPC lipid, and structural properties including lipid volume, ordering and conformation of acyl chains are in good agreement with experiments. However, to our knowledge, the GROMOS model has not been tested for the PE lipid family, and most studies employing GROMOS in the literature are limited to PC lipids.

AMBER/GAFF lipid force field The AMBER lipid forcefield series is adhered to the AMBER MD software package and is built up on a modular basis [308]. The General Amber Force Field (GAFF) allows different lipid types are flexibly assembled from head and tail groups, and interaction parameters are simply generated from the GAFF parameter sets. Early versions of the AMBER force field are less frequently used for investigation into lipid membranes. The average area per lipid was found to be underestimated by AMBER94 and GAFF compared to the experimental value for DMPC and DOPC lipids [196, 225]. The GAFF force field seems not able to satisfyingly reproduce bilayer structures without further optimization.

In the most recent AMBER Lipid14 forcefield [88], the Lennard-Jones interaction and torsion interactions in aliphatic tails were further parameterized to correct the defect in the previous version Lipid11 forcefield that a external surface tension is required. Validations were performed on five PC lipids and also the POPE lipid. Compared with experimental values, basic structural properties including lipid area and volume, order parameters, as well as the lipid lateral diffusion were in good agreement for PC lipids in tension-free simulations, but results for POPE indicated somehow artificial chain order and other properties showed to be less accurate to different extents.

CHARMM lipid force field The CHARMM (Chemistry at Harvard Molecular Mechanics) force field may be the dominant all-atom lipid force field. It includes a wide variety of phospholipids and also other types of lipids [158]. The original CHARMM force field (CHARMM22) was published in 1996 [16], with a slightly more complicated parameterization for intramolecular potentials compared with GROMOS and AMBER force fields: the Urey-Bradley term is included in covalent angles, and more variations of dihedral angles are parameterized individually for different lipid types. In the following CHARMM27, descriptions of lipid bilayers were further improved on the basis of quantum-chemical calculations [110]. However, it was found the CHARMM27 model underestimated fundamental parameters including the lipid area in constant pressure simulations, with an over-emphasize of the trans-conformer in alkane chains.

In the most updated CHARMM36 lipid force field, the parametrization process targeted both quantum mechanical and experimental data [172], in order to correct

the two main flaws in the predecessor CHARMM27/27r version in reproducing surface tension and experimental deuterium order parameters [13, 332]. Several PC and PE lipids with varying chain length and saturation levels were test for validation. Surfaces areas, hydration levels, and order parameters with the NPT ensemble were shown to be improved by the reparameterization. It is also worth noting that the dipole electrostatic potential also showed improvements over previous parameter set, which may be mainly related to the partial atom charge modifications. This is crucial for the membrane simulation in this project, as the dipole potential is a particularly focused property among others. We employed the CHARMM36 lipid force field in all lipid bilayer simulations presented in this thesis.

2.3.2 A brief review on coarse-grained water force fields

Though computational power has exponentially grown in recent years, brute-force atomistic simulation can still not be the solution for all cases. Coarse-grained models were developed with the idea of simplification to accelerate but not necessarily sacrificing the desired information generated from the simulation. Water is perhaps the most popular coarse-graining target because it is the most prevalent solvent in biological environments as well as in many other applications. An ideally reduced description of a biomolecular system might be reached that the solvent characteristics are simplified to save computational cost whereas the mainly focused physics is captured. However, the presence of water is crucial to the solutes in the system as they are closely interacted. Thus, a balance between accuracy and efficiency becomes necessarily important to a CG water model. A CG water model maps one or more water molecules from the atomistic scale to the CG scale. Below we briefly summarize the basics of representative coarse-grained water force fields, and introduce the details of the ELBA water force field which will be one of the main topics of the project presented.

MARTINI water force field The MARTINI model [207] maps 4 water molecules into 1 CG bead, where CG beads interact through a 12-6 Lennard-Jones interaction. A trial-and-error procedure was used for parametrization to reproduce the experimental density of bulk water and other properties. MARTINI water reasonably

reproduces fundamental thermodynamic properties such as the diffusion, but possibly due to the lack of explicit electrostatic interactions, it has poor representation of properties such as interfacial tension, compressibility, and the phase behaviour [379]. Attempts have been made to develop a polarized-MARTINI model [382], where two additional charged sites are added, with fixed distance set between the charged sites and the original one. This model has shown improved melting temperature representation and transportation properties [297].

BMW water force field The BMW (big multipole water) model [379] performs a 4-to-3 mapping, which is using three sites to represent four water molecules. In the BMW model, the two outer sites only interact through Coulombic forces while the center bead through both Coulombic and van der Waals forces. The geometry and charges of BMW were optimized against dipole and quadrupole moments of a four-water cluster. Similar to MARTINI, a relative dielectric screening is required for BMW to fit to experimental density, air-water interfacial tension, etc. In a DPPC bilayer simulation combined with BMW, a correct dipole potential were obtained, but cautions were also given for its usage outside 300K where the parameters were optimized [25].

WT4 water force field The WT4 model [75] (11-to-4 mapping) was an attempt to further extend the degree of coarse-graining of water, while still incorporating the electrostatics and polarisability. Mass of the WT4 bead was fitted to the experimental density, and a partial charge was assigned to each bead to reproduce the dielectric permittivity. Every four WT4 beads are tetrahedrally bonded, and the bonds are relatively flexible to suit for the polarizability. The WT4 model has been shown a good solvation feature especially for the DNA structure compared with atomistic models [299].

ELBA water force field The ELBA water model was developed by Orsi et al. [242, 249], where one water molecule is mapped onto one Lennard-Jones sphere with an additional point dipole embedded. Interactions in ELBA water follow a shifted-force parametrization derived from the classic Stockmayer polar model (i.e. the general "Lennard-Jones plus point dipole" model) [372]. The Lennard-Jones

part follows a shifted-force scheme proposed by Stoddard and Ford [336] and the electrostatic part is modified from the classic electrostatic model [9, 283], so that both the potential energy and its derivative (the force) vanish to zero smoothly at the cut-off. In this way, system energy conservation is improved and the cut-off related artifact for dipolar particles is removed.

The ELBA model was parametrized against density and self-diffusion constant of bulk water. Other fundamental water properties were also accurately reproduced, including the heat of vaporisation, surface tension, and the liquid-vapour interface structure [243]. However, one significant issue was observed for the radial distribution function, which showed qualitative and quantitative differences compared to experimental and atomistic data. In terms of computational efficiency, the speed-up of ELBA compared to traditional all-atom models such as TIP3P and TIP4P reaches one or two orders of magnitude.

ELBA is one of the main focuses of the presented project. Quantitative descriptions and the rationales of the ELBA potential are as below:

$$U = U_{\mathrm{LJ}} + U_{\mathrm{dip}}, \tag{2.24}$$

where the Lennard-Jones interaction term

$$\begin{aligned} U_{\mathrm{LJ}} = {} & 4\epsilon \left[\left(\frac{\sigma}{r}\right)^{12} - \left(\frac{\sigma}{r}\right)^{6} \right] \\ & + 4\epsilon \left[6\left(\frac{\sigma}{r_c}\right)^{12} - 3\left(\frac{\sigma}{r_c}\right)^{6} \right] \left(\frac{r}{r_c}\right)^{2} - 4\epsilon \left[7\left(\frac{\sigma}{r_c}\right)^{12} - 4\left(\frac{\sigma}{r_c}\right)^{6} \right], \end{aligned} \tag{2.25}$$

and the dipole interactions

$$U_{\mathrm{dip}} = \frac{1}{4\pi\varepsilon_0} \cdot \left[1 - 4\left(\frac{r}{r_c}\right)^{3} + 3\left(\frac{r}{r_c}\right)^{4} \right] \cdot \left[\frac{1}{r^3}(\boldsymbol{\mu}_i \cdot \boldsymbol{\mu}_j) - \frac{3}{r^5}(\boldsymbol{\mu}_i \cdot \boldsymbol{r})(\boldsymbol{\mu}_j \cdot \boldsymbol{r}) \right]. \tag{2.26}$$

In Equation 2.25, σ and ϵ have the standard meaning in Lennard-Jones potential [9, 292], r is the inter-particle distance, and r_c is the cut-off radius. In Equation 2.26, ε_0 is the vacuum permittivity, $\boldsymbol{\mu}_i$ and $\boldsymbol{\mu}_j$ are the point dipole vectors of the interacting pair, $\boldsymbol{r}$ and r are the distance vector and its magnitude, respectively. From

Equation 2.25, the corresponding force can be derived:

$$\boldsymbol{f}_{\mathrm{LJ}} = \left\{ \left[48\epsilon \left(\frac{\sigma}{r}\right)^{12} - 24\epsilon \left(\frac{\sigma}{r}\right)^{6} \right] \frac{1}{r^2} - \left[48\epsilon \left(\frac{\sigma}{r}\right)^{12} - 24\epsilon \left(\frac{\sigma}{r}\right)^{6} \right] \frac{1}{r_c^2} \right\} \boldsymbol{r}, \qquad (2.27)$$

from which we can see $\boldsymbol{f}_{\mathrm{LJ}}$ is vanishing at r_c (i.e. shifted to zero). Then, from Equation 2.26 the corresponding electrostatic force

$$\begin{aligned} \boldsymbol{f}_{\mathrm{Dip}} = {} & \frac{3}{r^5} \left[1 - 4 \left(\frac{r}{r_c}\right)^{3} + 3 \left(\frac{r}{r_c}\right)^{4} \right] \left[(\boldsymbol{\mu}_j \cdot \boldsymbol{r})\boldsymbol{\mu}_i + (\boldsymbol{\mu}_i \cdot \boldsymbol{r})\boldsymbol{\mu}_j - \frac{2}{r^2}(\boldsymbol{\mu}_i \cdot \boldsymbol{r})(\boldsymbol{\mu}_j \cdot \boldsymbol{r})\boldsymbol{r} \right] \\ & + \frac{3}{r^5} \left[1 - \left(\frac{r}{r_c}\right)^{4} \right] \left[(\boldsymbol{\mu}_i \cdot \boldsymbol{\mu}_j) - \frac{3}{r^2}(\boldsymbol{\mu}_i \cdot \boldsymbol{r})(\boldsymbol{\mu}_j \cdot \boldsymbol{r}) \right] \boldsymbol{r} \end{aligned} \qquad (2.28)$$

where it also can be proved that $\boldsymbol{f}_{\mathrm{Dip}}$ is shift to zero at r_c, and the pair torque to be identical to each other.

Chapter 3

Effects of Lamellar and Nonlamellar Lipid Composition on Bilayer Membranes

Biological bilayer membranes typically contain varying amounts of lamellar and nonlamellar lipids. Lamellar lipids, such as dioleoylphosphatidylcholine (DOPC), are defined by their tendency to form the lamellar phase, ubiquitous in biology. Nonlamellar lipids, such as dioleoylphosphatidylethanolamine (DOPE), prefer instead to form nonlamellar phases, which are mostly nonbiological. However, nonlamellar lipids mix with lamellar lipids in biomembrane structures that remain overall lamellar. Importantly, changes in the lamellar vs. nonlamellar lipid composition are believed to affect membrane function and modulate membrane proteins. In the presented work, we employ atomistic molecular dynamics simulations to quantify how a range of bilayer properties are altered by variations in the lamellar vs. nonlamellar lipid composition. Specifically, we simulate five DOPC/DOPE bilayers at mixing ratios of 1/0, 3/1, 1/1, 1/3, 0/1. We examine properties including lipid area and bilayer thickness, as well as the transmembrane profiles of electron density, lateral pressure, electric field, and dipole potential. While the bilayer structure is only marginally altered by lipid composition changes, dramatic effects are observed for the lateral pressure, electric field and dipole potential profiles. Possible implications for membrane function are discussed.

3.1 Introduction

The lipid bilayer plays many key structural and functional roles within biological membranes [227]. For example, it envelops cells, compartmentalizes the intracellular space, and acts as a selective barrier to permeation. The lipid bilayer also supports, and interacts with, numerous proteins. A detailed understanding of the properties of lipid bilayers is therefore central to biology, and is also relevant to many applications in the medical and pharmaceutical fields, ranging from biosensors [56, 306] to drug design and delivery [213, 246, 281]. Unfortunately, the current knowledge on lipid membranes is limited, especially with respect to molecular-level properties and phenomena. Membrane properties can exhibit significant variations as a function of depth inside the bilayer, yet measuring experimentally such variations can be extremely difficult, because of the membrane's very small thickness ($\sim$5 nm) compounded by high heterogeneity, disorder, and fluidity. A different, complementary approach to experimental investigation is represented by molecular dynamics (MD) computer simulation. In particular, MD has proven to be a powerful tool to study many aspects of biological membranes at the nanoscale [169, 198, 245, 258, 273].

In this chapter, we apply atomistic MD simulations to investigate a fundamental yet elusive area of membrane research, that is, the effect of lipid composition changes on membrane physical properties. More specifically, we focus on the effect of changes in the content of lamellar vs. nonlamellar lipids. It is well known that biological membranes are composed of a wide variety of lipid species, whose relative amounts are dynamically regulated [227]. The most prevalent lipid type observed in biological membranes is represented by glycerophospholipids, which can be further categorized into the lamellar or nonlamellar subtypes according to their inherent phase behavior. Dioleoylphosphatidylcholine (DOPC) and dioleoylphosphatidylethanolamine (DOPE) are two typical representatives of the lamellar and nonlamellar lipid families, respectively. Between DOPC and DOPE, there is a small yet crucial structural difference in the head groups, as illustrated in Figure 3.1a. Specifically, PC lipids comprise a choline group, characterized by three terminal methyl (CH_3) groups, whereas PE lipids comprise a smaller amine group (where hydrogen atoms replace the choline methyl groups of PC). Importantly, DOPC and DOPE exhibit substantially different phase behaviors. DOPC lipids preferentially

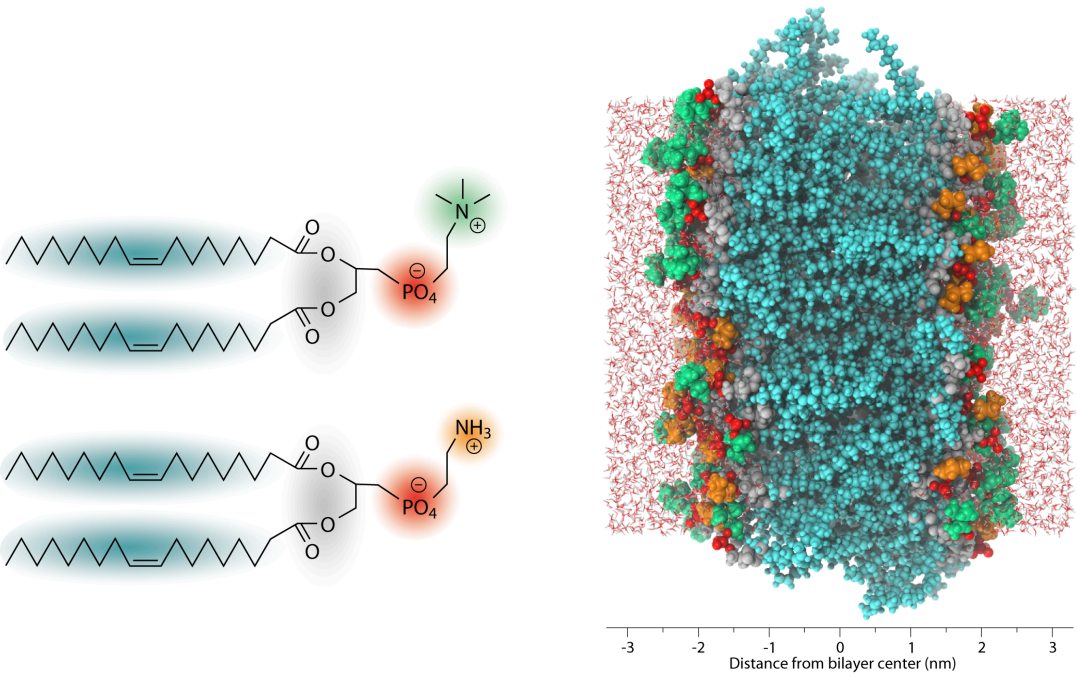

(a) (b)

Figure 3.1: Illustation of DOPC, DOPE and the mixed bilayer of them. (a) Molecular structures of DOPC (above) and DOPE (below). Colors highlight hydrocarbon tails (cyan), glycerol–ester groups (grey), phosphate groups (red), choline (green) and ethanolamine (orange). (b) A representative snapshot from our simulation of the mixed DOPC/DOPE (1/1 ratio) bilayer system (created using VMD [149]). Water molecules are depicted using a line representation, with oxygen and hydrogen colored red and white, respectively. Lipid molecules are represented using solid spheres, with molecular groups colored consistently with panel (a).

self-assemble into the lamellar phase, which is the predominant phase observed in real biological membrane. By comparison, if DOPE lipids are dispersed in water at biological conditions, a nonlamellar (inverse hexagonal) phase will be formed, in which water aggregates in columns lined by the lipid headgroups [116]. Despite such intrinsic tendency towards a phase that is mostly nonbiological, DOPE and other nonlamellar lipids are widespread in real biomembranes, where they mix with lamellar lipids to form phases which, importantly, are overall lamellar. It may then be asked what is the role of nonlamellar lipids in vivo, and whether their frustrated desire to transition from lamellar to nonlamellar phases has any effects. A first

intuitive explanation is that nonlamellar lipids are involved in membrane processes that require local nonlamellar structures (e.g., pores) to be formed, such as in cellular budding, fission or fusion [208, 227]. An additional hypothesis, less intuitive but potentially of great importance, points to the changes that nonlamellar lipids may induce on some key bilayer properties which will in turn control the behavior of the membrane and of any inclusions such as proteins [132, 208, 227, 353]. A significant and growing number of experimental studies have indeed provided evidence on how variations in the lamellar vs. nonlamellar membrane lipid composition can control biological functions, such as protein folding [71], lipid biosynthesis [17], protein channel conductance [212] and gating [353]. However, a quantitative understanding of the mechanisms involved is hindered by experimental difficulties in accessing the relevant molecular-scale properties.

Here, we perform atomistic molecular dynamics simulations to quantify relevant bilayer properties for mixed DOPC/DOPE systems at different relative compositions. In each bilayer studied, both leaflets contain the same amount of DOPC and DOPE lipids, that is, the lipid distribution is symmetric. It should be noted that lipid membranes in vivo can exhibit asymmetry of the lipid distribution across leaflets, and such asymmetry could have significant effects on the membrane's mechanical [205] and electrostatic properties. [129] However, the focus here is exclusively on symmetric bilayers.We first consider basic membrane structural quantities, including lipid area, lipid volume, membrane thickness and electron density. These fundamental membrane properties have been previously investigated by experiments and other simulations, especially for pure DOPC bilayers. However, much fewer data have been previously reported regarding mixed DOPC/DOPE bilayers; in particular, to our knowledge, no previous all-atom simulation of mixed DOPC/DOPE bilayers has been reported. We will then focus on the transmembrane profiles of lateral pressure, dipole potential, and electric field; these properties are expected to vary significantly according to the position (depth) inside the membrane, and are hypothesized to play crucial roles in numerous membrane functions (see Section 2.1.4).

Regarding the membrane lateral pressure profile, the key factor that determines its shape and magnitude is represented by the specific composition of the lipid bilayer. Importantly, small changes in the lipid composition can induce large variations in the pressure profile [52]. Previous simulation studies have focused on the effects

of including cholesterol [266] or changing unsaturation levels [241]. Regarding the effect of systematic composition changes within lamellar/nonlamellar lipid mixtures, previous results have been obtained only from simulation of a simple coarse-grained model [251]. Perrin et al. [269] have reported the pressure profile for a single composition (1/1) of a POPG (lamellar) / POPE (nonlamellar) lipid mixture by employing the atomistic CHARMM36 lipid force field (as in this study). As far as we are aware, no previous atomistic MD study has been reported on pressure profiles from a range of compositions of lamellar-nonlamellar mixed bilayers modeled with atomistic force fields.

Regarding the dipole potential, previous studies have considered the effect of lipid composition changes on it by focusing on the headgroup type [333], ether or ester linkage type [322], and double bonds in the chain region [254]. Regarding lamellar/nonlamellar systems, previous investigations include a few experiments [272, 311, 333], a coarse-grained simulation study [251], but no atomistic simulations.

In the remainder of this chapter, we report on a series of all-atom MD simulations aimed at quantifying the effects of changes in the lamellar vs. nonlamellar lipid content on membrane physical properties. It will be shown that the bilayer structure is relatively constant across the different systems, while the lateral pressure, dipole potential, and electric field profiles exhibit high sensitivity to composition.

3.2 Methods

3.2.1 Bilayer systems

Five bilayer systems were considered, comprising two pure DOPC and DOPE systems, and three mixed systems of varying DOPC/DOPE composition ratio. Table 3.1 details the composition of each system, and a snapshot from a simulation of a representative mixed bilayer is shown in Figure 3.1b. All systems were fully hydrated with 4300 water molecules (water/lipid ratio $\sim$33.6) [232]. It should be noted that under the studied conditions the pure DOPE system experimentally forms a nonlamellar (inverse hexagonal) phase [116]. However, in our simulation the preassembled bilayer system maintains a lamellar structure, most likely because of the relatively small system size and the constraints imposed by the periodic

Table 3.1: Composition of the simulated bilayer systems

System	N_{DOPC}	N_{DOPE}	N_{water}	N_{atoms}
DOPC	128	0	4300	30564
DOPC/DOPE (3/1)	96	32	4300	30276
DOPC/DOPE (1/1)	64	64	4300	29988
DOPC/DOPE (1/3)	32	96	4300	29700
DOPE	0	128	4300	29412

N_{DOPC} and N_{DOPE} represent the number of DOPC and DOPE molecules, respectively; N_{water} indicates the number of water molecules; N_{atoms} indicates the total number of atoms.

boundary condition. While the simulated lamellar DOPE bilayer is thus rather artifactual, it will prove useful for providing a more complete and systematic data set, and to corroborate any observed composition-dependent trend. In fact, atomistic simulations of pure lamellar DOPE bilayers have also been used previously [330, 331, 362].

It is nonetheless of interest to investigate whether the CHARMM36 force field can indeed predict the correct DOPE phase when the constraints of a preassembled system are removed. To this end, we have conducted a self-assembly test starting from a random solution of DOPE lipids and water, and we have been able to observe the formation of an inverse hexagonal phase, in agreement with the known experimental behavior. Full details of these simulations are reported in the end of this chapter.

3.2.2 Simulation details

The starting structures of the bilayers were built using Packmol [215]. Regarding the force field parameters, the CHARMM36 all-atom lipid force field [173] and the CHARMM TIP3P (TIPS3P) water model [41, 97] were adopted. Molecular dynamics simulations were carried out using the LAMMPS program (version 11 Nov 2013) [2, 274]. Simulation input files were generated using the *charmm2lammps.pl* tool available in the LAMMPS distribution and the *psfgen* plugin of VMD [149]. The initial structures were energy minimized to remove potentially problematic close contacts between atoms. Each system was then simulated for a total of 1 μs. The temperature was controlled at 303 K by applying the Langevin thermostat [313]

with a collision frequency of 1 ps^{-1}. The barostat by Berendsen et al. [29] was used to maintain the system pressure at 1 atm, with a damping time of 1 ps and an isothermal compressibility of 4.6×10^{-5} atm^{-1}. The pressure was controlled semi-isotropically, that is, the z-component (perpendicular to the bilayer plane) of the pressure tensor was controlled independently from the other two (coupled) components along the x- and y-axes (parallel to the bilayer plane). Periodic boundary conditions were applied in all 3 dimensions. The SHAKE algorithm was applied, with a relative tolerance of 10^{-5}, to constrain all the bonds involving hydrogen atoms, as well as the H–O–H angle in water. The integration timestep was 2 fs. At every step, the net momentum of the mass center of the entire system was removed to prevent any drifting [137] Nonbonded Lennard-Jones interactions were cut off beyond 10 Å, and the standard switching function in CHARMM was applied from 8 to 10 Å [201]. Electrostatic interactions were computed using the PPPM (particle-particle particle-mesh) method [143], with a relative error tolerance of 10^{-5}, and a real space cutoff of 10 Å. [242] Intramolecular nonbonded interactions were considered according to the CHARMM convention, that is, interactions between atoms separated by less than three bonds (so-called 1–2 and 1–3 terms) were skipped, and 1–4 interactions were weighted according to the atoms types [201].

3.2.3 Data analysis details

Data analysis was performed on the last 800 ns of each simulation, while the first 200 ns were regarded as equilibration. All targeted quantities were collected every 20 ps. Statistical uncertainties were estimated by the block averaging procedure [109, 292], with a block size of 20 ns. Error estimation analyses are shown in 3.2 for the calculated area per lipid of the pure DOPC system, as a representative example. The error estimation evaluated the variances from a series of blocking averages with successive block sizes to decide the appropriate block size to average the properties sampled in the course of our simulations. With the block size getting larger, σ^2 increases until a plateau is reached, where the block size is around 20 ns. Thus, we chose 20 ns as the basic block size to do statistic analysis in this work.

For the transbilayer profiles, symmetrization were performed with respect to the bilayer center by averaging over the two monolayers. Calculation details for specific

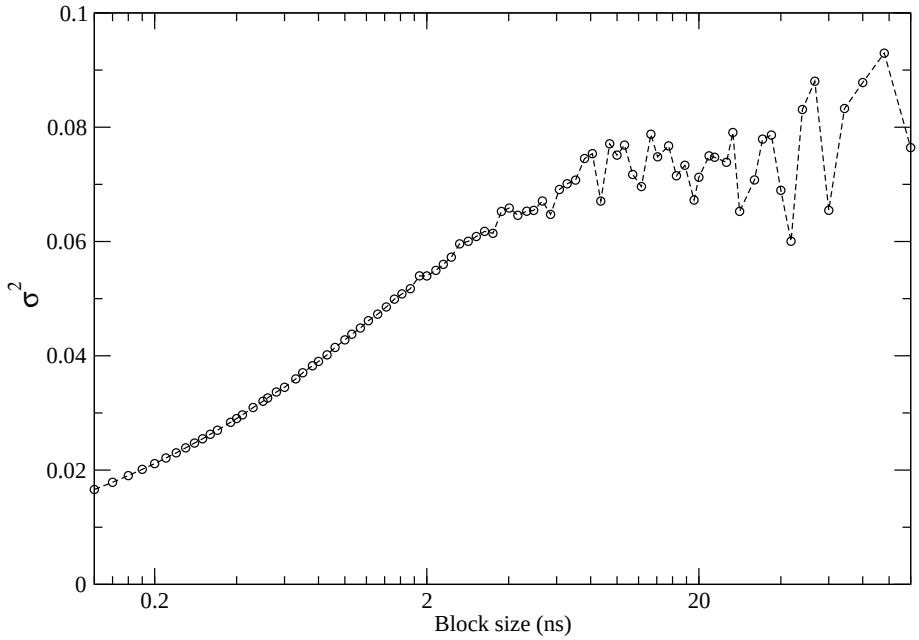

Figure 3.2: Block-averaged error estimation for the area per lipid calculated for the pure DOPC system. σ^2 stands for the variance calculated between data blocks with a certain block size.

properties are described in the following sections.

Structural properties

The area per lipid, volume per lipid and bilayer thickness were calculated following previously reported protocols [252, 273]. The average area per lipid (A_{L}) is defined as the cross-section area of the whole system along the bilayer surface plane (xy-plane) divided by the number of lipids in each monolayer (64 in our systems). The average volume per lipid is defined as $(V_{\mathrm{box}} - V_{\mathrm{water}})/N_{\mathrm{L}}$, where V_{box} is the volume of the whole simulation box, V_{water} is the volume occupied by the water molecules, and N_{L}=128 is the total number of lipids in our systems. The bilayer thickness d_{HH} is obtained from the peak to peak distance in the electron density profile.

Lateral pressure profile

To calculate the lateral pressure (or stress) distribution across the bilayer, the simulation box was first discretized into thin slabs parallel to the xy plane. The

thickness of each slab was set to 1 Å. For a slab centered at depth z, the lateral pressure profile $\Pi(z)$ is defined as [240, 251]:

$$\Pi(z) = \frac{P_{\mathrm{xx}}(z) + P_{\mathrm{yy}}(z)}{2} - P_{\mathrm{zz}}(z) \tag{3.1}$$

where $P_{\mathrm{xx}}(z)$, $P_{\mathrm{yy}}(z)$ and $P_{\mathrm{zz}}(z)$ are the diagonal elements of the pressure tensor. Owing to the symmetry of the system with respect to the direction normal to the bilayer, the tangential pressures are expected to converge to identical values, that is, $P_{\mathrm{xx}}(z) = P_{\mathrm{yy}}(z)$, hence only either of the two is strictly needed for the calculation. However, in practice, both of them were calculated and the average of the two was used, thus improving the calculation precision. The normal component $P_{\mathrm{zz}}(z)$ was assumed constant and equal to the external pressure ($P_{\mathrm{zz}}(z) = 1$ atm) for all slabs; this condition, required by mechanical equilibrium [359], is also consistent with previous work [251, 330]. The contributions to the pressure in each slab from the various interactions were accumulated following the approach by Harasima [135], as in previous work [250, 251].

Dipole potential and electric field profiles

The dipole potential profile $\Psi(z)$ was calculated from the charge density distribution $\rho(z)$ along the direction normal to the bilayer plane. To obtain $\rho(z)$, the systems were again subdivided into 1 Å thick slabs, and the atomic (partial) charges were accumulated and averaged in each slab. The relation between $\Psi(z)$ and $\rho(z)$ is defined by Poisson's equation:

$$\frac{\mathrm{d}^2\Psi(z)}{\mathrm{d}z^2} = -\frac{\rho(z)}{\varepsilon_0}, \tag{3.2}$$

so the dipole potential can be calculated as [242, 250, 322]:

$$\Psi(z) = -\frac{1}{\varepsilon_0}\int_{z_0}^{z}\int_{z_0}^{z'} \rho(z'')\mathrm{d}z''\mathrm{d}z', \tag{3.3}$$

where the constant ε_0 is the electrostatic permittivity in vacuum, and z_0 is the reference position where the potential is set to zero, which in our calculations corresponds to the center of the water region. The electric field $E(z)$ projected

on the z direction can be obtained as the negative of the spatial derivative of the dipole potential, i.e., $E(z) = -\,\mathrm{d}\Psi(z)/\mathrm{d}z$.

3.3 Results and discussion

3.3.1 Structural properties

The calculated area per lipid (A_L), volume per lipid (V_L) and the bilayer thickness (d_HH) of the simulated systems are shown in Figure 3.3, together with available literature data from experiments and from simulations of the same all-atom force field used in this work. Numerical values for A_L, V_L and d_HH from our simulations are tabulated in 4.1.

Table 3.2: Structural properties of the DOPC/DOPE bilayer systems. Results are shown in the 'mean ± standard error' format.

System	A_L (Å^2)	V_L (Å^3)	d_HH (Å)
DOPC	69.82 ± 0.14	1289.83 ± 0.62	37.07 ± 0.10
DOPC/DOPE (3/1)	67.63 ± 0.17	1275.17 ± 0.60	37.81 ± 0.15
DOPC/DOPE (1/1)	65.81 ± 0.15	1260.47 ± 0.61	38.40 ± 0.14
DOPC/DOPE (1/3)	64.51 ± 0.18	1245.86 ± 0.81	38.75 ± 0.14
DOPE	63.42 ± 0.17	1231.23 ± 0.60	39.13 ± 0.16

It can be seen from Figure 3.3a that the area per lipid A_L decreases with the presence of increasing amounts of DOPE; this trend is intuitive considering the smaller size of the DOPE headgroup with respect to DOPC (see also Figure 3.1a). However, it is important to note that, quantitatively, the effect is rather small. In fact, the net reduction in A_L from comparing the extreme cases of pure DOPC to pure DOPE is only ∼9%. Figure 3.3a also shows that our results fall within the range of the various data previously reported in the literature.

Regarding the lipid volume V_L, our results again show a decreasing trend in response to increasing the DOPE content (Figure 3.3b). The actual differences between the different systems are however very small, with a maximum volume decrease of ∼5% when comparing the pure DOPC and DOPE systems. Figure 3.3b also shows that our value for pure DOPC is marginally smaller (to within 1%) than

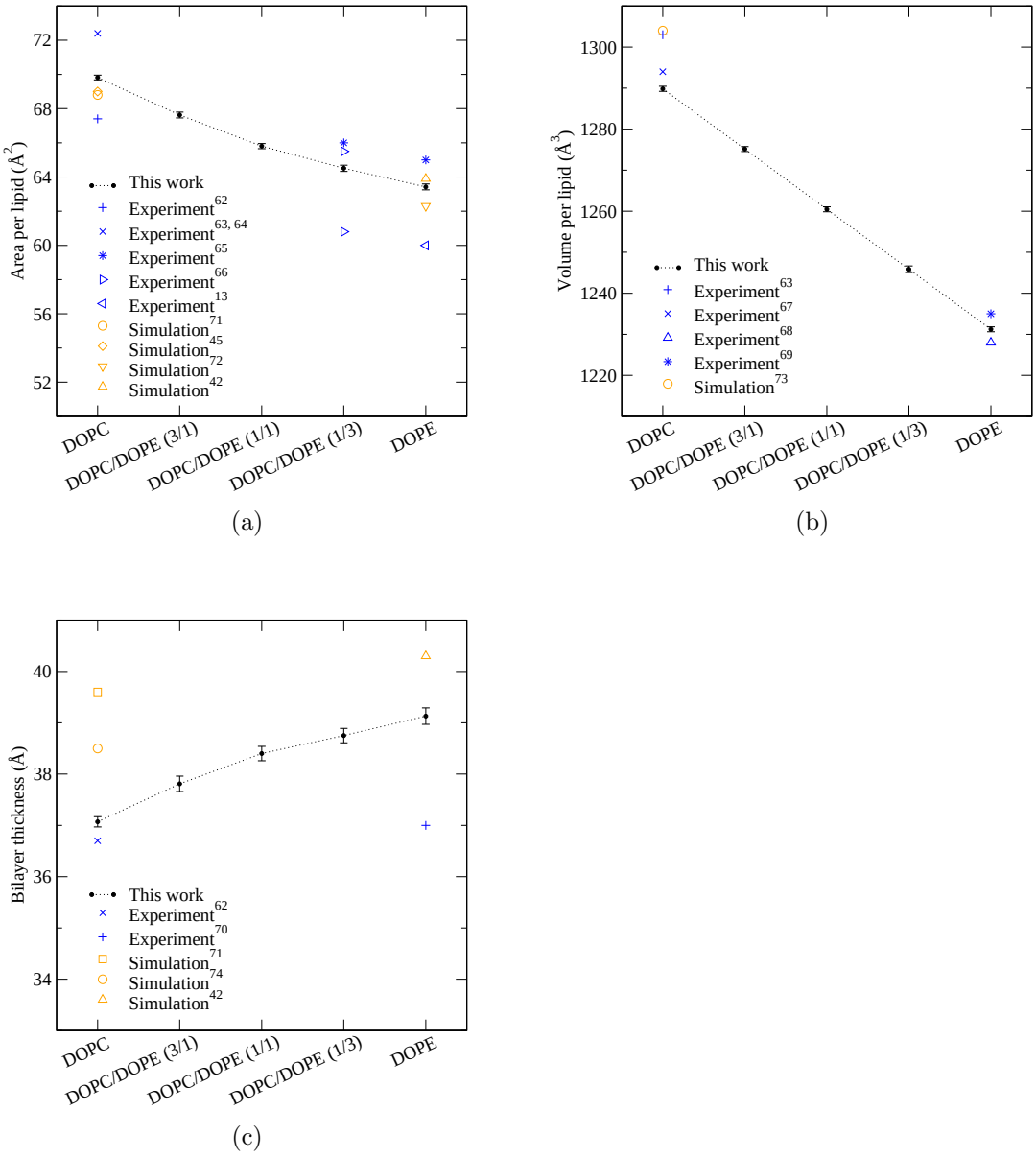

Figure 3.3: Structural properties: area per lipid (a), volume per lipid (b), bilayer thickness(c). Error bars represent standard deviations. Literature data are superimposed from experiments (for A_{L} [116, 178, 179, 261, 290, 291], V_{L} [65, 122, 179, 289] and d_{HH} [124, 178]) and CHARMM36 simulations (for A_{L} [173, 190, 294, 362], V_{L} [288] and d_{HH} [294, 362, 370]). Note that not all the literature values were obtained at the same temperature as for this work (303 K), but still in a comparable range (275 K to 318 K) consistent with a fluid phase for the lipids considered.

the available literature data, while there is an almost exact match with experiments for pure DOPE.

The data obtained for the bilayer thickness d_{HH} are displayed in Figure 3.3c. It can be seen that d_{HH} systematically increases with addition of DOPE. Quantitatively however, the changes in thickness corresponding to composition changes are very small, consistently with previous observations for A_{L} and V_{L}. In fact, the difference between the pure DOPC and DOPE systems is only $\sim$5%. A comparison with literature data highlights that all the CHARMM36 simulation results (including ours) overestimate the experimental measurements for the only two systems for which d_{HH} has been previously reported, i.e., pure DOPC and DOPE.

To characterize the relation between changes in the structural properties and corresponding changes in lipid composition, we performed a least squares fitting analysis of the data from this work reported in Figure 3.3. Table 3.3 reports linear and quadratic fitting results for the structural properties in relation with the DOPC/DOPE composition, together with the p values (the probability to reject the fitted model). In each fitted formula, variable Y stands for the property value, while the lipid composition is quantified by X, defined as the DOPE fraction normalized in the range between 0 and 1. For example, $X = 0$ represents the pure DOPC system and $X = 0.5$ represents the DOPC/DOPE (1/1) system. All fittings were performed applying the weighted least squares method [374], to take into account the measurement errors at each X value (i.e., at each composition). Then chi-squared tests [295] were performed to test the statistical significance. The results obtained indicate that the change in the lipid volume follows a linear relation with a high level of significance, while for lipid area and bilayer thickness the relations are best described by quadratic functions, although the level of significance is somewhat low. While the linearity of the lipid volume changes is intuitive, the nonlinearity for lipid area and thickness is not. However, the origin of such nonlinear behavior is unclear. In a previous investigation, de Vries et al. [80] obtained a trend similar to ours for the A_{L} change with DOPC/DOPE composition, and they attributed this to the combined effect from head group size difference, electrostatic interactions, and hydrogen-bonding capability. However, it must be noted that the atomistic model used in that study [80] was supplemented with a repulsive potential between the H atoms of the PE amine group and all other atoms, and it is not clear how this ad

Table 3.3: Fitted relations and statistical analyses for the structural properties

Property	Linear fit	Quadratic fit
A_{L} (Å^2)	$Y = -6.49X + 69.49$	$Y = 3.15X^2 - 9.52X + 69.81$
	$(p = 0.9350)$	$(p = 0.0482)$
V_{L} (Å^3)	$Y = -58.58X + 1289.80$	$Y = 0.12X^2 - 58.70X + 1289.81$
	$(p = 0.0002)$	$(p = 0.0006)$
d_{HH} (Å)	$Y = 2.12X + 37.16$	$Y = -1.12X^2 + 3.14X + 37.08$
	$(p = 0.2727)$	$(p = 0.0630)$

hoc modification may have influenced the trend reported.

Overall, experimental evidence on the effect of systematic composition changes appears necessary to validate the findings from simulations; unfortunately however, measurements reported to date are rather scattered, as it can be seen from Figure 2.

The electron density profiles are shown in Figure 3.4. As expected from the previously reported structural results, the electron densities are characterized by very minor differences across the different compositions. In particular, with increasing DOPE content the peaks in the head group region shift slightly out towards the water phase (consistent with the previously observed increase in d_{HH}), by a maximum of 0.1 nm when comparing pure DOPC and DOPE. The peak magnitudes are effectively unchanged across the different systems, while the central minimum decreases marginally, by at most $\sim$0.01 e nm^{-3} when comparing pure DOPC to DOPE.

3.3.2 Lateral pressure profile

The lateral pressure profiles $\Pi(z)$ for the bilayer systems investigated are shown in Figure 4.5. In general, it can be noted that all the profiles display similar overall qualitative features. Upon entering the bilayer from the outer water phase, the lateral pressure rises sharply and forms large positive peaks located roughly at the interface between the water and lipid heads regions. Positive values of the lateral pressure profile generally indicate repulsive forces, acting to enlarge the area of the bilayer. At the water-heads interface, a net repulsion is obtained from

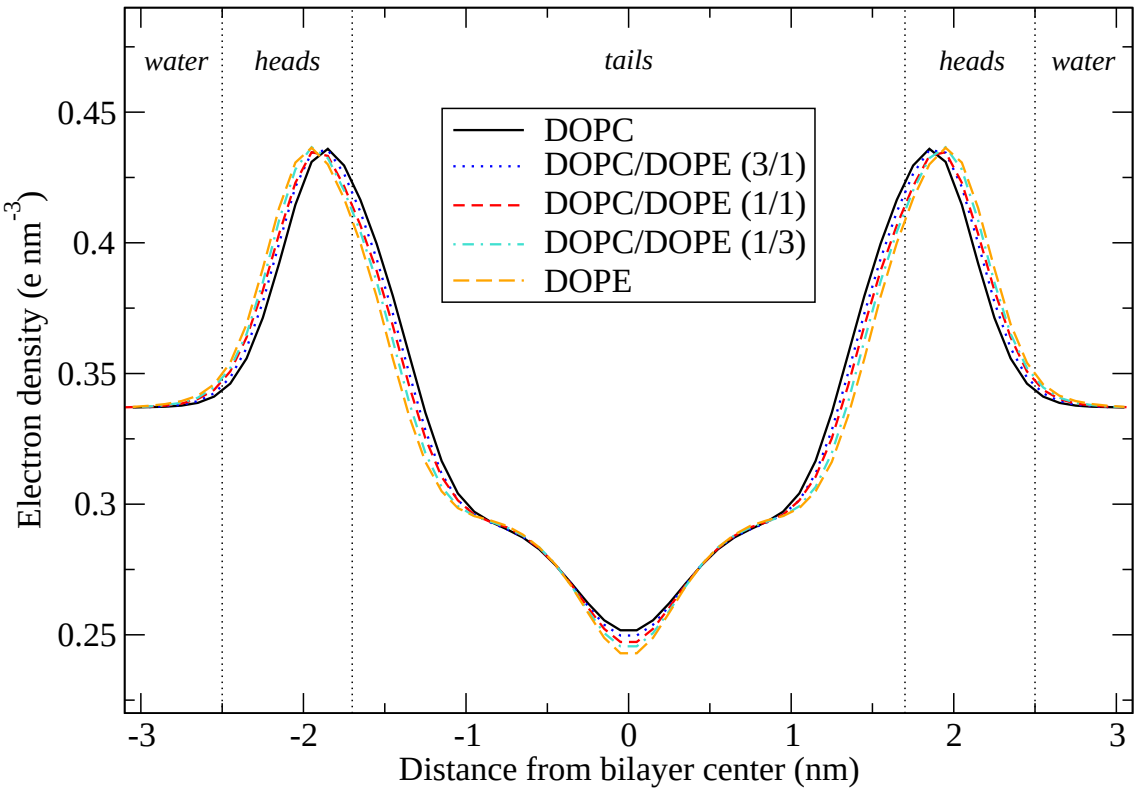

Figure 3.4: Electron density profiles. Vertical dotted lines indicate approximate boundaries between regions occupied predominantly by *water*, lipid *heads*, and hydrocarbon *tails*.

intermolecular contributions of steric, electrostatic, and hydration nature [57]. Upon moving deeper inside the bilayer, the lateral pressure drops drastically, forming deep troughs approximately at the interface between the lipid heads and tails regions. In general, negative pressures correspond to the presence of intermolecular attractive forces, that act to reduce the bilayer area. In fact, this location corresponds to an interface involving a hydrophobic environment (the hydrocarbon tail region) with a strong tendency to reduce and minimize its area in contact with a hydrophilic environment (comprising water and lipid heads). The lateral pressure troughs can thus be seen as a reflection of the hydrophobic effect, whereby hydrophobic molecules cluster together in order to restrict their exposure to water. In the central part of the profiles, corresponding to the hydrocarbon core of the bilayers, the lateral pressure is mostly positive, comprising three peak regions with two corresponding local minima

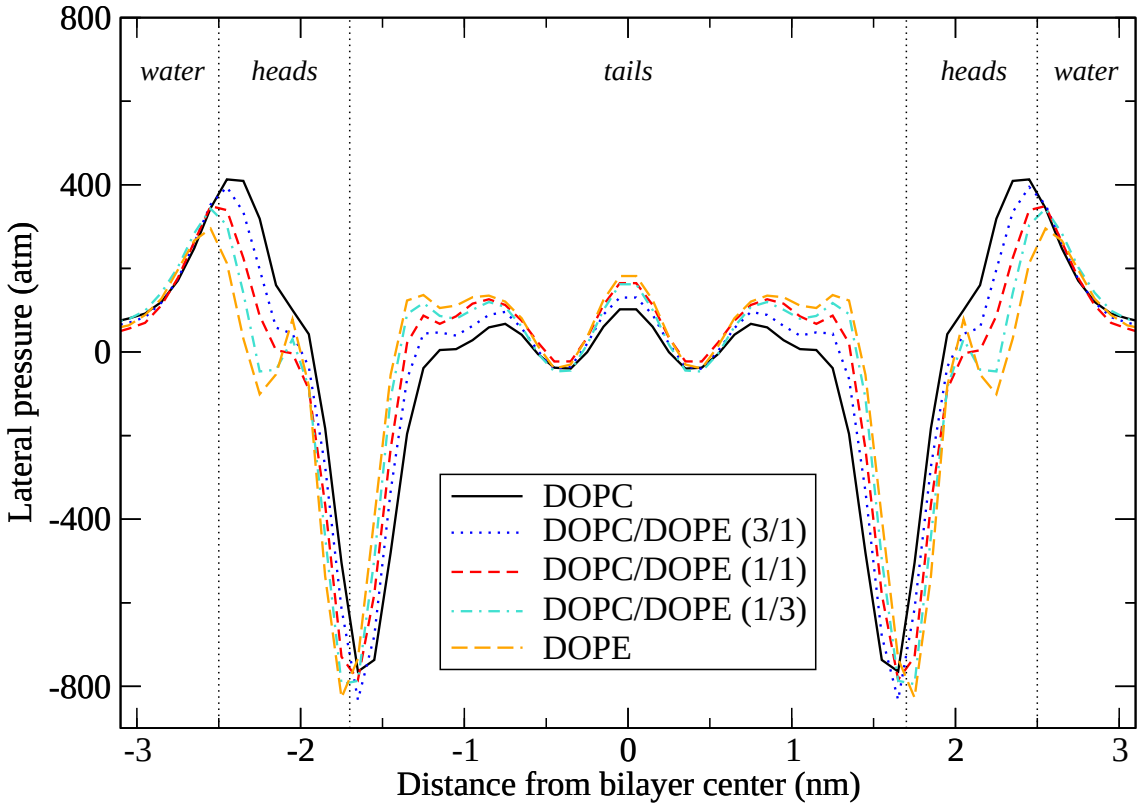

Figure 3.5: Lateral pressure profiles ($\Pi(z)$). Vertical dotted lines indicate approximate boundaries between regions occupied predominantly by *water*, lipid *heads*, and hydrocarbon *tails*.

in between. The repulsive forces giving rise to the tails pressure are typically explained in terms of entropy losses [52]. In particular, the tight molecular packing in the bilayer core forces the lipid tails to stretch (therefore losing entropy compared to isolated 'free' tails), ultimately causing substantial tail-tail repulsion [24, 230].

While all the profiles are similar qualitatively, remarkable quantitative differences and trends can be observed and related to changes in the lipid composition. Regarding the peaks at the interface between the water and lipid heads regions, corresponding to a distance of about 2.5 nm from the bilayer center, a top pressure of ∼410 atm is observed for the pure DOPC system. With the presence of increasing ratios of DOPE in the mixed systems, the peak pressure systematically decreases, reaching its lowest value for the pure DOPE system, at ∼290 atm. The presence of growing amounts of DOPE also causes the main peaks to shift slightly outwards,

towards the water region; this correlates with the small increase in bilayer thickness noted earlier (Figures 3.3c and 3.4). For the two systems with highest DOPE content, i.e., DOPC/DOPE (1/3) and pure DOPE, the emergence of a pair of local peaks and troughs can also be observed in the middle of the lipid heads region. The local troughs, at 2.25 nm from the bilayer center, markedly enhance the pressure drops at the same location compared to DOPC; such drops amount to ∼350 atm for DOPC/DOPE (1/3) and ∼400 atm for pure DOPE. Regarding the main troughs, located at a distance of ∼1.7 nm from the bilayer center, it can be seen that the minima in the pressure fall in a relatively narrow range between ∼−760 to ∼−830 atm, without any systematic trend related to the DOPC/DOPE ratio. Composition-dependent effects are again apparent in the hydrocarbon tail core of the bilayers, where increasing the DOPE ratio systematically increases the lateral pressure, up to 80 atm for the central peak, and up to ∼100 atm towards the top end of the tails (at ∼1 nm from the bilayer center), when comparing pure DOPC and DOPE.

To conduct a further quantitative assessment of the effect of the lipid composition on the pressure profile, we carried out an analysis in terms of the main 'integrated contributions' [208]. In particular, we first subdivided the profile into three main sections (Figure 3.6a): i) the headgroup ('hg') section corresponding to the part of the profile characterized by the positive pressure in the water and lipid heads regions; ii) the hydrophobic ('hg') section characterized by the negative pressure corresponding to the main troughs; iii) the chains ('ch') section corresponding to the positive pressure in the hydrocarbon tails (or chains) region. For each of these sections, we calculated the integrals of the lateral pressure profiles, as illustrated in Figure 3.6a. By integrating the pressure from key regions of the profiles, it is possible to capture the combined effect of peak magnitudes and peak widths, as obviously the integrals correspond to the areas under the curve for the related sections. The composition-dependent results obtained for the different bilayer systems are plotted in Figure 3.6b. First of all, it can be verified that, irrespective of the lipid composition, the sum over the three components is always zero, meaning that the integrals of the individual sections balance out, as required by mechanical equilibrium. Regarding the headgroup integral π_{hg}, it can be seen that it decreases together with the presence of increasing amounts of DOPE, a trend which is consistent with the previously observed decrease in peak pressures in the same region (Figure 4.5).

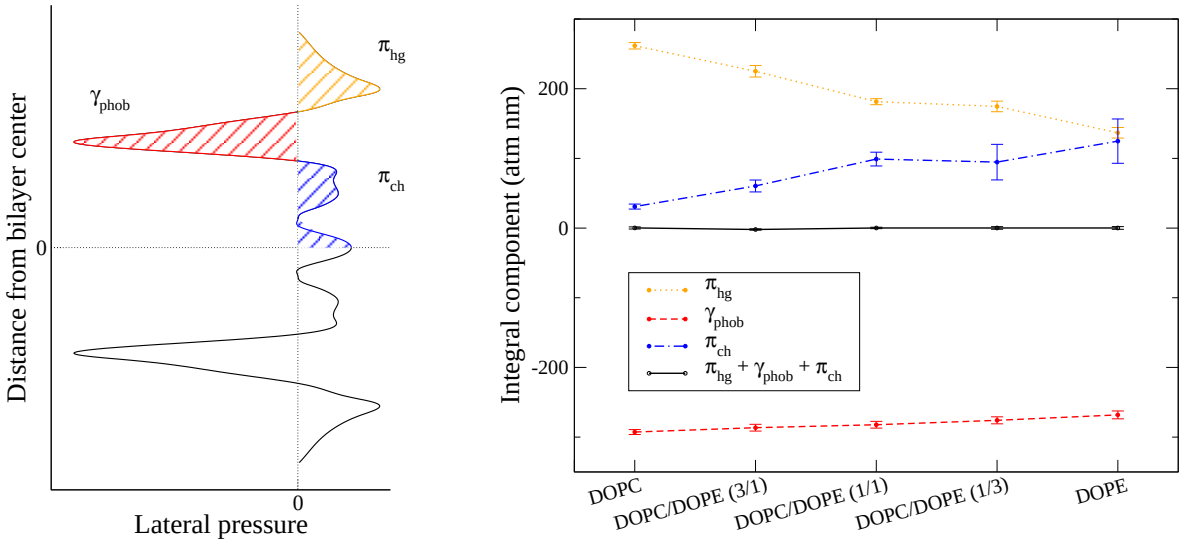

(a) (b)

Figure 3.6: Integrals of different sections of the lateral pressure profile. (a) A schematic illustration of the quantified contributions. (b) Results obtained (error bars represent standard deviations).

In particular, π_{hg} decreases by almost 50% from the pure DOPC system to pure DOPE. The trend observed for π_{hg} is countered by the chains integral π_{ch}, which displays an enormous increase in relative terms, of approximately 400%, from the pure DOPC to the pure DOPE system as a result of DOPE addition. Since it has been estimated that even a 10% change in the chains pressure can induce a very large shift in the conformational equilibrium of membrane proteins [52], our results suggest that even small shifts in the DOPC/DOPE composition can have significant biological repercussions. Incidentally, it has been proposed [208] that the relative size of the headgroup and chain contributions to the lateral pressure leads to the relation $\pi_{\mathrm{hg}}/\pi_{\mathrm{ch}} \approx 1$, which is consistent with the value of 1.1 ± 0.3 from our data. The hydrophobic integral γ_{phob} represents the interfacial tension acting at the polar–apolar interface [208]. It can be seen that the absolute value of γ_{phob} decreases slightly with increasing DOPE ratio; in particular, we observe an overall reduction of ∼9% from pure DOPC to pure DOPE. Such a reduction in interfacial tension reflects the slight decrease in the polar–apolar interfacial area observed previously (Figure 3.3a).

3.3.3 Dipole potential profile

The dipole potential profiles $\Psi(z)$ are displayed in Figure 3.7. It can be noticed that all the profiles share similar qualitative features, irrespective of the different lipid compositions. However, it is clear that there are substantial composition-dependent differences in the magnitude of the potentials. In particular, an evident trend can be observed, whereby increasing amounts of DOPE induce increasingly larger values of $\Psi(z)$ across the entire profile. Starting from the reference value of 0 mV in the water phase, $\Psi(z)$ rises sharply across the lipid heads region, up to peak values from 441 ± 26 mV for DOPC to 545 ± 24 mV for DOPE, with the mixed systems displaying values distributed in between. These peaks are located at ∼1.3 nm from the bilayer center, corresponding to the top part of the lipid tails, near the glycerol-ester groups. The profiles can then be observed to drop and form local minima at ∼0.8 nm from the bilayer center, a region roughly corresponding to the double bond midway along the hydrocarbon tails. In the bilayer center, the dipole potential reaches a global maximum with values ranging from 582 ± 28 mV for DOPC to 712 ± 25 mV for

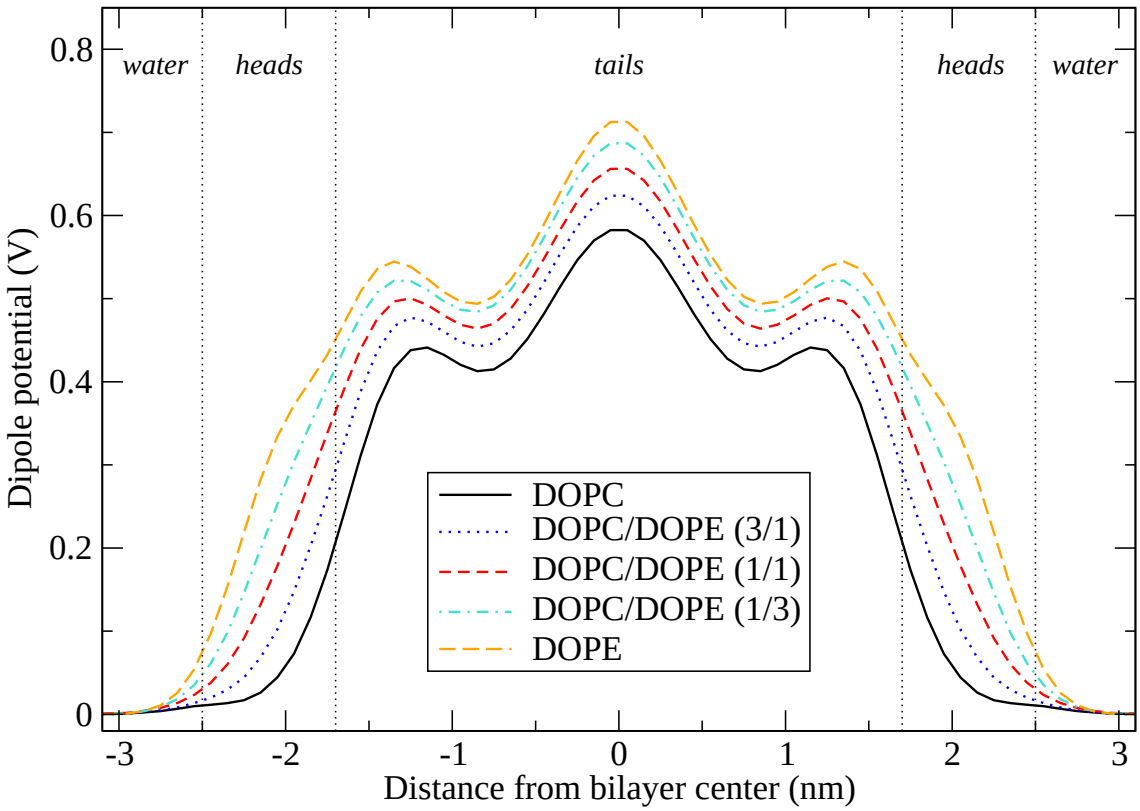

Figure 3.7: Dipole potential profiles $\Psi(z)$. Vertical dotted lines indicate approximate boundaries between regions occupied predominantly by *water*, lipid *heads*, and hydrocarbon *tails*.

DOPE, corresponding to an increase of 22%.

The profile obtained for the pure DOPC bilayer is consistent with the profile reported by Warshaviak et al. [370] from simulation of DOPC with the same force field used in our work (CHARMM36), as expected. Regarding the mixed DOPC/DOPE bilayers, we are not aware of any previous dipole potential data from either atomistic simulations or experiments. There are however some experimental studies on single-component bilayers. Specifically, earlier measurements by Pickar et al. [272] indicated values of 0.224 V and 0.215 V for DOPC and DOPE bilayers, respectively. These results have been more recently amended by Schamberger and Clarke [311] to include a more accurate estimate of hydration energies, yielding updated values of 0.343 V for DOPC and 0.334 V for DOPE [311]. Regardless of the correction, both sets of data indicate a (marginally) larger potential for DOPC

compared to DOPE, which is in contrast to the trend observed in our simulation results. However, more recent data by Starke et al. [333] showed an increase in the dipole potential, from 0.410 V to 0.461 V, when comparing a pure DMPC system to an equimolar mixture of DMPC and DMPE, in qualitative agreement with our results (note that DMPC/DMPE and DOPC/DOPE are characterized by differences which are small and localized in the hydrocarbon region, thus it is acceptable to make a qualitative comparison in relation to their dipole potential). In any case, it is not clear how reliable the experimental estimates are, given the well-known difficulties in measuring the dipole potential, and especially in relation to ranking different values from PC vs. PE systems. In fact, all three reported PC/PE pairs of experimental values are very close to each other, with a level of uncertainty that in one case [333] has been reported to be much larger ($\sim$ 0.15 V) than the actual difference in PC vs. PE values (0.05 V). No uncertainty estimates were reported for the other data [272, 311], but the differences in PC vs. PE values are so small (0.009 V in both cases) that they are very much likely to be smaller than the uncertainty in the measurements.

In general, it should be noted that the experimental estimates for the dipole potential tend to be markedly lower than the simulation values. This is a well-known issue, consistently observed in previous atomistic simulations of lipid bilayers [173, 277, 322, 328, 365, 370]. The discrepancy with respect to the experimental values has been ascribed, at least in part, to the lack of electronic polarizability in standard atomistic force fields [365].

To further investigate the molecular origin of $\Psi(z)$, as well as the effect of changing the lamellar-nonlamellar lipid ratio, we isolated the two separate contributions to $\Psi(z)$ from the water and lipid molecules. Results for such individual components are plotted in Figure 3.8, together with the net profiles (already reported in Figure 3.7) for reference. For all systems, it can be seen that the total net potential results from a competition between much larger positive and negative contributions due to water and lipids, respectively. This is generally consistent with previously reported data from atomistic simulations of pure DOPC systems [328, 370]. In the only previously reported simulation study on DOPC/DOPE mixed bilayers, the lipid dipoles (rather than water) were the main contributors to the total potential, and composition-related trends were also different from those observed here [251]. However, that

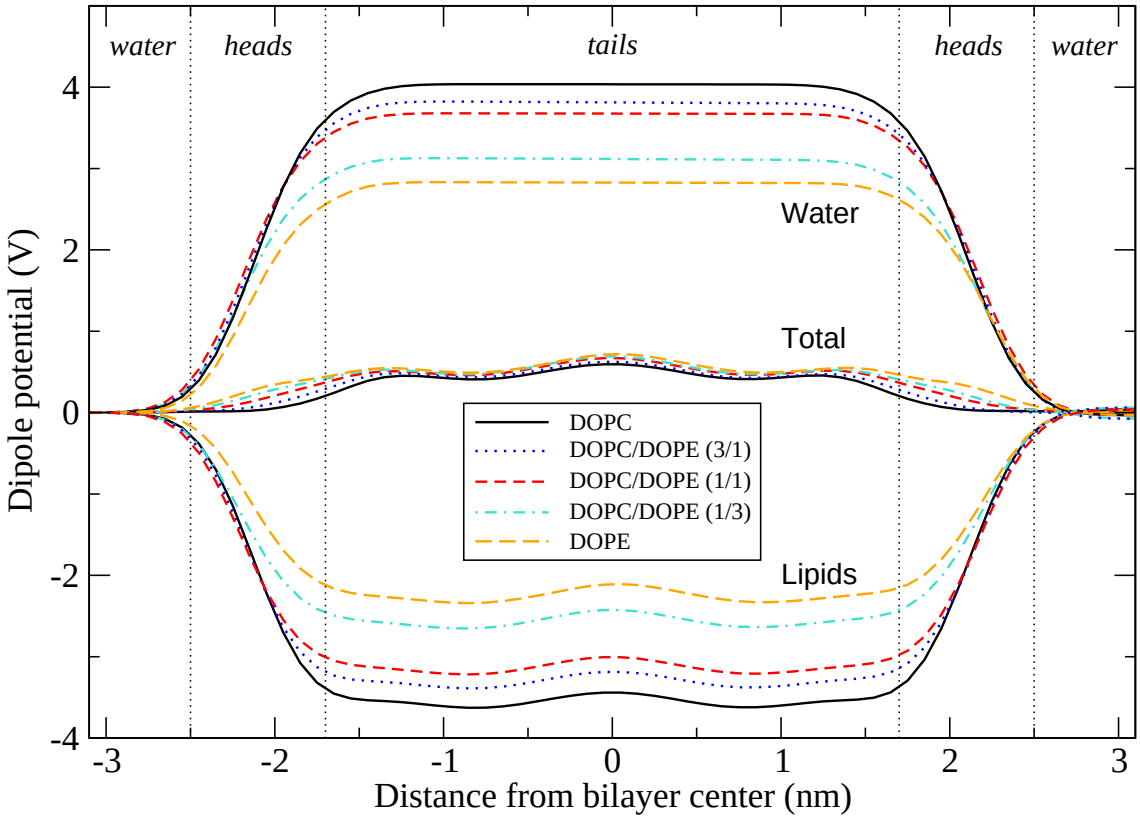

Figure 3.8: Individual contributions of the dipole potential profile from water and lipid molecules. The total net potentials are also plotted for reference (see Figure 3.7 for dedicated plot). Vertical dotted lines indicate approximate boundaries between regions occupied predominantly by *water*, lipid *heads*, and hydrocarbon *tails*.

study [251] employed a coarse-grained model which treats water molecules as single point dipoles without explicit hydrogen bonding capabilities [90, 244], and hence the preferential alignment of water in the heads region (which determines the electric field) may not be accurately reproduced. The atomistic simulations reported here allow new quantitative insights to be obtained into composition-dependent effects. Specifically, Figure 3.8 shows that while the water contribution determines the positive sign of the overall net profiles, their composition-dependent trend is dictated by the lipid contributions. In fact, the observed increase in the overall net dipole potential brought about by the presence of increasing amounts of DOPE is determined by the lipid relative contributions overcompensating the water contributions (which instead display decreasing potential values with increasing DOPE ratios).

3.3.4 Electric field

The projection of the electric field along the direction normal to the bilayer plane is reported in Figure 3.9. Note that the curves are antisymmetrical, due to the

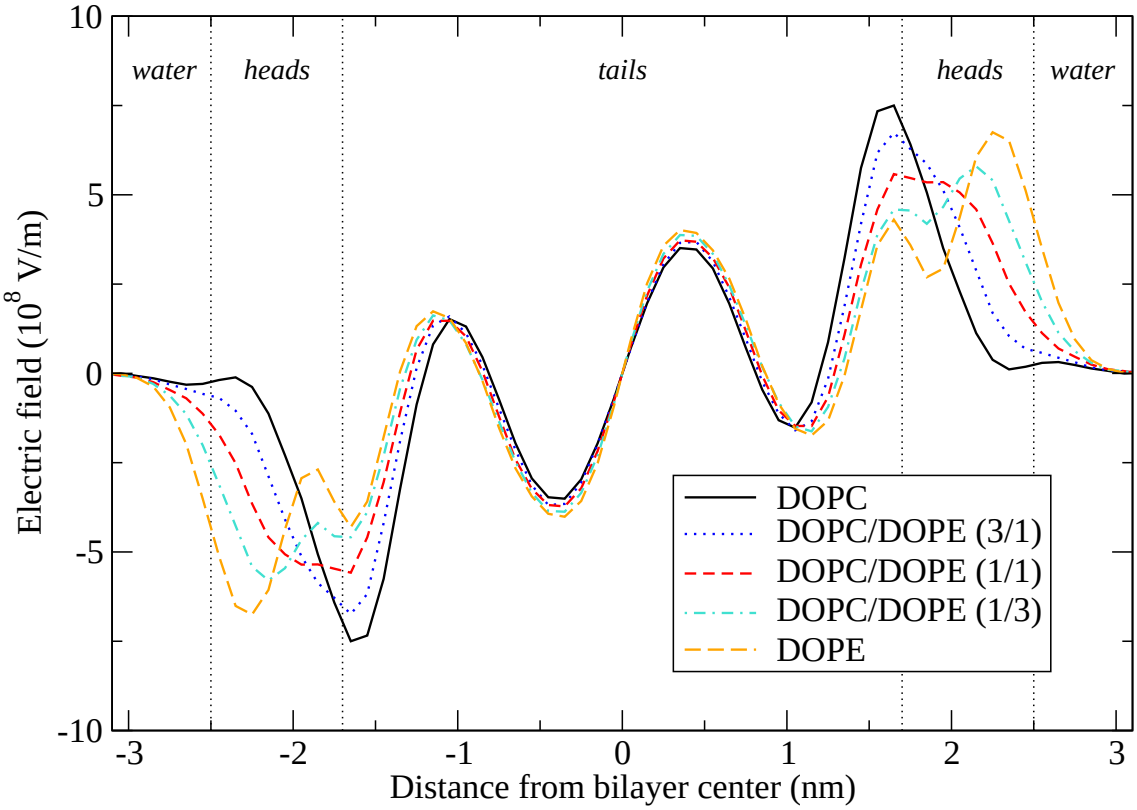

Figure 3.9: Electric field $E(z)$. Vertical dotted lines indicate approximate boundaries between regions occupied predominantly by *water*, lipid *heads*, and hydrocarbon *tails*.

vectorial nature of the electric field and the symmetry of the bilayer systems with respect to the central plane. Thus, field vectors pointing outwards from the bilayer towards the water phase are indicated by positive values of $E(z)$ on the right hand side of the diagram, and by corresponding negative values, of equal magnitude and equidistant from the origin, on the left hand side (and vice versa for inwards pointing vectors). In other words, the field profiles would be symmetric if calculated with respect to the normal for each leaflet. It can be seen that the electric field magnitude reaches huge peak values, with overall maxima of up to $\sim 7.5 \times 10^8$ V/m, located near

or inside the lipid heads region depending on the system. Despite the absence of direct experimental measurements for comparison, such strong electric fields are consistent with the dipole potential profile, in relation to its peak magnitudes and steep gradients [70]. In fact, the electric field strength corresponds to the spatial derivative of the dipole potential, which varies substantially over extremely small distances (see Figure 3.7). For pure DOPC, our result matches as expected a previously reported profile [370] obtained from simulations of the same force field (CHARMM36). For the mixed systems, we are not aware of any previously reported $E(z)$ data from either simulation or experiment.

It is clear from Figure 3.9 that changes in the DOPC/DOPE ratio induce substantial redistributions of the electric field, especially corresponding to the lipid heads region and at the heads-tails interface. Regarding the pure DOPC bilayer, the largest peak magnitude corresponds to $\sim 7.5 \times 10^8$ V/m, and is located at the interface between the heads and tails regions as denoted on Figure 3.9. Considering the DOPC/DOPE (3/1) systems, the magnitude drops by $\sim 0.8 \times 10^8$ V/m, or 11%. An even larger decrease of $\sim 1.1 \times 10^8$ V/m in the field strength can be observed by comparing the DOPC/DOPE (3/1) and DOPC/DOPE (1/1) bilayers. The magnitude of the heads-tails interfacial peak decreases further until a value of $\sim 4.4 \times 10^8$ V/m for the pure DOPE bilayer, corresponding to an overall drop of 41% compared to the pure DOPC system. Interestingly, the two systems with highest DOPE content (DOPC/DOPE (1/3) and pure DOPE) are also characterized by additional features; in particular, their points of maximum field strength correspond to extra peaks (compared to the other systems) inside the heads region. In fact, taking into account all the peaks of maximum magnitude for each of the five systems, from pure DOPC to pure DOPE, such peaks can also be interpreted as shifting outwards from the bilayer interior towards the water region, by as much as 0.6 nm when comparing the pure DOPC and DOPE bilayers. The largest composition-dependent effect on the field magnitude can be observed at a distance of $\sim$2.3 nm from the bilayer center, where the field strength is almost zero for DOPC, while it grows dramatically for the mixed bilayers, up to $\sim 7 \times 10^8$ V/m for DOPE. Overall, such $E(z)$ changes are expected to have significant effects on any charged or polar molecule interacting with the bilayer (e.g., permeants), as well as embedded peptides and proteins. Specifically, it was estimated that a change in field magnitude

of $\sim 2 \times 10^8$ V/m can already induce substantial shifts in protein conformational equilibria [370]. Charged protein residues are predicted to be especially sensitive, but also uncharged residues will be affected through interactions with the large dipole (3.5 D) that characterizes the peptide bond.

In the hydrocarbon tails core, the composition-dependent changes in $E(z)$ are more limited, as intuitively expected considering that there are no chemical differences between DOPC and DOPE tails. However, some effects can still be noted. In particular, the innermost peaks, located at $\sim$0.4 nm from the bilayer center, show increasing magnitudes with addition of DOPE, up to 0.5×10^8 V/m when comparing pure DOPC with pure DOPE. Regarding the peaks at $\sim$1 nm from the bilayer center, a slight increase (up to 0.25×10^8 V/m) in magnitude is accompanied by a small shift outwards (up to $\sim$0.1 nm) upon DOPE addition.

To further assess the biological relevance of the results obtained, it is useful to compare them to the electric fields corresponding to two other membrane-related potentials, i.e., the transmembrane potential and the surface potential, for which more knowledge exists compared to the dipole potential, because they are comparatively easier to study experimentally [70]. The transmembrane potential arises from the different ion concentrations typically present between the inner and outer sides of biological membranes, and underlies the opening and closing of ion channels that control the transmission of electrical signals along neurons and muscle cells. The surface potential arises from charged lipid headgroups and polar molecules accumulating at the membrane surface, and controls the ion distribution at the cell surface. The electric field magnitudes related to the transmembrane and surface potentials have been estimated to be, respectively, $\sim 0.25 \times 10^8$ V/m and $\sim 0.1 \times 10^8$ V/m[323]. Considering that these field strengths are known to be responsible for significant biological activity, the composition-dependent effects for the dipole potential highlighted here, especially around the heads region, can be expected to also have major biological consequences. In fact, even the smaller DOPC/DOPE composition-dependent effects on $E(z)$ that we observed in the tails region are of comparable size to the field magnitudes from the transmembrane and surface potentials.

To further analyse the electric field, we also calculated the separate contributions from the water and lipid molecules, respectively (Figure 3.10). By comparing

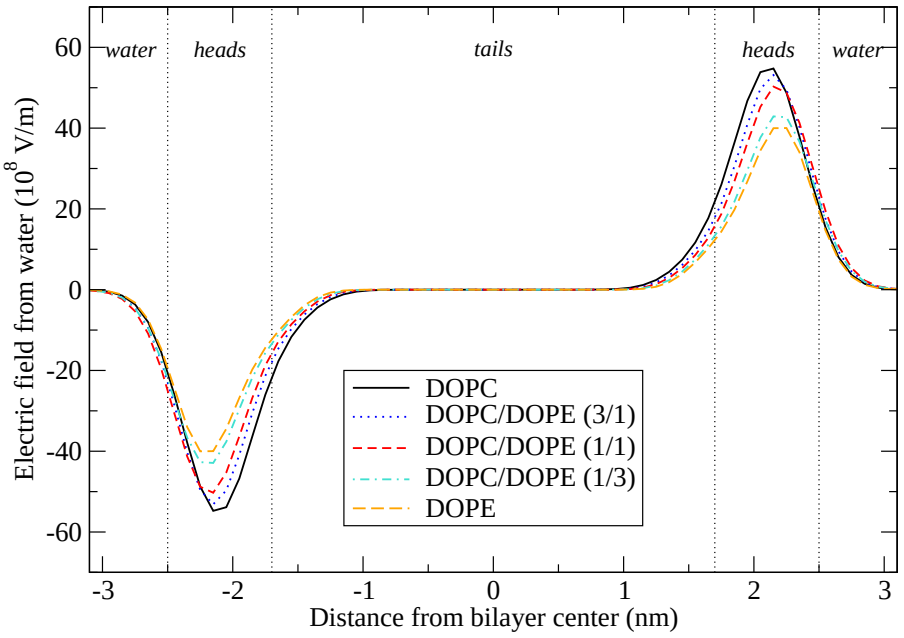

(a)

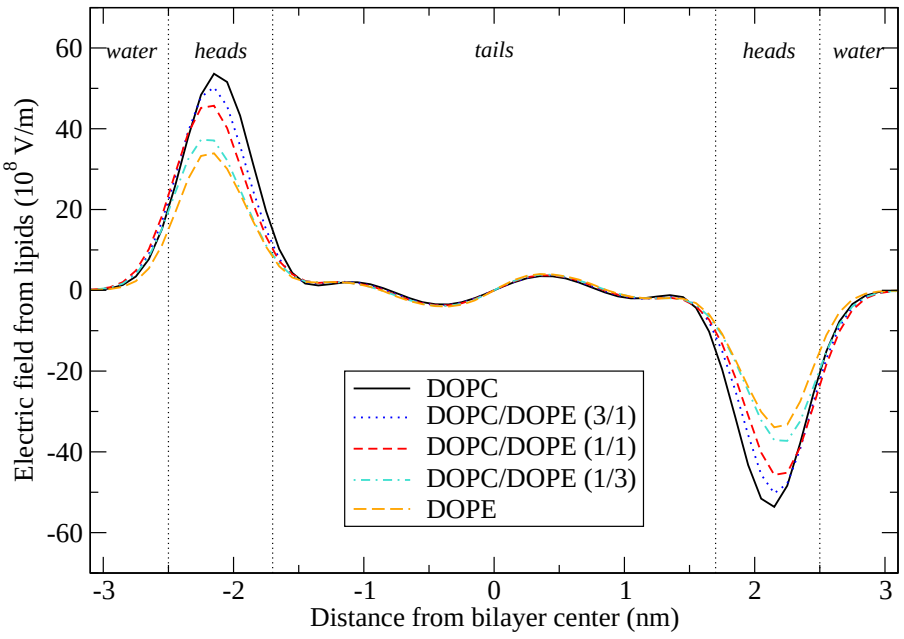

(b)

Figure 3.10: Separated contributions of the electric field: (a) from water and (b) from lipid molecules. Vertical dotted lines indicate approximate boundaries between regions occupied predominantly by *water*, lipid *heads*, and hydrocarbon tails.

Figures 3.10a and 3.10b, it can be noticed in general that the water and lipid profiles display extremely large and mostly opposing field strengths, whose main peaks are all centered inside the lipid heads region. The water contribution shows a negative peak on the left hand side of the profile, and an antisymmetric positive peak on the right hand side. These peaks originate from a preferential orientation of the water molecular dipoles, whereby the positive ends (H atoms) tend to point towards the bilayer center, while the negative ends (O atoms) tend to point away from the membrane and towards the bulk water phase. The water electric field is countered by that originating in the lipid molecules; specifically, the lipid headgroup dipoles preferentially point away from the membrane and towards the outer water phase. Inside the hydrocarbon tails region, from -1 to 1 nm about the bilayer center, the water contribution is zero, due to the absence of water in the hydrocarbon core. The lipid profile exhibits instead shallow peaks (evidently much smaller in magnitude than those in the heads region), arising from the preferential orientation of dipolar molecular segments along the hydrocarbon tails. In terms of the influence of changes in the lamellar/nonlamellar lipid composition, the presence of increasing amounts of DOPE induces increasing attenuations of the magnitude of the peak strength in the heads region, for both the water (Figure 3.10a) and lipids (Figure 3.10b) profiles. By comparing the individual profiles with the total $E(z)$ curve (Figure 3.9), it is clear that the net electric field originates from a nontrivial interplay between the separate contributions from the lipid and water molecules, with large cancellations of enormous opposing field strengths. In fact, the $E(z)$ range for the individual contributions is -60×10^8 V/m to 60×10^8 V/m, which is an order of magnitude larger than the range of values observed for the net profiles.

3.3.5 DOPE inverse phase formation

We performed an additional simulation to validate the nonlamellar phase behavior of DOPE modeled with the CHARMM36 lipid force field which was employed for this study. Starting from the last configuration of the 1-μs pure DOPE bilayer run, the system was first heated up to 1000 K until the bilayer was completely disrupted by thermal agitation, and a random dispersion of lipids and water was obtained. The temperature was subsequently brought back to 303 K, and the system

spontaneously self-assembled into an inverse hexagonal phase. Figure 3.11 shows a series of trajectory snapshots depicting the main stages of the phase formation process. In the last snapshot, it is possible to identify the circular cross sections of cylindrical water columns, which are typical of the DOPE inverse phase. The DOPE heads line the water columns, while the lipid tails assemble together away from direct contact with water. Overall, our results indicate that the CHARMM36 lipid force field is able to capture correctly the experimentally observed nonlamellar phase of DOPE during self-assembly from a random dispersion. However, small preassembled bilayers (such as the one reported in the main body of this paper) under periodic boundary conditions remain stable in the lamellar phase. It may be possible to observe a lamellar to inverse hexagonal phase transformation by simulating larger (multilamellar) systems, however this may require prohibitively large computing resources (in fact, such a phase transformation has so far only been simulated with coarse-grained models [251]).

3.4 Conclusions

In this chapter, we presented a computational investigation into how a number of physical properties of lipid bilayer membranes are affected by changes in the lipid composition. Specifically, we conducted atomistic molecular dynamics simulations of bilayer systems containing the lamellar lipid DOPC and the nonlamellar lipid DOPE in varying proportions. We investigated basic structural properties, as well as depth-dependent distributions of internal pressure, dipole potential, and electric field.

For most of the properties studied, we observed changes proportionally related to the changes in the lipid composition, as intuitively expected. However, the actual amount of change in the physical properties was shown to depend dramatically on the specific properties under investigation. In particular, while structural properties varied only marginally across the different systems, substantial composition-dependent changes were observed for the lateral pressure, dipole potential, and electric field profiles. Increasing the concentration of DOPE was shown to induce a transfer of pressure from the lipid headgroups to the inner hydrocarbon core. Specifically, we observed a decrease in integrated contributions by up to 50% in the headgroup region

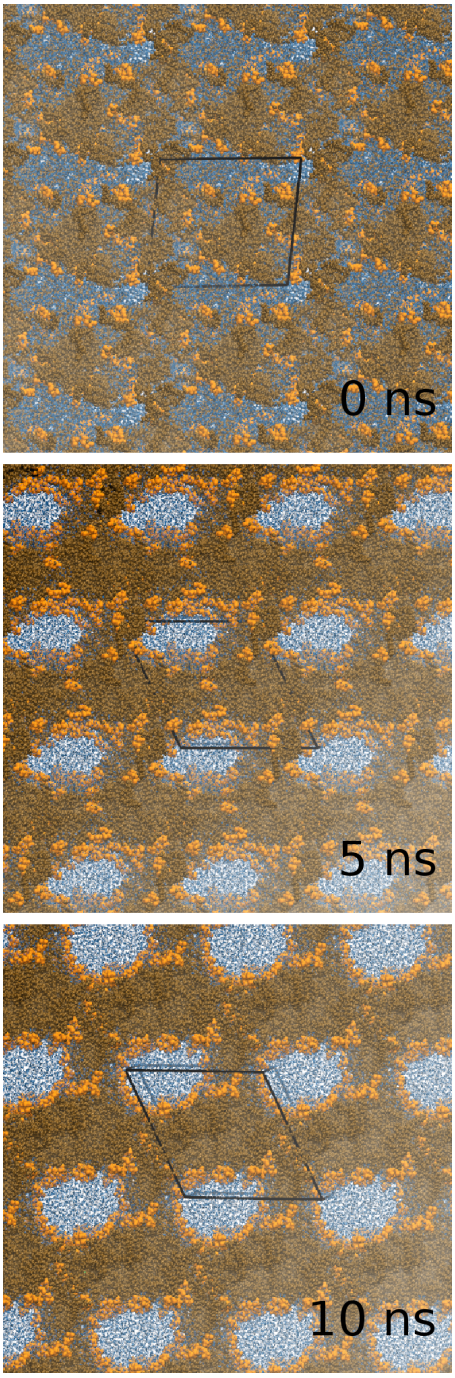

Figure 3.11: Simulation snapshots of spontaneous formation of DOPE inverse hexagonal phase. Lipid heads and tails are colored orange and brown, respectively, while water is blue. The central simulation region is identified by black segments.

and an increase by up to 400% in the hydrocarbon tail region, when comparing pure DOPC and DOPE systems. The dipole potential profile across the whole membrane was enhanced by the addition of DOPE, with increases of over 20% for the pure DOPE system compared to pure DOPC. Regarding the electric field, composition changes brought about nontrivial effects in a number of features, including a shift of the main peaks by 0.6 nm towards the outside of the bilayer, as well as a drop of 41% in strength at the heads-tails interface.

In summary, we have shown quantitatively that changes in the lamellar vs. nonlamellar lipid composition amplify mechanical and electrical signals without significantly altering structural features. The predicted effects on lateral pressure, dipole potential, and electric field profiles are expected to be large enough to affect a range of biological phenomena, including membrane permeation and binding, as well as conformational changes within membrane proteins.

Chapter 4

Effects of High Pressure on Bilayer Membranes with Different Saturation Levels

The response of lipid membranes to changes in external pressure is important for many biological processes, and it can also be exploited for technological applications. In this chapter, we employ all-atom molecular dynamics simulations to characterize the changes in the physical properties of phospholipid bilayers brought about by high pressure (1000 bar). In particular, we study how the response differs, in relation to different chain unsaturation levels, by comparing mono-unsaturated 1-palmitoyl-2-oleoyl-phosphatidylcholine (POPC) and bi-unsaturated dioleoyl-phosphatidylcholine (DOPC) bilayers. Various structural, mechanical and dynamical features are found to be altered by the pressure increase in both bilayers. Notably, for most properties, including bilayer area and thickness, lipid order parameters, lateral pressure profile, and curvature frustration energy, we observe significantly more pronounced effects for mono-unsaturated POPC than bi-unsaturated DOPC. Possible biological implications of the results obtained are discussed, especially in relation to how different lipids can control the structure and function of membrane proteins.

4.1 Introduction

Pressure is one of the most important environmental factors for living organisms; growing attention is being devoted especially to the effects of high pressure on biological processes. On the one hand, experimental studies have revealed how various organisms and tissues undergo cell damage under high pressure [111, 300, 381]. On the other hand, some bacteria and viruses have been shown to be pressure-tolerant [8, 114]. Barophilic organisms have been discovered in deep marine environments where the hydrostatic pressure can reach 1100 bar (110 MPa), a factor of over one thousand greater than atmospheric pressure [271]; in general, it is of great scientific interest to understand how life can adapt to such extreme environmental pressures [325]. To study the biological impact of high pressure, researchers have investigated a range of phenomena related to pressure change, such as the inactivation of pathogens [147] or the denaturation of proteins [376]. High hydrostatic pressure is also relevant to the action mechanism of anesthetics [62], and it can be exploited for protein crystallization [67] as well as for drug encapsulation and delivery [176, 284]. Moreover, the food industry has seen in recent years the emergence of pressure-based processing technologies, for example as an approach to improve pasteurization. Compared to traditional high-temperature treatments, high-pressure food processing is expected to better preserve the original organoleptic properties such as flavor and color, as well as the nutritional content [175, 236].

The lipid bilayer membrane, a key structural and functional component of cells, is regarded as one of the most pressure-sensitive biological systems [301]. Various aspects of the lipid bilayer have been observed to be altered under high pressure conditions, such as volume, fluidity, and phase transition [42, 43, 72, 329, 377]. Moreover, the folding/unfolding and aggregation processes of membrane-embedded proteins, who closely interact with membrane lipids, can also be affected by pressure changes [181, 339]. Overall, pressure effects on lipid membranes appear to be of great importance for living organisms. As a remarkable example, many bacteria have been found to modify their membrane lipid composition in response to environmental changes in hydrostatic pressure [229]. In particular, evidence collected over the past decades on deep sea organisms suggests that the increased deep sea hydrostatic pressure selects for a higher ratio of unsaturated fatty acids in the

lipid membrane [23, 84, 164, 278]. Unsaturated fatty acyl chains in membrane phospholipids are characterized by one or more double bonds, which induce more disordered conformations, ultimately maintaining membrane fluidity (an essential condition for most biological functions) even under high pressure. In particular, it has been shown experimentally that a bi-unsaturated 16:0-18:2 PC (PLPC) bilayer shows greater resistance to pressure-induced liquid-to-gel phase transition than a mono-unsaturated 16:0-18:1 PC (POPC) bilayer [329].

While previous experimental work has shed light on pressure-induced structural and energetic changes in relation to the unsaturation level in lipid membranes, molecular-level mechanisms are still not well understood. In practice, measuring microscopic membrane properties while simultaneously maintaining the pressure at a desired level is fraught with great technical challenges [43].

As an alternative to conventional experiments, molecular simulation represents a powerful tool to study pressure effects on lipid membrane systems, thanks to the ability to accurately control the simulated pressure while obtaining quantitative nanoscale measurements [346, 351, 387]. In this work, we conduct atomistic molecular dynamics simulations to study the effects of high pressure on key physical properties of lipid bilayers. In particular, we focus on two lipid types that are prevalent in biological membranes, i.e., dioleoyl-phosphatidylcholine (DOPC) and 1-palmitoyl-2-oleoyl-phosphatidylcholine (POPC). These two lipids are very similar apart from a key difference in unsaturation content, so that their response to pressure changes will also allow us to investigate the specific role of unsaturation in determining related changes in physical properties. Specifically, DOPC has two unsaturated chains each containing a C-C double bond, whereas POPC has one such mono-unsaturated chain (as DOPC) while the other chain is fully saturated (all C-C linkages are single bonds). By comparing the changes induced by increasing the pressure on bilayers comprising these two representative lipid types, we aim to provide a systematic understanding of the role that unsaturation plays in the membrane response to increased pressures. In particular, we simulate the two bilayer systems at the standard atmospheric condition of 1 bar and at the higher pressure level of 1000 bar, under which both the DOPC and POPC bilayers still remain in the fluid L_α phase (which is the biologically relevant phase). At each of these two pressures, a series of structural, dynamical, mechanical, and electrostatic properties are measured

and compared. While research on lipid bilayers at standard atmospheric condition has been extensive, to our knowledge this is the first simulation study investigating high pressure effects on bilayer properties using fully atomistic models. The few previous simulations of lipid bilayers at high pressure were conducted with either united-atom or coarse-grained models [64, 185]. In this work, we simulate all-atom models to investigate fundamental bilayer properties including lipid area, lipid volume, bilayer thickness, lipid lateral diffusivity, and deuterium order parameters. Notably, we also calculate the lateral pressure and dipole potential, two elusive and often overlooked trans-membrane profiles which have been suggested to play key roles in numerous membrane phenomena [227, 319, 368]. The lateral pressure (or stress) profile represents the distribution of lateral stresses as a function of depth inside the bilayer. Experimentally, given the nanoscopic thickness of a typical lipid bilayer membrane, it is extremely difficult to measure internal stresses. Attempted measurements suggest significant depth-dependent variation [166, 343], and computational modeling studies have indeed quantified lateral pressure changes on the order of several hundred bars [240]. Naturally, substantial mechanical influence on embedded molecules such as membrane proteins or permeants is expected as a consequence of the existence of the lateral pressure profile [208, 245, 247, 354]. Moreover, the lateral pressure profile underpins a number of elastic parameters, such as the spontaneous curvature and the bending rigidity, which are critical indicators of the mesoscopic phase behavior of a hydrated lipid bilayer [43, 208, 377]. For example, changes in the lateral pressure profile and related elastic properties may lead to the destabilization of cell membranes [36, 123, 256]. The dipole (electrostatic) potential profile, arising from the preferential alignment of the dipole moments of water molecules and dipolar segments of lipid molecules, is another trans-membrane property that is of great biological relevance yet also very difficult to probe by experiment [96, 368]. In this chapter, we investigate the sensitivity of DOPC and POPC bilayers to external pressure by evaluating the dipole potential profile as a function of depth across the bilayers.

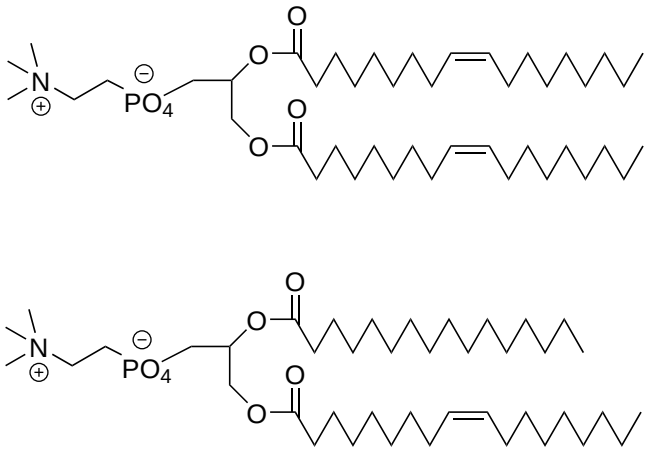

Figure 4.1: Molecular structures of DOPC (above) and POPC (below).

4.2 Methods

4.2.1 Lipid bilayers

Two single-type lipid bilayer systems have been investigated. One system comprises 1-palmitoyl-2-oleoyl-phosphatidylcholine (POPC) lipids, which are mono-unsaturated. The other system comprises dioleoyl-phosphatidylcholine (DOPC) lipids, which are bi-unsaturated. The molecular structures of the two lipid types are shown in Figure 4.1. Each bilayer system contains 128 lipid molecules and is fully hydrated with 4300 water molecules (with a water/lipid ratio of approximately 33.6) [172, 388]. Initial pre-equilibrated configurations were obtained from our previous studies [92].

4.2.2 Simulation details

The bilayer systems were modelled with the CHARMM36 all-atom force field [172] and simulated with the Gromacs 5.1 software [30]. Long range electrostatic interactions were solved by the PME (Particle-Mesh Ewald) method [74]. Bonds and angles in water molecules were constrained by the SETTLE algorithm [222]; the LINCS algorithm [139] was used to constrain all other hydrogen-related bonds, with a numerical expansion up to fourth order and two iterations in every step for correcting rotational effects. With these constrained algorithms applied, the systems' total energy was well conserved at the selected timestep of 2 fs. Each of

the DOPC and POPC bilayers were simulated at two pressure levels, 1 bar and 1000 bar, respectively. The Parrinello–Rahman barostat method was used [263], with the pressure coupled semi-isotropically (isotropic in the two directions along the bilayer plane but independent to the one in the normal direction) and a coupling time constant of 1 ps. The temperature was maintained at 310 K for all systems, by applying the velocity-rescale thermostat [46] with a damping time constant of 0.1 ps. Each simulation was run for 1000 ns in total. The first 200 ns were regarded as equilibration and the following 800 ns were used for data analysis. Data for all properties were sampled every 50 ps.

4.2.3 Data analysis

The following properties were evaluated: area per lipid (A_L), volume per lipid (V_L), bilayer thickness (d_{HH}), lateral diffusion coefficient (D_L), deuterium order parameter (S_{CD}), electron density profile ($\rho(z)$), dipole potential profile ($\Psi(z)$), lateral pressure profile ($\Pi(z)$), monolayer spontaneous curvature (c_0^m), monolayer bending modulus (κ^m), curvature frustration energy ($\kappa^m c_0^m$). Calculations of these properties were carried out following standard approaches, as detailed previously [157, 251]. To estimate the average volume per lipid V_L, two extra simulations consisting of 4300 TIP3P water molecules (same amount as in the bilayer systems) in the bulk liquid phase were performed at 1 bar and 1000 bar, respectively, so that V_L could be computed as $V_L = (V_{total} - V_{water})/128$, where V_{total} is the total volume of the bilayer systems and V_{water} is the volume of the bulk water simulations. Regarding the lateral pressure profile, a modified version of Gromacs, the Gromacs-LS package [349, 357], was used to rerun the simulation trajectories and to output local stress tensors. Since the long-range electrostatic solver is not implemented in the Gromacs-LS package, an increased cut-off distance of 2.2 nm was used for the Coulomb interactions, as recommended by the package developers [357].

Regarding the statistical analysis, uncertainties for all calculated properties (except for D_L) were estimated by the block averaging procedure [109, 292], with a block size of 40 ns. The only exception, D_L, was obtained from the linear fitted slope of the averaged 2-dimensional mean squared displacement (MSD) following a standard procedure [91, 243]. The MSD was treated by the time-averaged method,

with the initial reference point reset every 40 ns [157, 292]. All numerical results will be presented in the format "mean ± standard error (S.E.)" unless otherwise specified.

To rigorously compare the results obtained for the two different lipid types at the two levels of external pressure studied, we carried out standard two-sample t-tests wherever appropriate; a difference between two means is considered statistically significant if the corresponding p value is less than 0.05, as per predominant convention.

4.3 Results and discussions

4.3.1 Structural properties

The area per lipid (A_L), volume per lipid (V_L), and bilayer thickness (d_{HH}) were calculated for the DOPC and POPC bilayer simulations at the two investigated pressures. Results are summarized in Table 4.1. Regarding the values obtained at

Table 4.1: Structural properties for the simulated bilayer systems

	A_L (Å^2)	V_L (Å^3)	d_{HH} (Å)
DOPC, 1 bar	68.72 ± 0.09	1290.46 ± 0.09	38.42 ± 0.05
DOPC, 1000 bar	65.43 ± 0.12	1235.91 ± 0.06	38.28 ± 0.06
POPC, 1 bar	65.10 ± 0.09	1243.04 ± 0.26	38.74 ± 0.03
POPC, 1000 bar	60.80 ± 0.13	1188.18 ± 0.55	39.14 ± 0.07

A t-test was performed for each pair of values from the same bilayer between the two pressures. Statistically significant differences ($p < 0.05$) exist for each pair, with the only exception of d_{HH} for the DOPC bilayer ($p = 0.13$).

atmospheric pressure, our results are consistent with previous reports from both experiments and atomistic simulations. [92, 172, 180, 232, 273] A comparison with the results obtained at the high pressure of 1000 bar reveals noticeable effects. In particular, for the area per lipid A_L, a significant reduction is shown for both POPC and DOPC as the pressure increases from 1 bar to 1000 bar. Comparing the extent to which A_L changes, the reduction for POPC (an average 4.30 Å^2 or 7.4% decrease) is larger than that observed for DOPC (an average 3.29 Å^2 or 4.7% decrease). Regarding the lipid volume, increasing the pressure causes a reduction

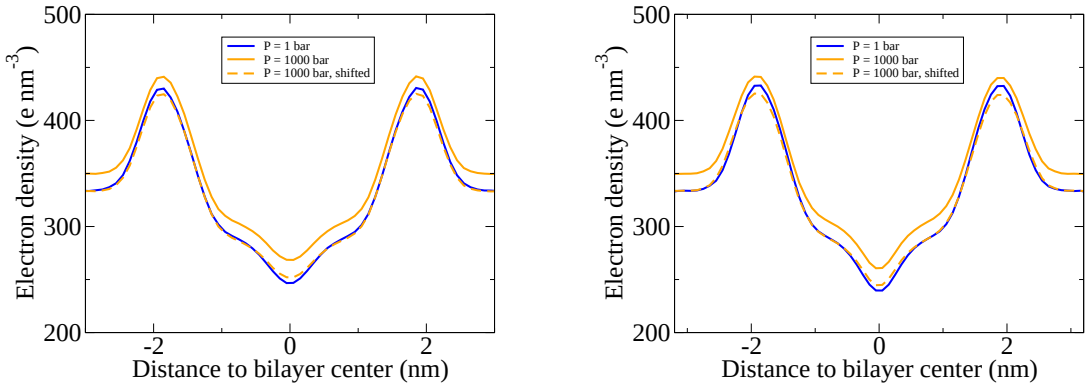

Figure 4.2: Electron density for (a) DOPC and (b) POPC bilayers at 1 bar (blue) and 1000 bar (orange). To better highlight differences within each membrane type (see main text), the dashed orange lines represent electron density profiles at 1000 bar that have been shifted to overlap those at 1 bar in the water phase. Error bars are smaller than the thickness of the lines.

of V_L for both lipid types, as intuitively expected, with an average 54.5 Å^3 (4.2%) decrease being shown for DOPC and 54.9 Å^3 (4.4%) for POPC. Regarding the bilayer thickness (d_{HH}), the pressure increase does not induce a significant effect on DOPC. However, it is possible to identify a statistically significant increase for POPC, albeit small (0.4 Å or 1%). While the change seems negligible, previous findings indicate that membrane protein channels can be deformed and inactivated by hydrophobic mismatch even for small changes in bilayer thickness of less than 1 Å [214]. Previous studies on the relation between bilayer thickness and pressure have given varying results by different techniques and measurements: a recent experimental work observed that the lattice parameter of DOPC vesicle increased along with the pressure increase [284], while insensitivity of d_{HH} was found for DPPC bilayers in the fluid phase at different pressures in a coarse-grained simulation study [185].

Electron density profiles ($\rho(z)$) for both bilayers are shown in Figure 4.2. It can be seen that $\rho(z)$ for both DOPC and POPC increases across the whole depth z as the pressure is increased from 1 bar to 1000 bar, consistently with the reduction in

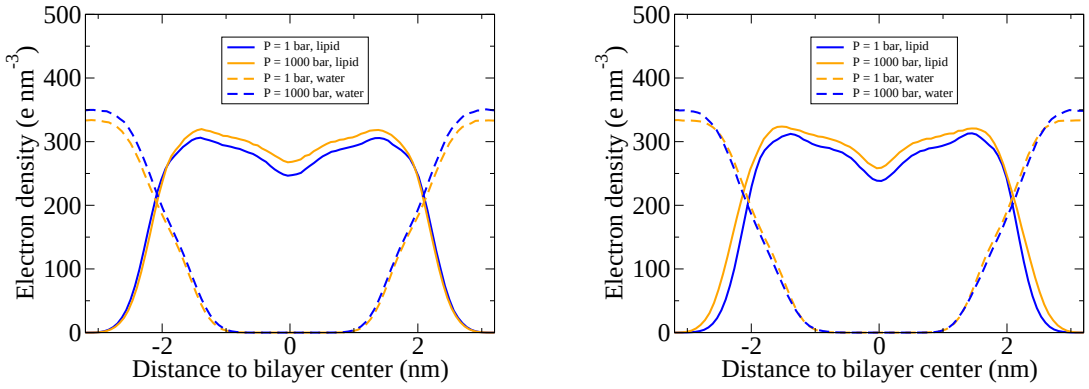

Figure 4.3: Electron density of the individual water and lipid components for (a) DOPC and (b) POPC bilayers at 1 bar (blue) and 1000 bar (orange).

lipid area and volume reported earlier. To better highlight differences within each membrane type, the electron density profiles at 1000 bar have also been shifted so that they overlap those at 1 bar in the water phase; such shifted curves can be seen in Figure 4.2 as dashed orange lines. Compared to the 1 bar curves, it can be seen that the 1000 bar shifted profiles are slightly lower at the two peaks corresponding to the lipid head groups while higher at the central trough. These differences indicate that most of the volume reduction takes place in the bilayer center (the lipid tail end region). This can be interpreted as a relatively higher resistance to volume reduction in the lipid head groups, since this region is already the densest; conversely, the bilayer is compressed more markedly in the central core, where the density is lowest (thus corresponding to highest free volume). It is relevant to note that, despite the compression brought about by the pressure increase, no chain interdigitation is observed in any of the systems studied, as indicated by the well-defined central minima in all the electron density diagrams of Figure 4.2. Further confirmation of the absence of interdigitation can be found in the Supporting Information, where we report individual electron density profiles for only the chain components (Figure 4.3)

4.3.2 Deuterium order parameters

Deuterium order parameters (S_{CD}) for acyl-chain carbon atoms computed from each investigated system are displayed in Figure 4.4 based on:

$$S_{CD} = \frac{1}{2}\langle 3\cos^2\theta - 1\rangle, \tag{4.1}$$

where θ is the angle between the C-D vector and axis normal to bilayer surface. The angular brackets represent an ensemble average. The S_{CD} values for both chains in DOPC lipids (Figure 4.4a and 4.4c) and the *sn*-2 chain in POPC lipids (Figure 4.4d) exhibit generally similar features, in that the S_{CD} value drops to a minimum at positions corresponding to the double-bonded atoms. In contrast, the POPC *sn*-1 chain (Figure 4.4b) exhibits a monotonically decreasing S_{CD} from the position corresponding to the glycerol segment to the end of the chain, as is normal for a fully-saturated chain.

As intuitively expected, higher pressure causes the S_{CD} values to increase, reflecting enhanced order brought about by a reduction in free volume (consistently with the results on the lipid volume reported earlier). Specifically, the increase in order parameters indicates a change in orientation of the corresponding chain segments, which tend to become more aligned to the direction perpendicular to the bilayer plane. By comparing *sn*-2 (unsaturated) tails in DOPC and POPC (Figure 4.4c and Figure 4.4d), different changes induced by the pressure increase can be noticed. The effect on POPC is more pronounced, with an average S_{CD} increase of 0.015 compared with 0.006 for its DOPC counterpart. Although not directly comparable, S_{CD} values for the POPC sn-1 chain are increased markedly by 0.020, while the increase for DOPC sn-1 chain is 0.007. Experimental studies have suggested that S_{CD} values for POPC in the L_α phase increase by roughly 10^{-4} per MPa (10 bar) [44] at 300 K, corresponding to 0.01 over 1000 bar, which is in reasonable agreement with our results.

Overall, our comparison between S_{CD} order parameters in DOPC and POPC shows that the less saturated POPC bilayer is more sensitive to the pressure increase, consistently with our earlier observation on lipid area, lipid volume, and bilayer thickness.

In general, the changes in structural properties from our simulations are con-

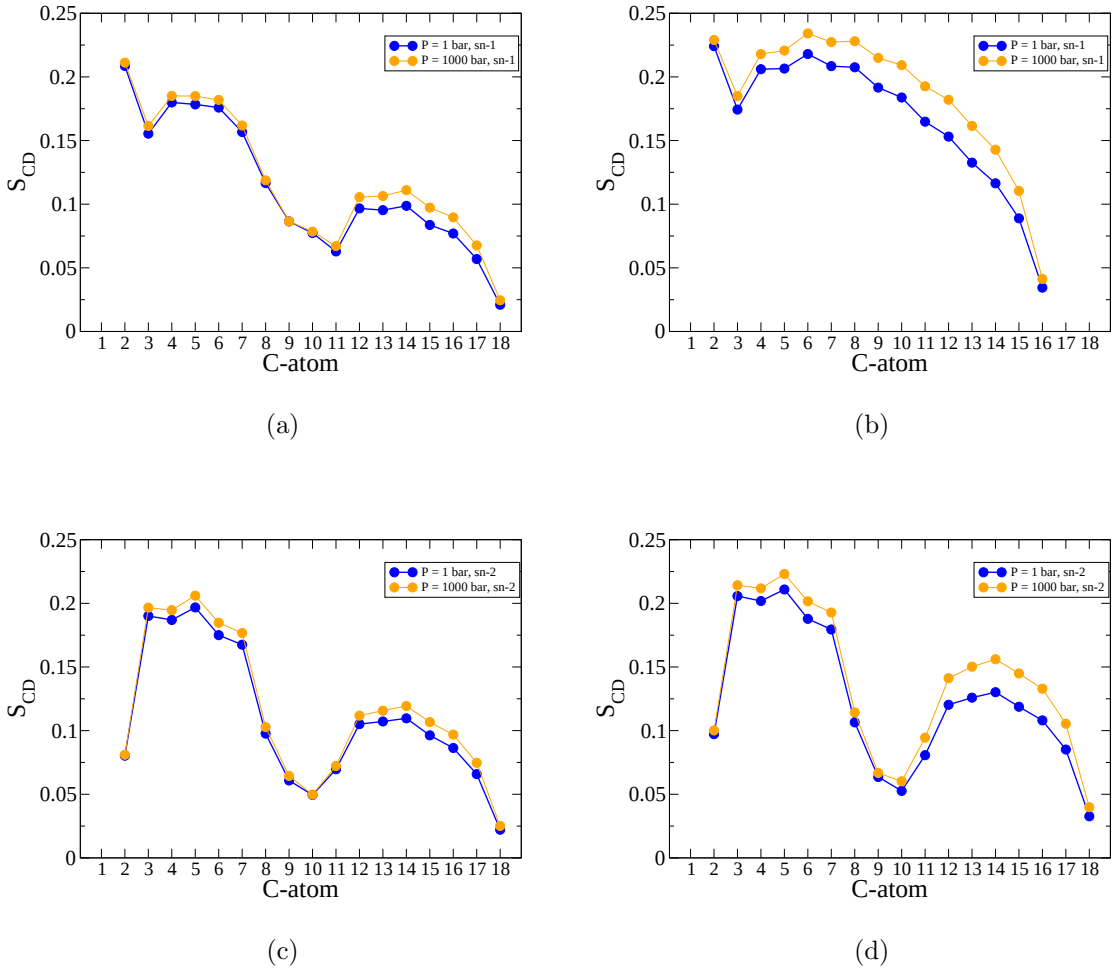

Figure 4.4: S_{CD} for (a) DOPC, *sn*-1 chain, (b) POPC, *sn*-1 chain, (c) DOPC, *sn*-2 chain, and (d) POPC, *sn*-2 chain at 1 bar (blue) and 1000 bar (orange). Error bars are smaller than the symbols' size.

sistent with previous theoretical understanding that increased unsaturation (as in DOPC vs. POPC) results in a stronger resistance to structural change under high pressure [329].

4.3.3 Lateral diffusion

The lateral diffusion coefficient (D_L) measures the long range motion of lipids in the bilayer plane. The D_L values obtained from our DOPC and POPC simulations at 1 bar are 14.7 ± 0.8 $nm^2/\mu s$ and 16.2 ± 0.6 $nm^2/\mu s$, respectively. These results are in reasonable agreement with previously reported values for phospholipid bilayers from both experiments and simulations [106, 112, 251, 273]. Comparing the two lipid types, we find no statistically significant difference between D_L for DOPC and POPC at 1 bar ($p = 0.18$); this is in agreement with the earlier conclusion by Ollila et al. [241] that unsaturation does not influence the lateral diffusivity of lipids. Under the high pressure of 1000 bar, we obtain D_L values of 9.8 ± 1.5 $nm^2/\mu s$ and 7.1 ± 0.2 $nm^2/\mu s$ for DOPC and POPC, respectively. It is clear that, for both lipid types, there is a substantial reduction in lateral diffusion brought about by the pressure increase; this effect is expected intuitively, and is consistent with the observed reduction in system volume. Comparing the D_L values for the two lipid types at 1000 bar, no statistically significant difference is detected ($p = 0.053$), similarly to what was found for the systems at 1 bar. In summary, while high pressure markedly reduces the lateral diffusivity for both the DOPC and POPC bilayers, our results do not show specificity to the lipid type.

4.3.4 Lateral pressure profile

The lateral pressure profile ($\Pi(z)$) characterizes the inhomogeneous and depth-dependent distribution of lateral stresses across the bilayer. The calculation of $\Pi(z)$ from molecular simulations provides nanoscale insights for the understanding of the mechanical stability of the membrane itself as well as the interactions between lipids and other biomembrane constituents (such as membrane proteins). The $\Pi(z)$ profiles computed for the systems investigated in this work are shown in Figure 4.5. Regarding the profiles at 1 bar, both the DOPC and POPC results are consistent with previous literature [239, 240, 249]. In particular, large positive peaks

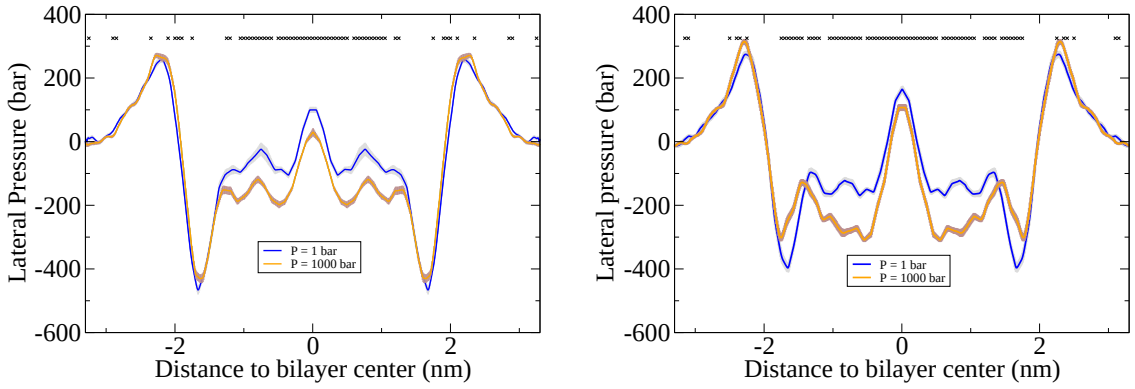

(a) (b)

Figure 4.5: $\Pi(z)$ for (a) DOPC and (b) POPC bilayers at 1 bar (blue) and 1000 bar (orange). Shaded areas indicate the statistical uncertainty (mean $\pm$ S.E.). Statistical analysis was performed to compare the difference between the two curves in each diagram. The stars at the top of each diagram indicate the positions where the values of the two curves are statistically different ($p < 0.05$).

of $\sim$ 300 bar can be seen at a distance of $\sim$ 2 nm to the bilayer center, reflecting net repulsive forces primarily attributable to steric and electrostatic interactions between lipid heads and water. Proceeding deeper inside the bilayers, at a depth corresponding roughly to the glycerol groups, we can observe sharp negative troughs, which are typically explained in terms of attractive forces due to the hydrophobic effect. [58, 208] The bilayer center is instead characterized by pressure peaks that are believed to originate from loss of entropy in the chain region. [230, 253]

Regarding the effect of increased external pressure, in the outer regions corresponding to the water phase and headgroup layer no significant differences are observed for both lipid types. Such a low sensitivity of $\Pi(z)$ to external pressure changes in these regions has been predicted theoretically on the basis of the relatively high local density [43] (which can be seen in the electron density profiles of Figure 4.2). Deeper inside the bilayer, the large hydrophobic troughs exhibit a response to high pressure which is dependent on the lipid type. In particular, increased external pressure does not significantly alter the DOPC hydrophobic troughs, whereas the POPC troughs markedly decrease in magnitude, by $\sim$ 100 bar. Regarding

the lipid chain region, it can be seen that the increase in external pressure brings about a significant and substantial decrease in $\Pi(z)$ for both lipid types. This effect can be correlated to the increase in chain order parameters under high pressure observed earlier (Figure 4.4). Such a relation was also found in previous studies focusing on other external factors like temperature and chain length [115, 241]. From our data, it can be seen that the pressure-induced changes are more prominent for POPC, consistently with the larger increase in S_{CD} values with respect to DOPC (as discussed earlier). In particular, taking the chain region to be within 1.3 nm from the bilayer center, we observe an average lateral pressure drop of 82.8 ± 19.2 bar for DOPC under high pressure, while for POPC we calculate a larger drop of 101.7 ± 35.9 bar.

Overall, it is evident that the lateral pressure profile for both DOPC and POPC bilayers is affected by the external pressure, and that the effects are more pronounced for the mono-unsaturated POPC compared to the bi-unsaturated DOPC. Higher lipid unsaturation therefore reduces bilayer sensitivity to increased hydrostatic pressure; this is analogous to the behavior observed previously for a number of structural properties. Further quantitative analysis of the lateral pressure profiles, based on elastic parameters that can be derived via numerical integration, is reported in the following section.

4.3.5 Elastic properties

Key elastic parameters of the bilayer are connected analytically with $\Pi(z)$. Specifically, the product of the monolayer bending modulus κ^m and the monolayer spontaneous curvature c_0^m is equal to the fist integral moment of $\Pi(z)$:

$$\kappa^m c_0^m = \int_0^l z\Pi(z)\,\mathrm{d}z, \tag{4.2}$$

where $z = 0$ at the center of the bilayer and $z = l$ in the water phase. [24, 340] To obtain the fist integral moment of $\Pi(z)$ (corresponding to the right hand side of equation 4.2), a conventional numerical integration was performed. The monolayer bending modulus κ^m was estimated by the relation $\kappa^m = k_A(d_{HH} - 10)^2/48$ based on an empirical model [293]. The monolayer spontaneous curvature c_0^m can then

Table 4.2: Elastic properties for the simulated bilayer systems

	κ^m $(10^{-20}J)$	c_0^m (nm^{-1})	$\kappa^m c_0^m$ $(10^{-21}J\,nm^{-1})$
DOPC, 1 bar	4.43 ± 0.03	-0.056 ± 0.023	-2.48 ± 1.10
DOPC, 1000 bar	3.92 ± 0.03	-0.091 ± 0.034	-3.55 ± 1.44
POPC, 1 bar	4.34 ± 0.02	-0.054 ± 0.027	-2.32 ± 1.25
POPC, 1000 bar	3.88 ± 0.04	-0.168 ± 0.040	-6.53 ± 1.65

A t-test was performed for each property from the same bilayer type at the two pressures. Regarding κ^m, differences between the values at 1 bar vs. 1000 bar are significant ($p < 0.05$) for both bilayers. Regarding c_0^m, differences are significant for POPC but not for DOPC ($p = 0.10$). Regarding $\kappa^m c_0^m$, differences are again significant for POPC but not for DOPC ($p = 0.55$).

be easily obtained as the ratio between the first integral moment of $\Pi(z)$ and the monolayer bending modulus κ^m. The values obtained for these elastic properties at the studied pressures for each bilayer are presented in Table 4.2.

Our results for κ^m for both bilayers at 1 bar are consistent with previous experimental and computational measurements [180, 254, 262]. Regarding the effect of high pressure, our results show a slight decrease in κ^m at the increased pressure of 1000 bar, for both bilayers. A recent experimental study [284] on DOPC, which appears to be the first and so far only direct measurement of the bending rigidity of a lipid membrane under high pressure, shows a significant increase (up to a factor of 2) for external pressures of up to 400 bar. Interestingly however, for higher external pressures of up to 800 bar, the bending rigidity is then found to decrease down to the value observed at 1 bar.

For a symmetrical bilayer, the monolayer spontaneous curvature c_0^m measures the intrinsic tendency of each of the monolayers to curl. Conventionally, the magnitude of c_0^m quantifies a leaflet's desire to either curl towards the water phase in order to form inverse structures (for $c_0^m < 0$) or to curl away from the water phase to form micellar structures (for $c_0^m > 0$). When the magnitude of c_0^m is small, the tendency to curl is not satisfied, and the monolayers assemble symmetrically to form a flat lamellar bilayer. Table 4.2 shows that, at 1 bar, both DOPC and POPC bilayers are characterized by small negative values of c_0^m, consistent with the well-known experimental behavior whereby these lipids form standard lamellar

bilayer phases (as opposed to micelles or inverse phases); furthermore, the specific values obtained are in good agreement with previous literature [66, 239, 241, 254]. At the increased external pressure of 1000 bar, c_0^m for POPC decreases (becomes more negative) whereas no statistically significant change is observed for DOPC (Table 4.2). The increased unsaturation level in DOPC with respect to POPC is therefore correlated with a resistance to changes in spontaneous curvature under high pressure. To our knowledge, no experimental measurement or other simulation study on the pressure dependence of the spontaneous curvature has been previously reported in the literature.

The quantity $\kappa^m c_0^m$ characterizes the membrane curvature frustration energy, also known as torque tension; it is a fundamental biophysical property that underlies mechanisms by which lipids can modulate the structure and function of membrane proteins [17, 53, 210]. Our results are in fair agreement with available experimental measurements [66] conducted at atmospheric pressure (1 bar), whereas no data are available at increased pressure. Considering the results obtained for our systems, we observe a statistically significant increase in the magnitude of $\kappa^m c_0^m$ under increased external pressure for POPC, whereas for DOPC there is no significant difference. It is interesting and relevant to compare our data with quantitative estimates, obtained theoretically by Cantor [53], of the changes in the product $\kappa^m c_0^m$ required to affect protein function. Specifically, from the analysis of collective rearrangements of simple geometric models of proteins, it was calculated [53] that significant shifts in protein conformational equilibria could be induced by changes in $\kappa^m c_0^m$ of order $1.2 \times 10^{-21}\,\mathrm{J\,nm^{-1}}$. From our data (Table 4.2), considering first DOPC, we can calculate that increasing the pressure from 1 to 1000 bar induces changes in $\kappa^m c_0^m$ of magnitude $1.1 \times 10^{-21}\,\mathrm{J\,nm^{-1}}$, which is below Cantor's threshold, and anyway not statistically significant. For POPC however, the change in pressure brings about a substantially larger change in $\kappa^m c_0^m$ of magnitude $4.2 \times 10^{-21}\,\mathrm{J\,nm^{-1}}$, which is well above Cantor's threshold, as well as being statistically significant. Therefore, at least in relation to Cantor's theoretical model [53], pressure-induced changes in $\kappa^m c_0^m$ would be large enough to alter protein conformational equilibria in a POPC bilayer, but not in a DOPC bilayer. Real systems are obviously much more complex, in that $\kappa^m c_0^m$ values will depend on the specific proteins as well as the lipid composition of the bilayer. Bearing this caveat in mind, our results nonetheless clearly suggest that

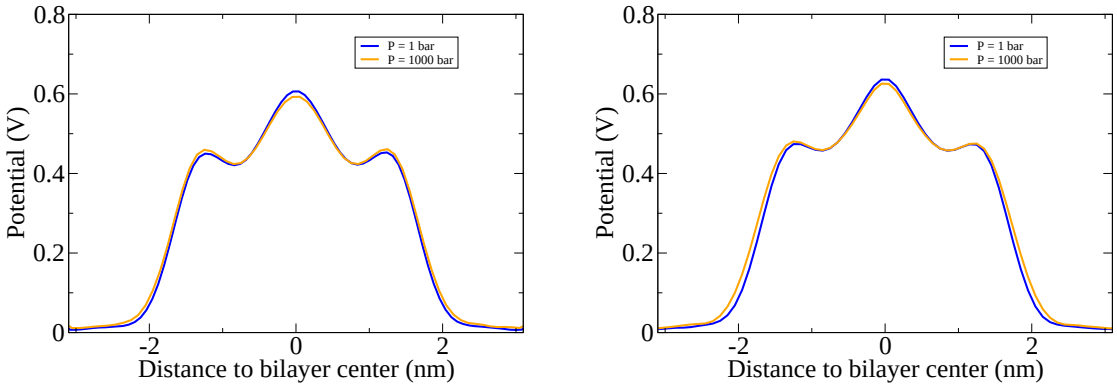

Figure 4.6: Dipole potential profiles for (a) DOPC and (b) POPC bilayers at 1 bar (blue) and 1000 bar (orange). Error bars are are smaller than the lines' thickness.

the response in terms of $\kappa^m c_0^m$ values to a change in pressure can be highly sensitive to the lipid type, and specifically to the level of unsaturation. In particular, the mono-unsaturated POPC is found to be very sensitive to an increase in external pressure, with a much amplified effect on $\kappa^m c_0^m$ compared to the bi-unsaturated DOPC, for which the change with pressure is not significant.

4.3.6 Dipole potential profile

The electrostatic dipole potential profiles $\Psi(z)$ for the investigated DOPC and POPC bilayers at 1 bar and 1000 bar are shown in Figure 4.6. Interestingly, in this case, it can be seen that the change in pressure does not induce any substantial change in the dipole potential of either bilayer. The absence of pressure-induced effects was confirmed by further decomposition of $\Psi(z)$ into the individual contributions from water and lipid molecules (data not shown); these results are consistent with previous reports obtained under standard ambient pressure [92, 277, 327]. Particularly, for both bilayers, the contribution due to water is largely positive, determines the sign of overall profile, and is compensated by the negative lipid contribution. We are not aware of previously reported dipole potential data at other pressures, from either experiments or simulations. Overall, our results show that the dipole potential is

Table 4.3: Average number of hydrogen bonds formed between lipid head groups and water molecules

Number	DOPC		POPC	
of H-bonds	1 bar	1000 bar	1 bar	1000 bar
Head-Water	6.87 ± 0.04	6.91 ± 0.03	6.60 ± 0.03	6.66 ± 0.03
Head-Head	0.34 ± 0.02	0.34 ± 0.01	0.38 ± 0.01	0.39 ± 0.01

not sensitive to changes in the external hydrostatic pressure, irrespectively of the type of lipid.

4.3.7 Hydration and permeation

To investigate more closely the interaction of the bilayers with water, we computed the individual electron density contribution for water (Figure 4.3). The data obtained show that the response to the pressure change does not significantly alter the hydration features of the bilayer.

We also quantified the lipid headgroup orientation by calculating the angle between the lipid head P-N vector and the z-axis (i.e., the bilayer normal). For DOPC, the angle is 69.53 ± 0.20 degrees at 1bar and 69.24 ± 0.23 degrees at 1000 bar, while for POPC it is 69.38 ± 0.22 degrees at 1bar and 69.54 ± 0.22 degrees at 1000 bar. Statistically, the differences for both pairs are not significant ($p > 0.05$). Incidentally, the absence of a significant effect on the headgroup orientation is consistent with the results obtained for the dipole potential, when one considers that the P-N vector is the main contributor (in terms of magnitude) to the overall dipole potential. The results obtained show that, for both the POPC and DOPC bilayers, the headgroup orientation does not change significantly in response to the imposed pressure increase. Incidentally, the absence of a significant effect on the headgroup orientation is consistent with the results obtained for the dipole potential, when one considers that the P-N vector is a major contributor to the overall dipole potential.

The lipid headgroups were also analyzed in terms of their hydrogen bonding with water. Consistently with the electron density data on the headgroup hydration, no significant difference was found in the number of hydrogen bonds upon increasing the external pressure (Table 4.3).

To study the permeation of water through the bilayers, we calculated the number

of water molecules crossing the bilayers during the simulation. For POPC, the number of crossing events was 54 ± 8 at 1 bar and 14 ± 2 at 1000 bar, the difference being statistically significant ($p = 0.04$). For DOPC, the number of water crossings was 52 ± 8 at 1 bar and 33 ± 3 at 1000 bar; in this case the difference is not statistically significant ($p = 0.15$). Note that, to be able to estimate the standard errors, for each system we counted separately the crossings along the two directions aligned and anti-aligned the z axis, thus obtaining two data values for each systems.

4.4 Conclusions

In this chapter, we employed fully atomistic molecular dynamics simulations to investigate the effects of a high external pressure of 1000 bar, compared to the ambient value of 1 bar, on a number of key physical properties of lipid bilayer systems. In particular, we studied and compared systems comprising either bi-unsaturated DOPC or mono-unsaturated POPC lipids. With the exception of the electrostatic dipole potential profile and headgroup hydration, the properties investigated were shown to be significantly affected by the pressure increase in both bilayers. Notably, for most properties the effects are amplified for the POPC bilayer, especially in relation to lipid area, chain order parameters, lateral pressure profile, spontaneous curvature and curvature frustration energy. Regarding the structural properties, our results provide molecular-level evidence to previous theoretical understanding that increased unsaturation results in a stronger resistance to structural change in response to high pressure [329]. In particular, the existence of two unsaturated bonds (one in each tail) in the chemical structure of DOPC explains the less pronounced mechanical response to high pressure compared to the amplified response obtained for POPC, which features only one unsaturated bond. Moreover, the change in the curvature frustration energy $\kappa^m c_0^m$ was also much more pronounced for POPC; specifically, it was found to be significantly and substantially above a threshold value predicted to be required in order to affect the conformational equilibria of membrane-embedded proteins [53], whereas for DOPC we obtained a value below such threshold and not statistically significant.

The lower unsaturation level in POPC with respect to DOPC seems therefore to make most physical properties of the corresponding bilayer more sensitive to high

pressure. Conversely, increased unsaturation for DOPC correlates to higher resistance to changes in physical properties under increased pressure. More generally, our results provide a quantitative molecular-level basis to rationalize the experimental observation that bacteria adapted to live under high hydrostatic pressure in the deep sea are characterized by higher ratios of unsaturated fatty acids in the lipid membrane [23, 84, 164, 278]. Future work will involve simulations of more complex systems, especially including membrane proteins, aimed at quantifying high pressure effects on specific biological processes in relation to lipid diversity.

Chapter 5

Pressure- and temperature-dependent characteristics of the ELBA coarse-grained water model

The ELBA coarse-grained model describes a water molecule as a single-site Lennard-Jones particle embedded with a point dipole. ELBA has been previously reported to capture several properties of real water with relatively high accuracy, while being up to two orders of magnitude more computationally efficient than atomistic models. In this chapter, the ELBA model is 'stress tested', by investigations into the temperature- and pressure-related characteristics. In particular, temperature- and pressure-dependences of two most important water properties, the liquid density and the self-diffusion coefficient are studied; thermodynamic properties that reflects derivative changes at ambient conditions in response to pressure or temperature fluctuations, namely the isothermal compressibility, isobaric heat capacity, and thermal expansion coefficient, are also caculated. For temperature- and pressure-dependences, molecular dynamics simulations are performed spanning temperatures from 268 K up to 378 K and pressures from 1 atm up to 4000 atm. Comparisons are made with literature data from experiments and from simulations of traditional 3-site atomistic models. Remarkably, the ELBA results show an overall similar (and

sometimes higher) accuracy with respect to the atomistic data. For thermodynamic properties, the accuracy of ELBA is relatively good compared to atomistic and other coarse-grained models.

5.1 Introduction

Water is a non-negligible part in a biomembrane system. Not only it accounts for a substantial ratio of the system in molecule amounts, but also water-biomolecule interations contribute significantly to the behaviour of the system. The modelling and simulation of water is of great interest for both academic research and industrial applications. Numerous water models, with various characteristics and capabilities, have been developed over several decades now [127, 130, 138, 360]. A popular approach involves atomistic models where each atom in the water molecule is represented by a simulated site [26, 28, 160], although optimised models also exist which include one or two extra sites [4, 162, 203]. While the simulations of atomistic models can provide accurate and realistic results, they are also highly demanding of computational resources. To reduce the computational cost, simplified models can be developed by representing one or several water molecules with lower-resolution single sites; in this approach, known as 'coarse-graining', some atomic-level details are sacrificed to increase simulation efficiency [234, 252, 254, 296, 366].

The ELBA coarse-grained model has been developed to attempt striking a new balance between physical accuracy and simulation efficiency [243, 249, 251]. In the ELBA model, the three atoms of a water molecule are reduced to a single particle, with an electrical point dipole affixed to its centre to capture the well-known dipolar nature of water. Previous molecular dynamics simulations have shown relatively good accuracy of the ELBA model under ambient conditions of temperature and pressure. In particular, ELBA reproduced several fundamental water properties as accurately as the best atomistic models, including density, potential energy, self-diffusion coefficient, heat of vaporisation, critical point, surface tension and the liquid-vapour interface structure [243]. A significant issue was however observed for the radial distribution function, which showed qualitative and quantitative differences compared to experimental and atomistic data [243].Notably, ELBA can also be used to hydrate atomistic solutes, including small organic molecules and proteins;

in particular, uniquely for a coarse-grained model, ELBA was shown to be *directly* compatible with common atomistic force fields, meaning that no additional or ad hoc scaling factors, intermediate regions, or extra sites were required [244]. In terms of computational cost, ELBA proves to be between one to two orders of magnitude more efficient to simulate than traditional multi-site atomistic models [243].

While ambient conditions are obviously of primary importance, there is also substantial interest in applying molecular simulations to investigate phenomena which take place under a variety of temperatures and pressures, such as protein folding processes [167, 191] and water filtration [100]. Hence, it is important to assess how well a water model can predict real water behaviour at non-ambient conditions. In this work, the performance of the ELBA model (with no modification to the original parameters) is examined over a wide range of temperatures (268 K to 378 K) and pressures (1 atm to 4000 atm). We investigate the temperature and pressure dependences of two fundamental water properties, the liquid phase density and self-diffusion, which ELBA reproduces accurately under ambient conditions [243]. Comparison are made with corresponding experimental data and simulation results for the atomistic models SPC [28], SPC/E [26] and TIP3P [160], which represent the most widely-used water models in molecular simulation. As extra findings, we also compute the pressure dependence of liquid density and self-diffusion coefficient at room temperature for, respectively, TIP3P and SPC. To our knowledge, these properties have not been previously published.

Additional temperature- or pressure-related thermodynamic properties are calculated here for ELBA at ambient conditions, namely, isobaric heat capacity, thermal expansion coefficient, and isothermal compressibility. For these properties, literature data exist also from simulation of other coarse-grained models, which are thus included in the comparison.

5.2 Methods

5.2.1 ELBA coarse-grained model

The ELBA model describes a water molecule as a single Lennard-Jones particle embedded with a point dipole (Figure 5.1) [243, 249].

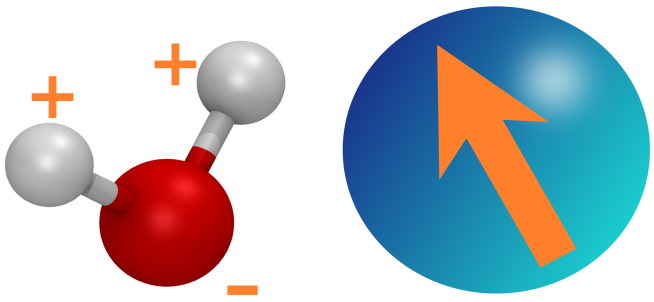

Figure 5.1: Atomistic water molecule and the ELBA model. The left panel shows a water molecule at the atomic level, with a negative charge ("−" sign) on the oxygen atom and two positive charges ("+" signs) on the hydrogen atoms. The right panel depicts an ELBA water site, with the arrow representing an electrical point dipole.

The potential energy U_{ij} for a pair of water particles i and j is the sum of a Lennard-Jones interaction term U_{LJ} and a dipole interaction term U_{dip}:

$$U_{ij} = U_{\mathrm{LJ}} + U_{\mathrm{dip}}. \tag{5.1}$$

Both terms are in the 'shifted-force' form [9, 292], whereby the potential energy and its derivative (the force) go to zero smoothly at the cut-off point. The shifted-force scheme removes cutoff-related artefacts and simulation stability problems [9, 292], which are especially severe for orientation-dependent potentials such as the point dipole potential [6]. For the Lennard-Jones part, the following expression proposed by Stoddard and Ford [336] is adopted:

$$U_{\mathrm{LJ}} = 4\epsilon \left\{ \left[\left(\frac{\sigma}{r}\right)^{12} - \left(\frac{\sigma}{r}\right)^{6} \right] + \left[6\left(\frac{\sigma}{r_c}\right)^{12} - 3\left(\frac{\sigma}{r_c}\right)^{6} \right] \left(\frac{r}{r_c}\right)^{2} - 7\left(\frac{\sigma}{r_c}\right)^{12} + 4\left(\frac{\sigma}{r_c}\right)^{6} \right\}, \tag{5.2}$$

in which σ and ϵ have the standard meaning [9, 292], r is the inter-particle distance, and r_c is the cut-off radius. For the dipole interactions, the classic electrostatic

model [9, 283] has been modified [243, 251] as:

$$U_{\text{dip}} = \frac{1}{4\pi\varepsilon_0} \cdot \left[1 - 4\left(\frac{r}{r_c}\right)^3 + 3\left(\frac{r}{r_c}\right)^4\right] \cdot \left[\frac{1}{r^3}(\boldsymbol{\mu}_i \cdot \boldsymbol{\mu}_j) - \frac{3}{r^5}(\boldsymbol{\mu}_i \cdot \boldsymbol{r})(\boldsymbol{\mu}_j \cdot \boldsymbol{r})\right], \quad (5.3)$$

where ϵ_0 is the vacuum permittivity, $\boldsymbol{\mu}_i$ and $\boldsymbol{\mu}_j$ are the point dipole vectors of the interacting pair, $\boldsymbol{r}$ and r are, respectively, the distance vector and its magnitude, and r_c is the cut-off distance. Values of the potential parameters used here follow conventional settings [243]: $\epsilon = 0.55$ kcal mol^{-1}, $\sigma = 3.05$ Å, $\mu = 2.6$ D and $r_c = 12.0$ Å.

5.2.2 General simulation details

Molecular dynamics simulations were performed using the software LAMMPS (version 11 Nov 2013) [1, 274]. Input scripts are available on our group website [3]. The simulation systems contained 8000 water sites in a cubic region. Conventional periodic boundary conditions were adopted. Conditions of constant temperature and pressure were applied in most of the simulations; in these cases, the edge length of the starting simulation box was set to 6.2 nm, yielding an initial water density of approximately 1 g cm^{-3} (consistent with the density of real water at standard ambient conditions). However, in some cases (detailed below), we fixed the volume, and hence also the system density, to a constant value. In all simulations, the temperature was controlled using the Langevin thermostat [313], with a collision frequency of 1 ps^{-1}. The pressure was maintained (when needed) using the barostat by Berendsen *et al.* [29], with a damping time of 1 ps and a bulk modulus of 2.174×10^4 atm. The integration time step for the ELBA simulations was 10 fs. At every time step, the net momentum of the mass centre of the entire system was removed to prevent drifting during the simulation. The interaction cutoff radius was 12 Å and no long range interactions (beyond the cutoff distance) were included for the ELBA model. All these settings are consistent with previous work [243]. Additional atomistic simulations were also run to study the pressure dependence of the TIP3P density and the SPC diffusion coefficient, as no corresponding results were found in the literature. For these simulations the time step was 2 fs. Bonds and angles were constrained using the SHAKE algorithm [304] with a relative tolerance

of 10^{-4}. The nonbonded cutoff distance was 10 Å for SPC [243] and 13 Å for TIP3P [243, 282]. Long range electrostatic interactions were included with the PPPM method [143] with a relative tolerance of 10^{-5}.

Specific details of individual calculations are given below in Section 5.2.3.

5.2.3 Details of individual calculations

To investigate density, self-diffusion, isothermal heat capacity, thermal expansion coefficient and isothermal compressibility, we ran series of 7 ns long simulations. The initial 2 ns were regarded as equilibration, while the subsequent 5 ns were considered as production; during production, the relevant properties were sampled every 0.1 ps. For each simulation, three independent repeats were run by assigning the initial velocities with different random seeds.

Calculations of density and self-diffusion coefficient followed standard procedures [127, 292]. Regarding isothermal heat capacity, thermal expansion coefficient and isothermal compressibility, details are given in the following Sections 5.2.3, 5.2.3 and 5.2.3, respectively.

Isobaric heat capacity

The isobaric heat capacity C_p at 298 K was estimated as [299]:

$$C_p = \frac{E_2^{tot} - E_1^{tot}}{T_2 - T_1} + \frac{\partial Q}{\partial T}, \tag{5.4}$$

where E_1^{tot} and E_2^{tot} are the total energies per molecule at temperature $T_1 = 288$ K and $T_2 = 308$ K. The second term at the right hand side of the equation is the quantum contribution, which for classical molecular simulations is about $-9.3\,\mathrm{J\,mol^{-1}K^{-1}}$ under standard ambient conditions [119, 146, 299].

Thermal expansion coefficient

The thermal expansion coefficient α at 298 K was estimated using the finite-difference expression method [119, 348]:

$$\alpha = \frac{1}{V}\left(\frac{\partial V}{\partial T}\right)_p \approx -\left(\frac{\ln\left(\frac{\rho_1}{\rho_2}\right)}{T_2 - T_1}\right), \tag{5.5}$$

where V is the simulation box volume, and ρ_1, ρ_2 are the densities at temperature T_1 (288 K) and T_2 (308 K), respectively.

Isothermal compressibility

The isothermal compressibility κ_T was calculated from two sets of constant-volume (and hence also constant-density) simulations, by applying the finite-difference equation as follows [119, 299]:

$$\kappa_T = -\frac{1}{V}\left(\frac{\partial V}{\partial P}\right)_T \approx -\left(\frac{\ln\left(\frac{\rho_1}{\rho_2}\right)}{P_2 - P_1}\right), \tag{5.6}$$

where P_1 and P_2 are the pressures corresponding to the constant density values of respectively ρ_1 (0.947g/cm^3) and ρ_2 (1.047g/cm^3). These density values were fixed at the outset by setting the system volume accordingly.

5.3 Results and discussion

5.3.1 Temperature dependence

The density and the self-diffusion coefficient of the ELBA water have been calculated at temperatures ranging from 268 K and 378 K, under a constant pressure of 1 atm. Results for both properties are compared with previously published results from experiment and from simulations of the widely-used 3-site atomistic water models SPC, SPC/E, and TIP3P [19, 126, 160, 161, 361].

Figure 5.2 shows the density data as a function of temperature. Compared

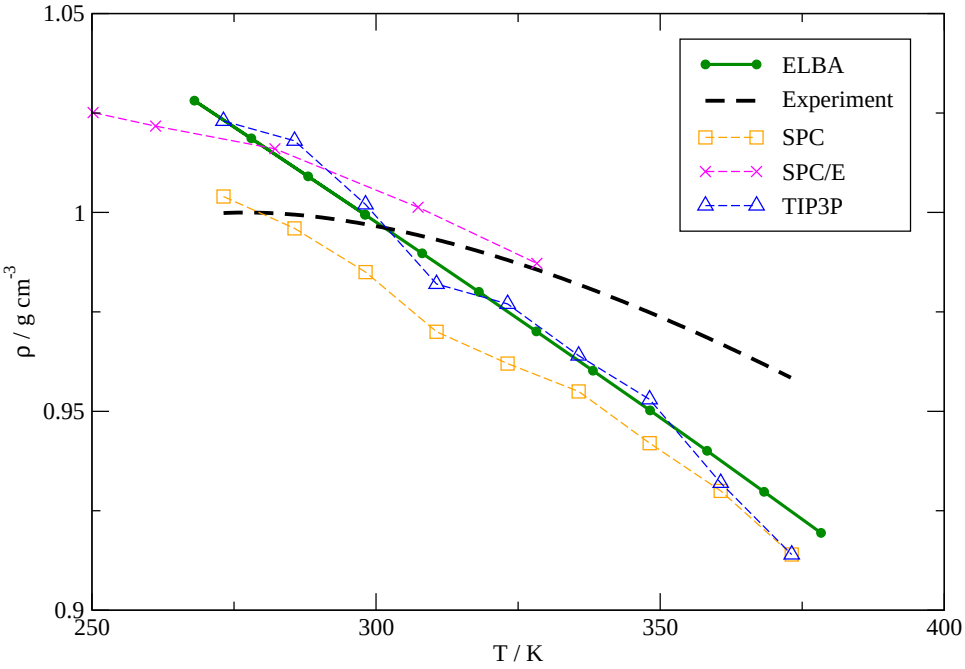

Figure 5.2: Density as a function of temperature at 1 atm. The standard deviation of the ELBA data is less than 0.00005 g cm^{-3} for all values; corresponding error bars are smaller than the size of the symbols. The experimental data are from the NIST database [188]. Atomistic data are from Paschek [265].

to the experimental data, it is clear that the ELBA results exhibit a larger rate of change with temperature in comparison to real water. Specifically, the ELBA results underestimate the density above room temperature while overestimate it below room temperature. Note however that the discrepancies observed are not particularly severe; the largest error, at around 373 K, is ∼0.03 g cm^{-3}, which corresponds to a relative error of only ∼3% with respect to the experimental measurement. When compared to the data from the atomistic models, the ELBA results are remarkably accurate (where *accurate* is intended to mean *close to the experimental value*). In particular, ELBA proves more accurate than SPC for temperatures above ∼285 K. ELBA is also more accurate than TIP3P for temperatures above ∼290 K. However,

ELBA is less accurate than SPC/E for all temperatures.

The self-diffusion coefficient data as a function of temperature are displayed in Figure 5.3. It can be seen that the ELBA results exhibit a lower rate of change with

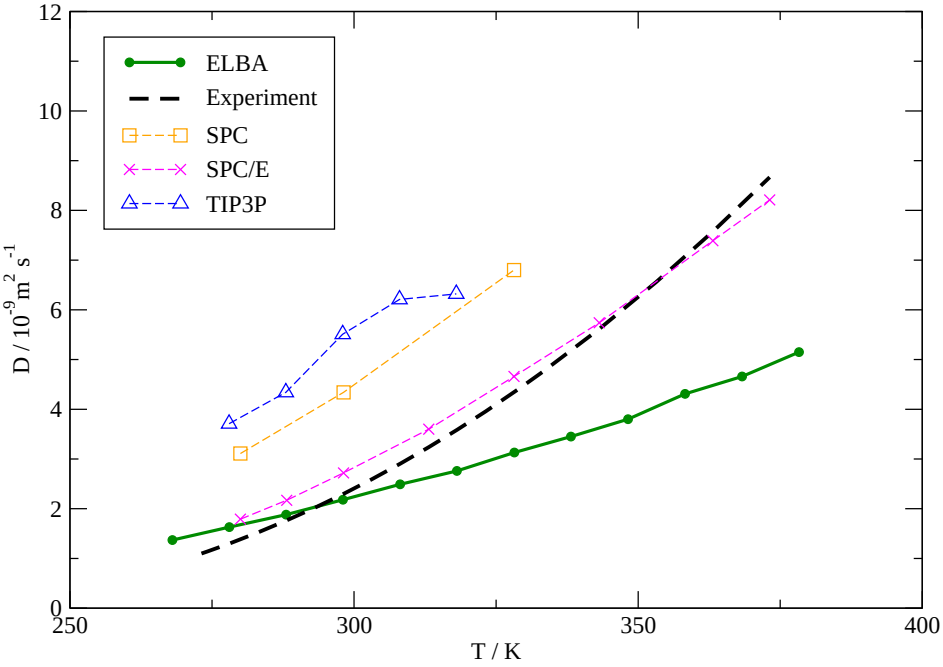

Figure 5.3: Self-diffusion coefficient as a function of temperature at 1 atm. The standard deviation for the ELBA results is at most 0.05 $\times$ 10^{-9} m^2 s^{-1}; corresponding error bars are of the order of the size of the symbols. The experimental data [144], as well as results for SPC [126], SPC/E [126] and TIP3P [361] are shown for comparison.

temperature in comparison to real water. In terms of absolute values, the accuracy of ELBA is rather good in a fairly large region centred around room temperature (approximately from 270 K to 320 K). In this region, ELBA is substantially more accurate than SPC and TIP3P, and largely as accurate as SPC/E. For temperatures above $\sim$320 K, the ELBA values increasingly diverge from the experimental curve, indicating that the mobility of the ELBA water is less sensitive than real water to

the temperature increase.

5.3.2 Pressure dependence

The pressure dependence of ELBA was investigated by applying external isotropic pressures from 1 atm to 4000 atm while maintaining a standard ambient temperature of 298 K. From Figure 5.4, it can be seen that the ELBA results are close to experiment only in the initial region around ambient condition, while they increasingly underestimate the experimental values with increasing pressure. This implies that

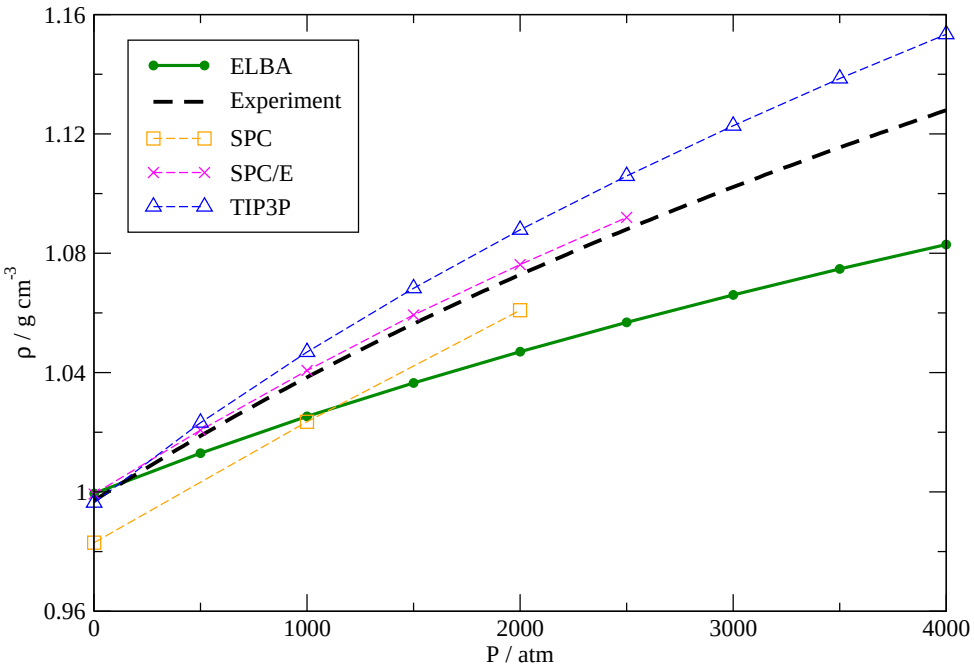

Figure 5.4: Density as a function of pressure at 298 K of ELBA, together with experimental data [188] and simulation results for SPC [286], SPC/E [286] and TIP3P (this work). The standard deviations for the ELBA and TIP3P results are at most 0.00005 g cm^{-3} and 0.00007 g cm^{-3}, respectively; corresponding error bars are smaller than the size of the symbols.

ELBA is less compressible by high pressure than real water. Compared to the atomistic models, ELBA is markedly less accurate than both SPC/E and TIP3P, but it proves more accurate than SPC for pressures below 1000 atm.

Regarding the self-diffusion coefficient, Figure 5.5 shows that the accuracy of ELBA is rather high at ambient pressure, but it decreases with increasing pressure, as the experimental values are more and more underestimated. Nevertheless, ELBA proves markedly more accurate than both SPC and (especially) TIP3P, while the SPC/E data almost match the experimental values.

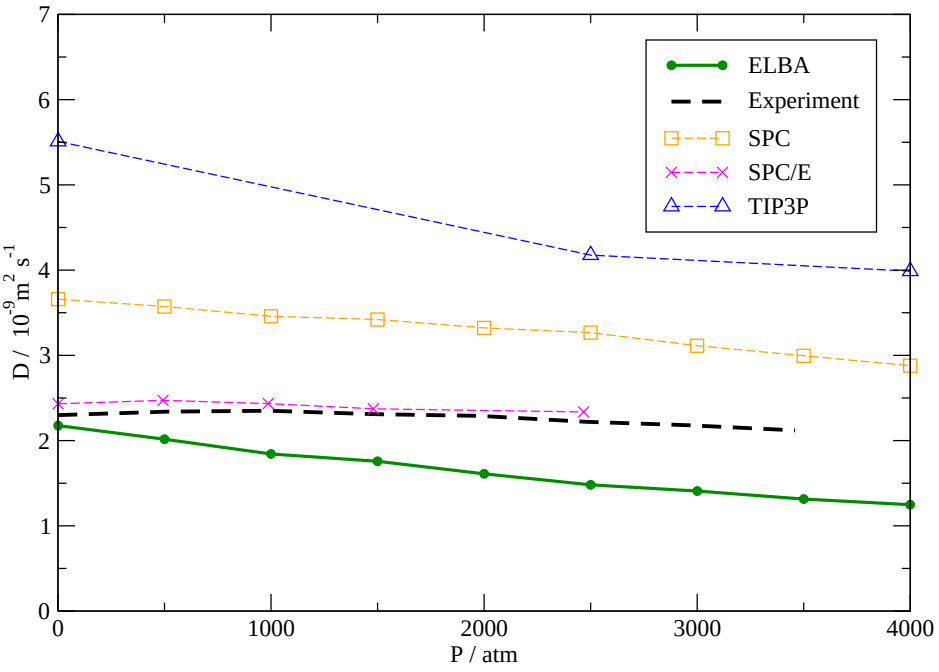

Figure 5.5: Self-diffusion coefficient as a function of pressure at 298 K. Results from experiment [136] and for SPC (this work), SPC/E [287] and TIP3P [118] are shown for comparison. The standard deviation for the ELBA and SPC values are at most 0.018 $\times 10^{-9}$ m^2 s^{-1} and 0.23 $\times 10^{-9}$ m^2 s^{-1}, respectively; corresponding error bars are of the order of the size of the symbols.

5.3.3 Thermodynamic properties at ambient conditions

Results for the thermodynamic properties of the ELBA model at 298 K and 1 atm are presented in Table 5.1, together with literature data from experiments, 3-site atomistic models, and also other coarse-grained models. The atomistic models are SPC [28], SPC/E [26] and TIP3P [160], already used as standards for comparison in the temperature and pressure dependences reported in the previous section. Regarding the other coarse-grained models, comparable results have been reported for single-site models (like ELBA) and for 'coarser' descriptions, whereby several water molecules are reduced to a smaller number of coarse-grained particles. Considering single-site models, relevant data have been reported in the literature for the SSD, mW, and MS-CG models. SSD is a model comprising a Lennard-Jones sphere, a point dipole, and an octupolar term used to capture hydrogen bonding. SSD has been used to study water in the liquid and ice phases [59, 102, 103, 194], and as a solvent for different systems [194, 221, 247, 257, 260]. The mW model is characterised by a three-body term that captures tetrahedral coordination [224]. MS-CG is a model consisting of an effective potential obtained by the force-matching method [154]. The BMW model [379] is a coarser model that reduces four water molecules to three charged sites, with the Born-Mayer-Huggins potential replacing the conventional Lennard-Jones potential. BMW has been applied to study the solvation and aggregation of peptides [380]. MARTINI is a popular model based on the Lennard-Jones potential, without explicit electrostatics, where each site represents four water molecules [207]. P-MARTINI [382] refers to a polarizable variant of MARTINI which comprises three sites, two of which are oppositely charged. The GROMOS model [299] maps five water molecules to two oppositely charged sites. This model has also been used as a solvent for proteins [297]. WT4 is a model that represents clusters of 11 water molecules by tetrahedral particles comprising 4 charged sites [75]. WT4 has been used as a solvent for ions and nucleic acids [75].

Regarding the isobaric heat capacity C_p, the ELBA result is lower than the experimental value. This could be expected since there is no explicit hydrogen-bonding network in the ELBA model. In fact, the high heat capacity of real liquid water is believed to be partly due to the presence of hydrogen bonds, because

when water is heated, the corresponding energy is partly used to bend or break the hydrogen bonds, rather than being totally transferred to the kinetic energy of the water molecules [94, 193]. Quantitatively, the difference between ELBA and the experimental value is ∼10 J mol^{-1} K^{-1}, corresponding to a relative error of 14.5%. Compared to the atomistic models, ELBA proves slightly more accurate than SPC/E, for which the relative error is 15%; however, SPC and TIP3P are in turn markedly more accurate than ELBA, with relative errors of 0.3% and 4%, respectively. As for the other coarse-grained models, it can be seen that mW is characterised by a C_p value that is less than half the experimental value. The WT4 model also underestimates C_p, being 43% lower than the experimental measurement. Both the SSD and GROMOS models instead overestimate C_p, although with rather different relative errors of respectively 60% and 7%.

Regarding the thermal expansion coefficient α, it can be seen that the ELBA value is not very accurate, as it is almost 4 times larger than the experimental value. However, in comparison with the atomistic models, the accuracy of ELBA is relatively good, being within the range reported for SPC and TIP3P (which have α values about 3 to 5 times larger than the experimental value). The SPC/E result is the most accurate, even though it is still over twice as large as the experimental result. It should be pointed out that these results are consistent with the temperature dependent density data reported in Figure 5.2, where all densities from simulations show a larger rate of change with temperature with respect to the experimental data. Specifically, as the density of the models decreases faster than experimentally observed with increasing temperature, the thermal expansion coefficient is expected to be overestimated. Compared with the other coarse-grained models, ELBA proves slightly more accurate than WT4 and substantially more accurate than GROMOS and MS-CG.

As for the isothermal compressibility κ_T, the ELBA model underestimates the experimental value by ∼36%, while the atomistic models all prove more accurate, with relative errors in the range from 4% to 28%. Compared with the other coarse-grained models, ELBA is instead more accurate than all but one model (BMW).

5.4 Conclusion

We have studied the temperature and pressure dependences of density and self-diffusion for the coarse-grained ELBA water model. Notably, the accuracy of ELBA was found to be overall comparable to that of the standard 3-site atomistic models, in that the relative errors with respect to experiment obtained with ELBA were mostly within the range of errors characterising the atomistic models. In fact, in some cases ELBA was shown to be even more accurate than some of the atomistic models.

Moreover, we computed thermodynamic properties at standard ambient conditions, namely isothermal compressibility, isobaric heat capacity and thermal expansion coefficient, for which comparisons could also include other coarse-grained models. For the thermal expansion coefficient and the isothermal compressibility, ELBA proved less accurate than the atomistic models, but more accurate than the other coarse-grained models. Regarding the heat capacity, ELBA was shown to be as accurate as SPC/E and more accurate than most available coarse-grained models.

Together with the previous demonstration of the direct compatibility of ELBA with atomistic force fields for organic molecules and proteins [244], the work presented here opens up a range of opportunities for mixed atomistic/coarse-grained simulations under non-ambient conditions of temperature and pressure.

Table 5.1: Thermodynamic properties at ambient conditions[a]. Isobaric heat capacity: C_p. Thermal expansion coefficient: α. Isothermal compressibility: κ_T. Melting point: T_m. Shear viscosity: η. The ELBA results are reported as 'average $\pm$ standard deviation'. A 'mapping' entry $m \to n$ indicates m water molecules are modelled by n sites.

	mapping	C_p ($\mathrm{J\,mol^{-1}K^{-1}}$)	α ($10^{-4}\mathrm{K^{-1}}$)	κ_T ($10^{-5}\mathrm{atm^{-1}}$)
ELBA	$1 \to 1$	64.37 ± 0.17	9.64 ± 0.03	2.914 ± 0.004
Experiment[b]		75.3	2.56	4.53
SPC[c]	$1 \to 3$	75.6	7.3, 10.6[d]	4.74
SPC/E[b]	$1 \to 3$	86.6	5.6[c]	4.67, 5.17[c]
TIP3P[b]	$1 \to 3$	78.41	9.2[e], 14.4[d]	5.81
SSD[f]	$1 \to 1$	120.5 ± 0.5	-	-
mW[g]	$1 \to 1$	33	-	1.9
MS-CG[h]	$1 \to 1$	-	25.0	14.7
BMW[i]	$4 \to 3$	-	-	3.3
P-MARTINI[k]	$4 \to 3$	-	-	-
MARTINI[l]	$4 \to 1$	-	-	2.6[i], 6.1
GROMOS[m]	$5 \to 2$	80.7	23	8.4 to 13.8
WT4[n]	$11 \to 4$	43[o]	11.6	2.46

[a]Temperature of 298 K and pressure of 1 atm, unless otherwise stated
[b]Reference [360]
[c]Reference [119]
[d]Reference [161]
[e]Reference [361]
[f]Reference [102]
[g]Reference [224], κ_T at 300 K
[h]Reference [154], at 300 K
[i]Reference [379], at 300 K
[j]Reference [39], at 300 K
[k]Reference [382]
[l]Reference [206], at 300 K
[m]Reference [299]
[n]Reference [75]
[o]Reference [77], value for a WT4 and SPC mixture.

Chapter 6

Folding Free Energy Landscape of Atomistic Protein Structures Solvated in Coarse-Grained ELBA Water

The ELBA water model has been applied in dual-resolution simulations of hydrated biomolecule systems. In specific, molecules represented with standard all-atom force fields are solvated in ELBA water. A unique characteristic of this methodology is that the mixing of resolutions is direct, meaning that no additional or *ad hoc* scaling factors, intermediate regions, or extra sites are required. To validate the methodology, hydrating properties from several aspects have been studied, including the hydration free energy of AA sidechain analogs, the stability of a typical full protein, etc [244]. Here, we compute folding free energy landscapes of representative $\alpha-$helical and $\beta-$hairpin structures solvated in ELBA water, and compare the results against those applying the TIP3P water model. The parallel tempering technique is applied. Our dual-resolution method is found to be comparatively accurate as the atomistic simulation, but several times more computationally efficient.

6.1 Introduction

The lipid bilayer self-assembly as well as many other biological processes are facilitated by the hydrating force with water [21, 61]. The multitude of hydration models that have been proposed in the literature could reflect the relevance of water as a solvent in countless natural and industrial processes [12, 76, 89, 128, 130, 155, 360]. An important computational aspect in the simulation of explicitly hydrated systems is that the large majority of the computation time is typically spent calculating water-water interactions. It is therefore unsurprising that numerous methods and models have been developed to simplify the treatment of hydration, and hence reduce the corresponding computational cost. In this respect, an increasingly popular approach involves the development of particle-based coarse-grained (CG) models, where one or more water molecules are represented by single interaction sites [18, 130, 151, 153, 255, 259, 296, 320].

An interesting and potentially very useful issue to consider is whether and how CG water models can be used to hydrate molecules described by standard atomistic models. Such a dual-resolution approach is highly desirable, because it allows the CG efficiency to be combined with the accuracy and generality of atomistic force fields - at least in principle. In practice however, complications arise because the CG force fields are not normally compatible with the atomistic ones. In fact, existing dual-resolution hydration schemes rely on one or more of the following *ad hoc* procedures to couple CG water and atomistic solutes: extra parameters or scaling factors to calibrate the atomistic-CG interactions [221, 247, 257, 260, 297, 298, 373], specific parametrization of atomistic-CG interactions [133, 134, 216, 217, 321], additional CG virtual sites [87, 231, 305, 373], artificial relative dielectric permittivity between atomistic sites due to lack of CG water electrostatic screening [133, 305], additional layers of atomistic water between the atomistic molecules and the CG water [121, 231, 298], or "adaptive resolution" transition regions [34].

The ELBA water model has been employed to develop a new direct approach to CG hydration of atomistic molecules [244], where the two levels of resolution (atomistic and CG) coexist in the same simulation without requiring any *ad hoc* treatment of the mixed interactions. In the ELBA CG force field [242, 248], each water molecule is represented by a point dipole attached to the center of a Lennard-

Jones sphere; such a combination of potentials is also known as the Stockmayer model. While the idea of parametrizing a "Lennard-Jones plus point dipole" potential to model water solvation was proposed by Warshel already 35 years ago [372], the Stockmayer model has been almost exclusively employed to study idealized polar fluids [22, 79, 159, 233]. The ELBA model is characterized by a novel parametrization targeted to liquid water, and by an original "shifted-force" variant of the point dipole potential (which is crucial to the viability and efficiency of the model in molecular dynamics simulations; see more details in Section 2.3.2).

Previous multiscale simulations usually set more than one regions for the system with different mesoscopic scales. For example, the famous AdResS method contains two regions, with one in atomistic level and the other in coarse-grained level, and when a molecule passes from one region to another, its resolution level changes accordingly [279, 280]. Here, the approach is to directly mix the ELBA water and atomistic solvents together without such pre-treatments and transition regions. To show that the ELBA water model can be used straightforwardly to hydrate molecules described by standard atomistic force fields, we mix CG and atomistic interactions through simple shifted-force potentials, with mixed parameters determined from the same standard rules employed for interactions among the atomistic sites. Thus, for all the interactions in the system, Lennard-Jones cross terms are determined by the Lorentz-Berthelot combining rules [10] (which involve simple geometric and arithmetic means), and electrostatic cross terms are determined from classical Coulomb expressions, with the relative permittivity set to unity ($\epsilon_r = 1$). The validity of this approach has been firstly tested by computing the free energy of hydration for several atomistically-modeled small molecules (analogs of amino acids) solvated in ELBA water [244]. Many among the most fundamental (bio)molecular processes, such as self-assembly, ligand binding, transmembrane permeation, and protein folding, are regulated by the free energy of hydration, and hence its accurate reproduction is paramount. Our calculations have shown that the dual-resolution approach reproduces the experimental data as closely as corresponding results from fully atomistic simulations. Also, the hydration free energy of ELBA water is in even better agreement with experiment than several standard atomistic models.

Then in this chapter, the ELBA water is applied to solvate a full typical protein structure, comprising an α-helix and four β-strands, modeled with a standard all-

atom force field. we conduct parallel tempering simulations to study the folding free energy landscape of two typical α helical and β hairpin elements. The consistency was again found with those from an equivalent fully atomistic system.

The parallel tempering (or replica exchange) method tackles the notorious free energy barrier problem by running in parallel multiple replicas of the same system at a sequence of temperatures ranging from the desired temperature to a higher temperature at which the energy barrier could be easily overcome [148, 338]. During the simulation of the replicas, neibouring ones are swapped, behind which is essentially a Monte-Carlo thought: since the simulation at higher tempreratures could traverse the free energy barrier, the swap of a low temperature replica into a higher one facilitate it to overcome the quasi-ergodicity. Such a straightforward method is suitable to study the free energy landscape problem, and the two foundamental protein structures (i.e. the protein G C-terminal β hairpin and the Trp-cage α helical) have been previously used as typical assessment models of the solvation forcefield [338, 385].

6.2 Methods

6.2.1 Mixed atomistic-CG interactions

The ELBA forcefield can refer to Section 5.2. Atomistic protein molecules are described with the CHARMM General Force Field (CGenFF), [358] version 2b7. Considering an atomistic site i and a CG ELBA water site j, the pair potential energy U_{ij} is:

$$U_{ij} = U_{ij}^{\mathrm{LJ}} + U_{ij}^{\mathrm{qp}} \tag{6.1}$$

with U_{ij}^{LJ} the Lennard-Jones term and U_{ij}^{qp} the charge-dipole term. For the Lennard-Jones term, we use the same shifted-force potential that models the water-water interactions (Equation 5.2), but with σ and ϵ now representing the mixed i-j (atom-water) interactions. Such cross terms are assigned with the standard Lorentz-Berthelot rules: [10] $\sigma = (\sigma_i + \sigma_j)/2$, $\epsilon = \sqrt{\epsilon_i \epsilon_j}$. These are the same rules used to assign Lennard-Jones cross terms within purely atomistic interactions. For the electrostatic potential between the atomistic (partial) charges and the CG water

dipoles, we use a shifted-force charge-dipole potential: [248]

$$U_{ij}^{\mathrm{qp}} = \frac{q_i}{4\pi\varepsilon_0\varepsilon_r r^3}\left[1 - 3\left(\frac{r}{r_c}\right)^2 + 2\left(\frac{r}{r_c}\right)^3\right]\boldsymbol{p}_j \cdot \mathbf{r} \tag{6.2}$$

with q_i the atom partial charge, $\boldsymbol{p}_j$ the water dipole, ε_0 the vacuum permittivity, ε_r the relative permittivity, $\mathbf{r}$ the pair distance vector, r the magnitude of $\mathbf{r}$, and r_c the cutoff radius. Note that $\varepsilon_r = 1$, as for the electrostatic interactions within standard all-atom models.

6.2.2 General molecular dynamics details

Molecular dynamics simulations were run with the program LAMMPS, [1, 275] version 16 Aug 2013, modified to include the calculation of solute-solvent potential energies required for the free energy calculations. Complete command scripts and input files are The *charmm2lammps.pl* tool [1] was used to convert the original *CGenFF* topology and parameter files into LAMMPS input files (which require a different format, as well as conversions to different units for some of the parameters).

Nonbonded interactions within the atomistic models (small molecules and protein G) were computed using standard approaches. In particular, Lennard-Jones pair interactions were considered up to an atom-based cutoff distance of 12 Å; a switching function [201] was used to make both energies and forces go to zero smoothly between 11 and 12 Å. Lorentz-Berthelot combining rules [10] were used (as in both the original CHARMM and AMBER force fields [199, 367]). For the Coulombic interactions, a cutoff distance of 12 Å was set for the real space part, while long range interactions were included using the particle-particle particle-mesh (PPPM) solver, [142] with a relative tolerance of 10^{-5}. Intramolecular 1-2 and 1-3 nonbonded interactions were neglected, while 1-4 interactions were treated according to the rules for the corresponding force field. [199, 367]

In all pure AA or AA-CG mixed simulations, the integration timestep was 2 fs. The temperature was controlled using a Langevin thermostat [314] with a collision frequency of $1\,\mathrm{ps}^{-1}$. The pressure was controlled isotropically using the barostat by Berendsen et al. [31] with a damping time of 1 ps and an isothermal compressibility of $4.6 \times 10^{-5}\,\mathrm{atm}^{-1}$. For the atomistic solutes, bonds involving hydrogen atoms were

constrained using the SHAKE algorithm [304] with a relative tolerance of 10^{-6}.

6.2.3 Parallel tempering simulations

The parallel tempering (or replica exchange) method [148, 338] was applied to investigate the folding free energy of the C-terminal β hairpin of protein G (PDB code: 2GB1) and Trp-cage (PDB code: 1L2Y). The β hairpin and Trp-cage protein structures were solvated with respectively 1901 and 1885 water molecules. Each system was initially equilibrated for 2 ns at 300 K and 1 atm; in particular, during the first 1 ns, the protein atoms were restrained to their original positions by applying harmonic springs. The systems were then run for 100 ps in the NVT ensemble, and the final configurations were used as the starting points for the parallel tempering simulations. For both proteins, 60 replicas were simulated in parallel with temperatures spanning the range from 270 to 655 K [384, 385]. In particular, each replica was simulated for 3.5 ns. During the first 0.1 ns, exchanges were not attempted. During the remaining 3.4 ns, parallel tempering was performed with exchanges attempted every 0.4 ps, and configurations saved every 0.1 ps. The last 3 ns of every replica were used for data collection. For the β hairpin, the two reaction coordinates are the number of the native backbone-backbone hydrogen bonds excluding the two near the turn, and the radius of gyration of the side chain atoms of the four hydrophobic residues (Trp43, Tyr45, Phe52 and Val54). [93] For the Trp-cage, the fraction of native contacts (Q) and the radius of gyration of the α-carbon atoms (Rg) were chosen as the reaction coordinates; a native contact was defined when the distance of a pair of α-carbon atoms from nonadjacent residues is less than 6.5 Å [383]. Free energy landscapes were obtained from histogram analysis [105].

6.3 Results

The free energy landscapes obtained from the parallel tempering simulations of the the β hairpin are shown in 6.1. In particular, Figure 6.1a refers to the fully atomistic run (CHARMM protein with TIP3P water), and Figure 6.1b represents the results from the dual-resolution system (CHARMM protein with ELBA water).

It can be noticed that the two diagrams show qualitatively similar "L"-shaped

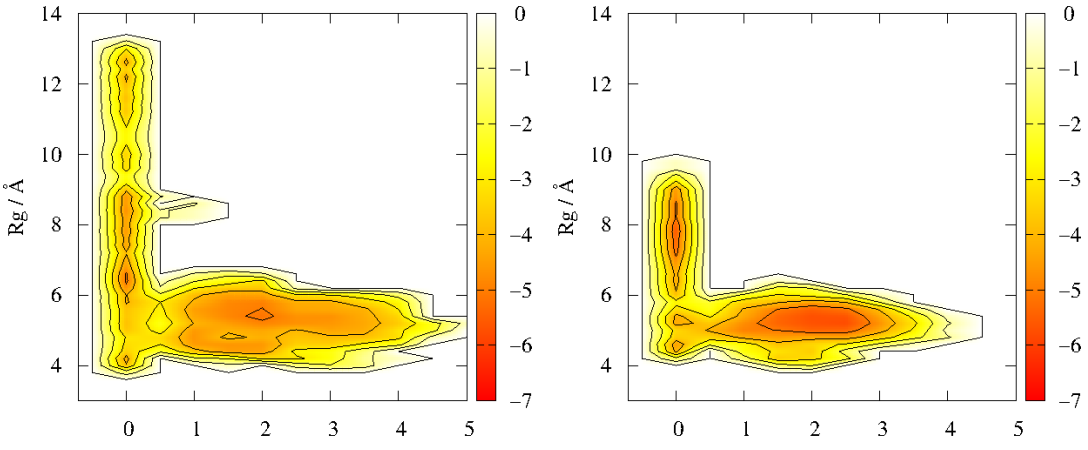

(a) All-atom (b) Dual-resolution

Figure 6.1: Free energy landscapes for β hairpin *vs* the two reaction coordinates, that is, number of H bonds and radius of gyration (Rg). The free energy is in units of k_BT, and contours are spaced with $1\,k_BT$ intervals. Panel (a): All-atom system. Panel (b): Dual-resolution system.

landscapes. To compare the two simulations quantitatively, we further compute the folding free energy. In particular, we consider folded and unfolded states when the number of hydrogen bonds is respectively greater or less than 1; [47] we can then calculate the folding free energy as $\Delta G = -RT \log(P_f/P_u)$ where P_f and P_u denote respectively the probabilities of the folded and unfolded states. The folding free energies obtained are respectively -0.43 kcal/mol and -0.39 kcal/mol for the all-atom and dual-resolution systems, showing reasonable agreement between the two approaches. In addition, the minimum locations of the folded and unfolded states in both system also show consistency, which is (2.0, 5.4) and (0.0, 6.4) for the all-atom system, while (2.5, 5.2) and (0.0, 7.6) for the dual-resolution system (N_{Hbond}, Rg).

Regarding Trp-cage, the free energy landscapes obtained from the parallel tempering simulations are shown in 6.2. In particular, Figure 6.2a refers to the fully atomistic run (CHARMM protein with TIP3P water), and Figure 6.2b represents the results from the dual-resolution system (CHARMM protein with ELBA water). It can be seen that the landscapes share qualitatively similar features, especially

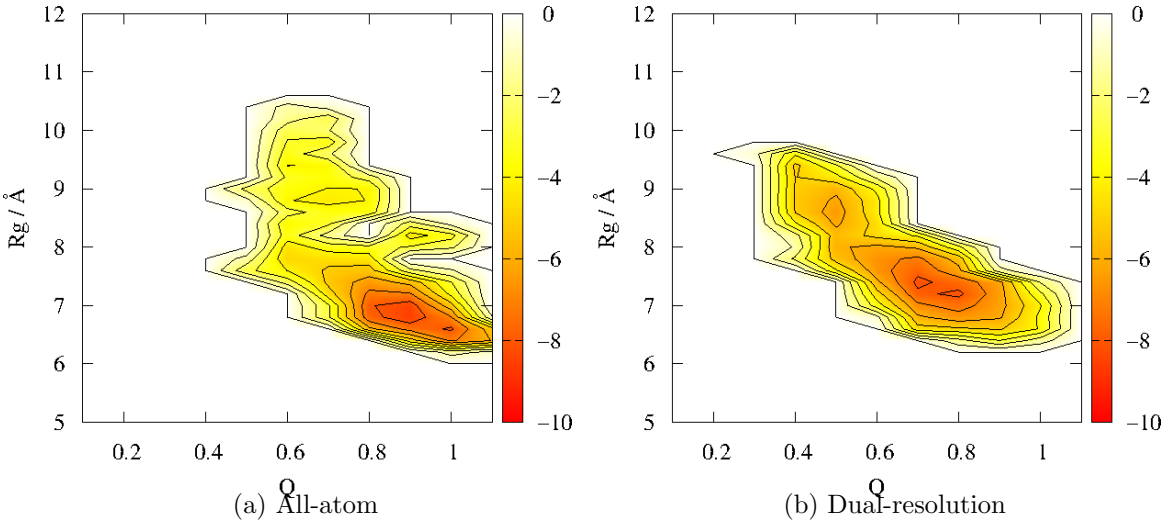

(a) All-atom (b) Dual-resolution

Figure 6.2: Free energy landscapes for Trp-cage *vs* the two reaction coordinates, that is, fraction of native contact (Q) and the radius of gyration of the α-carbon atoms (Rg). The free energy is in units of k_BT, and contours are spaced with $1\,k_BT$ intervals. Panel (a): All-atom system. Panel (b): Dual-resolution system.

with respect to the regions of lower free energy, whereas some differences are evident in the upper part of the landscapes, corresponding to regions of higher free energy. Importantly, both landscapes show a characteristic funnel-like pattern, and both display global minima at reaction coordinates near (0.8, 7). With respect to the folding free energy, considering folded states when $Q > 0.6$ and $Rg < 7.8$, we obtain -1.80 kcal/mol for the all-atom system and -0.66 kcal/mol for the dual-resolution system; in this case, there is a factor of three difference in the magnitude of the values. Remarkably, the dual-resolution result is closer to the experimental values of -0.7 kcal/mol [285] and -0.76 kcal/mol. [337]

6.4 Discussion

A new dual-resolution hydration approach is tested, whereby the ELBA coarse-grained model for water is used in combination with all-atom molecular models. A unique feature of this method is that no extra scaling factors, healing regions, or virtual sites are required to mix the two levels of resolution.

In previous studies [244], our simplified hydration model yielded predictions that are overall as accurate as those from fully atomistic simulations and experiments. Similarly notable was the finding that the hydration free energy of ELBA water in itself reproduces the experimental value for real water more accurately than most atomistic water models. Overall, these remarkable results are in line with recent work on pure water systems showing ELBA to be as accurate as the best atomistic models in reproducing fundamental properties such as density, diffusion, surface tension, vapor-liquid equilibria, and even the critical point. [242] Regarding a possible explanation for the comparatively high accuracy of ELBA, we believe that an important factor is the magnitude of its permanent dipole moment (2.6 D), which is significantly closer to that of real liquid water (2.95 D [125]) compared to those of standard atomistic models (2.18 D for TIP4P, [184, 204] 2.27 D for SPC, [170] 2.305 D for TIP4P/2005, [5] 2.35 D for SPC/E [184] and TIP3P [204]).

In this chapter, dual-resolution simulations were conducted with ELBA water hydrating typical protein structures modeled with a standard atomistic force field. Folding free energy results obtained were in satisfactory agreements for the β hairpin structure. However, for the α helical structure, the magnitude of the folding free energy obtained from the dual-resolution system was over three times smaller than that from the all-atom system; interestingly, the dual-resolution result was found to be closer to the experimental value. Combining all results together, some disagreement in the behavior of protein systems is expected, due to the differences observed between the all-atom and dual-resolution results for the hydration free energies of the amino acid sidechain analogs; specifically, while the overall accuracy of the simulation approaches is similar, significant variations can be observed for most sidechain analogs in terms of individual values of the hydration free energy from the different models.

Regarding general limitations of the mixing methodology, it is clear that any hydrogen bonding between an atomistic solute and ELBA water is inevitably described at an approximate level. In fact, while the electrostatic interactions between ELBA's dipole and atomistic donors and acceptors are expected to capture some overall features of hydrogen bonding, it is clear that the absence of explicit donor and acceptor sites in ELBA prevents local effects to be represented accurately. An example of the consequences of this limitation was indeed observed in the analysis of the

sidechain-sidechain hydrogen bonds. However, it is also interesting and important to stress that the lack of explicit hydrogen bonding sites in ELBA did not prevent the comparatively accurate prediction of the hydration free energy of the amino acid sidechain analogs, and of the ELBA water itself. From a technical standpoint, it should be noted that the ELBA model and related dual-resolution scheme are currently available only in the LAMMPS simulation program. [1, 275] Most other mainstream packages, such as GROMACS, [140] AMBER, [307] NAMD, [270] or GROMOS, [182] lack the point dipole potential, and related rotational integrator, that ELBA requires; these features could of course be implemented, but major modifications to data structures and core routines would be necessary.

6.5 Conclusions

A novel dual-resolution scheme, which couples the ELBA coarse-grained water model with conventional fully atomistic solutes, was tested. The approach presented is uniquely simple, since the coarse-grained water interacts directly with the atomistic molecules without the need for extra parameters. The methodology is overall capable of reproducing the folding free energy landscape of fundamental protein structures; while the average structure and energetics were consistent with corresponding all-atom calculations, some differences were noticed regarding flexibility and hydrogen bonding between sidechains. Computationally, our hybrid simulations proved up to six times more efficient than standard fully atomistic counterparts, and future work involving the implementation of multistep integration methods could increase this speedup further.

Chapter 7

Concluding remarks and perspective

This thesis presented molecular dynamics simulation work related to biomembrane systems. Firstly, shown in Chapter 3 and Chapter 4, atomistic simulations on lipid bilayers were performed. In general, obtained results have revealed how two key features in the lipid molecular structure, i.e., the head group moieties and the saturation level in hydrocarbon chains) influence the assembled membrane properties. Secondly, work presented in Chapter 5 and Chapter 6 on the ELBA CG water model shows the ability of this model to accurately capture essential physics in response to non-ordinary environmental changes (temperature and pressure), and in mixed atomistic/coarse-grained system as solvent.

In the atomistic bilayer-related work, lamellar vs. nonlamellar lipid composition change was shown to induce lipid bilayer property changes mostly in the two transbilayer lateral pressure and dipole potential profiles. At the same time, structural properties including the average area/volume per lipid, bilayer thickness, were also proportionally related to the changes in composition, but the effects are relatively marginal. More specifically, the lateral pressure profile results suggest that DOPE concentration increases induce a transfer of pressure from the lipid headgroups to the inner hydrocarbon core.

Further, the comparison of saturated vs. unsaturated lipids have shown significant effects in their response to high pressure. Notably, for most properties the effects

are amplified for the more saturated POPC bilayer, which suggest a hypothesis that increased unsaturation in the lipid tails results in a stronger resistance to structural change in response to high pressure.

Based on our findings, further investigations on compositional mechanisms of a range of biomembrane processes — such as passive permeation, membrane binding and insertion, and membrane protein functionality — could be potentially carried out. Moreover, as extensions to the current dual-component membrane model, studies on systems with increased complexity may be conducted to more accurately mimic the real biological membrane. Regarding the high pressure effect on membranes, several important membrane properties such as phase separation are yet to be investigated at the molecular-level by simulations. These features are thought to be also crucial to characterize the response of biological membrane to the pressure increase.

From the methodological viewpoint, a coarse-grained or dual-resolution modelling of the membrane system will be further developed. This is expected to be helpful to study larger-scale problems, such as phase transition and pore formation, that are hard to be addressed with atomistic models.

References

[1] `http://lammps.sandia.gov`.

[2] LAMMPS website, `http://lammps.sandia.gov`, accessed July 9, 2015.

[3] Orsi Group. `http://www.orsi.sems.qmul.ac.uk` (accessed June 10, 2014).

[4] J. L. Abascal and C. Vega. A general purpose model for the condensed phases of water: Tip4p/2005. *J. Chem. Phys.*, 123(23):234505, 2005.

[5] J. L. F. Abascal and C. Vega. A general purpose model for the condensed phases of water: Tip4p/2005. *J. Chem. Phys.*, 123:234505, 2005.

[6] D. J. Adams, E. M. Adams, and G. J. Hills. The computer simulation of polar liquids. *Mol. Phys.*, 38(2):387–400, 1979.

[7] J.-M. I. Alakoskela, T. Söderlund, J. M. Holopainen, and P. K. Kinnunen. Dipole potential and head-group spacing are determinants for the membrane partitioning of pregnanolone. *Molecular pharmacology*, 66(1):161–168, 2004.

[8] E. E. Allen, D. Facciotti, and D. H. Bartlett. Monounsaturated but not polyunsaturated fatty acids are required for growth of the deep-sea bacteriumphotobacterium profundum ss9 at high pressure and low temperature. *Applied and Environmental Microbiology*, 65(4):1710–1720, 1999.

[9] M. P. Allen and D. J. Tildesley. Oxford Science Publications, Oxford, U.K., 1st edition, 1987.

[10] M. P. Allen and D. J. Tildesley. *Computer Simulation of Liquids.* Oxford Science Publications, Oxford, U.K., 1st edition, 1987.

[11] S. J. Allen, A. R. Curran, R. H. Templer, W. Meijberg, and P. J. Booth. Controlling the folding efficiency of an integral membrane protein. *Journal of molecular biology*, 342(4):1293–1304, 2004.

[12] J. R. Allison, K. Boguslawski, F. Fraternali, and W. F. van Gunsteren. A refined, efficient mean solvation force model that includes the interior volume contribution. *J. Phys. Chem. B*, 115:4547–4557, 2011.

[13] J. B. K. And, B. R. Brooks, M. K. Jr, R. M. V. And, and R. W. Pastor. An ab initio study on the torsional surface of alkanes and its effect on molecular simulations of alkanes and a dppc bilayer. *Journal of Physical Chemistry B*, 109(11):5300–11, 2005.

[14] M. I. And and S. A. Simon. Hydration and steric pressures between phospholipid bilayers. *Annual Review of Biophysics and Biomolecular Structure*, 23(1):27, 1994.

[15] S. E. F. And, R. W. Pastor, A. Rojnuckarin, S. Bogusz, and B. R. Brooks. Effect of electrostatic force truncation on interfacial and transport properties of water. *Journal of Physical Chemistry*, 100(42):17011–17020, 2009.

[16] K. Arnold. Biological membranes: A molecular perspective from computation and experiment. *Zeitschrift für Physikalische Chemie*, 202(1-2):297–299, 1997.

[17] G. S. Attard, R. H. Templer, W. S. Smith, A. N. Hunt, and S. Jackowski. Modulation of CTP: phosphocholine cytidylyltransferase by membrane curvature elastic stress. *Proc. Natl. Acad. Sci. U.S.A.*, 97:9032–9036, 2000.

[18] G. S. Ayton, W. G. Noid, and G. A. Voth. Multiscale modeling of biomolecular systems: in serial and in parallel. *Curr. Opin. Struct. Biol.*, 17:192–198, 2007.

[19] L. A. Baez and P. Clancy. Existence of a density maximum in extended simple point charge water. *J. Chem. Phys.*, 101(11):9837–9840, 1994.

[20] P. Ball. Water as an active constituent in cell biology. *Chemical Reviews*, 108(1):74, 2008.

[21] P. Ball. Water as an active constituent in cell biology. *Chem. Rev.*, 108:74–108, 2008.

[22] J. Bartke and R. Hentschke. Phase behavior of the Stockmayer fluid via molecular dynamics simulation. *Phys. Rev. E*, 75:061503, Jun 2007.

[23] D. Bartlett. Pressure effects on in vivo microbial processes. *Biochimica et Biophysica Acta (BBA)-Protein Structure and Molecular Enzymology*, 1595(1):367–381, 2002.

[24] A. Ben-Shaul. *Structure and Dynamics of Membranes*, pages 359–401. Elsevier, Amsterdam, 1995.

[25] W. D. Bennett and D. P. Tieleman. Water defect and pore formation in atomistic and coarse-grained lipid membranes: pushing the limits of coarse graining. *Journal of chemical theory and computation*, 7(9):2981–2988, 2011.

[26] H. Berendsen, J. Grigera, and T. Straatsma. The missing term in effective pair potentials. *J. Phys. Chem.*, 91(24):6269–6271, 1987.

[27] H. J. Berendsen. *Simulating the physical world: hierarchical modeling from quantum mechanics to fluid dynamics*. Cambridge University Press, 2007.

[28] H. J. Berendsen, J. Postma, W. Van Gunsteren, and J. Hermans. Springer, Dordrecht, The Netherlands, 1981.

[29] H. J. Berendsen, J. P. M. Postma, W. F. van Gunsteren, A. DiNola, and J. Haak. Molecular dynamics with coupling to an external bath. *J. Chem. Phys.*, 81(8):3684–3690, 1984.

[30] H. J. Berendsen, D. van der Spoel, and R. van Drunen. Gromacs: a message-passing parallel molecular dynamics implementation. *Computer Physics Communications*, 91(1):43–56, 1995.

[31] H. J. C. Berendsen, J. P. M. Postma, W. F. Van Gunsteren, A. Di Nola, and J. R. Haak. Molecular dynamics with coupling to an external bath. *J. Chem. Phys.*, 81:3684–3690, 1984.

[32] J. M. Berg, J. L. Tymoczko, and L. Stryer. Lipids and cell membranes. In *Biochemistry*. W.H.Freeman and Company: New York, 2002.

[33] B. J. Berne and J. E. Straub. Novel methods of sampling phase space in the simulation of biological systems. *Current Opinion in Structural Biology*, 7(2):181–189, 1997.

[34] S. Bevc, C. Junghans, K. Kremer, and M. Praprotnik. Adaptive resolution simulation of salt solutions. *New J. Phys.*, 15(10):105007, 2013.

[35] E. M. Bevers, P. Comfurius, J. L. van Rijn, and H. C. Hemker. Generation of prothrombin-converting activity and the exposure of phosphatidylserine at the outer surface of platelets. *The FEBS Journal*, 122(2):429–436, 1982.

[36] S. M. Bezrukov. Functional consequences of lipid packing stress. *Curr. Opin. Colloid Interface Sci.*, 5:237–243, 2000.

[37] A. V. Botelho, N. J. Gibson, R. L. Thurmond, Y. Wang, and M. F. Brown. Conformational energetics of rhodopsin modulated by nonlamellar-forming lipids. *Biochemistry*, 41:6354–6368, 2002.

[38] A. V. Botelho, T. Huber, T. P. Sakmar, and M. F. Brown. Curvature and hydrophobic forces drive oligomerization and modulate activity of rhodopsin in membranes. *Biophysical journal*, 91(12):4464–4477, 2006.

[39] D. Braun, S. Boresch, and O. Steinhauser. Transport and dielectric properties of water and the influence of coarse-graining: Comparing bmw, spc/e, and tip3p models. *J. Chem. Phys.*, 140(6):064107, 2014.

[40] H. Brockman. Dipole potential of lipid membranes. *Chemistry and physics of lipids*, 73(1):57–79, 1994.

[41] B. R. Brooks, R. E. Bruccoleri, B. D. Olafson, D. J. States, S. Swaminathan, and M. Karplus. Charmm: A program for macromolecular energy, minimization, and dynamics calculations. *J. Comput. Chem.*, 4(2):187–217, 1983.

[42] N. J. Brooks. Pressure effects on lipids and bio-membrane assemblies. *IUCrJ*, 1(6):470–477, 2014.

[43] N. J. Brooks, O. Ces, R. H. Templer, and J. M. Seddon. Pressure effects on lipid membrane structure and dynamics. *Chemistry and physics of lipids*, 164(2):89–98, 2011.

[44] A. Brown, I. Skanes, and M. R. Morrow. Pressure-induced ordering in mixed-lipid bilayers. *Physical Review E*, 69(1):011913, 2004.

[45] B. Brügger. Lipidomics: analysis of the lipid composition of cells and subcellular organelles by electrospray ionization mass spectrometry. *Annual review of biochemistry*, 83:79–98, 2014.

[46] G. Bussi, D. Donadio, and M. Parrinello. Canonical sampling through velocity rescaling. *The Journal of chemical physics*, 126(1):014101, 2007.

[47] G. Bussi, F. L. Gervasio, A. Laio, and M. Parrinello. Free-energy landscape for β hairpin folding from combined parallel tempering and metadynamics. *J. Am. Chem. Soc.*, 128(41):13435–13441, 2006.

[48] O. C, V. A, M. AE, and van Gunsteren WF. A biomolecular force field based on the free enthalpy of hydration and solvation: the gromos force-field parameter sets 53a5 and 53a6. *Journal of computational chemistry*, 25(13):1656, 2004.

[49] M. Campbell and S. Farrell. *Biochemistry*. Cengage Learning, 2011.

[50] R. S. Cantor. The lateral pressure profile in membranes: a physical mechanism of general anesthesia. *Biochemistry*, 36(9):2339–2344, 1997.

[51] R. S. Cantor. Lateral pressures in cell membranes: a mechanism for modulation of protein function. *The Journal of Physical Chemistry B*, 101(10):1723–1725, 1997.

[52] R. S. Cantor. Lateral pressures in cell membranes: a mechanism for modulation of protein function. *J. Phys. Chem. B*, 101(10):1723–1725, 1997.

[53] R. S. Cantor. The influence of membrane lateral pressures on simple geometric models of protein conformational equilibria. *Chem. Phys. Lipids*, 101:45–56, 1999.

[54] R. S. Cantor. Lipid composition and the lateral pressure profile in bilayers. *Biophysical journal*, 76(5):2625–39, May 1999.

[55] D. A. Case, T. Darden, H. Gohlke, R. Luo, M. K. Jr, A. Onufriev, C. Simmerling, B. Wang, and R. J. Woods. The amber biomolecular simulation programs. *Journal of Computational Chemistry*, 26(16):1668, 2005.

[56] E. T. Castellana and P. S. Cremer. Solid supported lipid bilayers: From biophysical studies to sensor design. *Surf. Sci. Rep.*, 61(10):429–444, 2006.

[57] G. Cevc and D. Marsh. *Phospholipid Bilayers - Physical Principles and Models*. John Wiley & Sons, New York, first edition, 1987.

[58] G. Cevc and D. Marsh. *Phospholipid bilayers: physical principles and models*. Wiley, 1987.

[59] A. Chandra and T. Ichiye. Dynamical properties of the soft sticky dipole model of water: Molecular dynamics simulations. *J. Chem. Phys.*, 111:2701–2709, 1999.

[60] I. Chandrasekhar, M. Kastenholz, R. D. Lins, C. Oostenbrink, L. D. Schuler, D. P. Tieleman, and W. F. van Gunsteren. A consistent potential energy parameter set for lipids: dipalmitoylphosphatidylcholine as a benchmark of the gromos96 45a3 force field. *Eur Biophys J*, 32(1):67–77, 2003.

[61] M. Chaplin. Do we underestimate the importance of water in cell biology? *Nat. Rev. Mol. Cell Biol.*, 7:861–866, 2006.

[62] P.-L. Chau. New insights into the molecular mechanisms of general anaesthetics. *British journal of pharmacology*, 161(2):288–307, 2010.

[63] J. Chen and W. Im. Refinement of nmr structures using implicit solvent and advanced sampling techniques. *Journal of the American Chemical Society*, 126(49):16038–47, 2004.

[64] R. Chen, D. Poger, and A. E. Mark. Effect of high pressure on fully hydrated dppc and popc bilayers. *The Journal of Physical Chemistry B*, 115(5):1038–1044, 2010.

[65] Z. Chen and R. Rand. The influence of cholesterol on phospholipid membrane curvature and bending elasticity. *Biophys. J.*, 73(1):267, 1997.

[66] Z. Chen and R. P. Rand. The influence of cholesterol on phospholipid membrane curvature and bending elasticity. *Biophys. J.*, 73:267–276, 1997.

[67] V. Cherezov. Lipidic cubic phase technologies for membrane protein structural studies. *Current Opinion in Structural Biology*, 21(4):559 – 566, 2011. Engineering and design / Membranes.

[68] J. Cladera, I. Martin, J.-M. Ruysschaert, and P. OShea. Characterization of the sequence of interactions of the fusion domain of the simian immunodeficiency virus with membranes role of the membrane dipole potential. *Journal of Biological Chemistry*, 274(42):29951–29959, 1999.

[69] J. Cladera and P. O'Shea. Intramembrane molecular dipoles affect the membrane insertion and folding of a model amphiphilic peptide. *Biophysical journal*, 74(5):2434–2442, 1998.

[70] R. J. Clarke. The dipole potential of phospholipid membranes and methods for its detection. *Adv. Colloid Interface Sci.*, 89:263–281, 2001.

[71] A. R. Curran, R. H. Templer, and P. J. Booth. Modulation of folding and assembly of the membrane protein bacteriorhodopsin by intermolecular forces within the lipid bilayer. *Biochemistry*, 38(29):9328–9336, 1999.

[72] I. Daniel, P. Oger, and R. Winter. Origins of life and biochemistry under high-pressure conditions. *Chemical Society Reviews*, 35(10):858–875, 2006.

[73] T. Darden, D. York, and L. Pedersen. Particle mesh ewald - An Nlog(N) method for Ewald sums in large systems. *J. Chem. Phys.*, 98:10089–10092, 1993.

[74] T. Darden, D. York, and L. Pedersen. Particle mesh ewald: An n log (n) method for ewald sums in large systems. *The Journal of chemical physics*, 98(12):10089–10092, 1993.

[75] L. Darré, M. R. Machado, P. D. Dans, F. E. Herrera, and S. Pantano. Another coarse grain model for aqueous solvation: Wat four? *J. Chem. Theory Comput.*, 6(12):3793–3807, 2010.

[76] L. Darré, M. R. Machado, and S. Pantano. Coarse-grained models of water. *WIREs: Comput. Mol. Sci.*, 2(6):921–930, 2012.

[77] L. Darré, A. Tek, M. Baaden, and S. Pantano. Mixing atomistic and coarse grain solvation models for md simulations: let wt4 handle the bulk. *J. Chem. Theory Comput.*, 8(10):3880–3894, 2012.

[78] D. H. de Jong, C. A. Lopez, and S. J. Marrink. Molecular view on protein sorting into liquid-ordered membrane domains mediated by gangliosides and lipid anchors. *Faraday discussions*, 161:347–363, 2013.

[79] S. W. de Leeuw, J. W. Perram, and E. R. Smith. Computer simulation of the static dielectric constant of systems with permanent electric dipoles. *Annu. Rev. Phys. Chem.*, 37:245–270, 1986.

[80] A. H. de Vries, A. E. Mark, and S. J. Marrink. The binary mixing behavior of phospholipids in a bilayer: A molecular dynamics study. *J. Phys. Chem. B*, 108:2454–2463, 2004.

[81] P. De Weer. A century of thinking about cell membranes. *Annual review of physiology*, 62(1):919–926, 2000.

[82] M. Dékány Fraňová, I. Vattulainen, and O. Samuli Ollila. Can pyrene probes be used to measure lateral pressure profiles of lipid membranes? perspective through atomistic simulations. *Biochimica et Biophysica Acta (BBA)-Biomembranes*, 1838(5):1406–1411, 2014.

[83] M. Deleu, J. M. Crowet, M. N. Nasir, and L. Lins. Complementary biophysical tools to investigate lipid specificity in the interaction between bioactive molecules and the plasma membrane: A review. *Biochimica et Biophysica Acta (BBA) - Biomembranes*, 1838(12):3171–3190, 2014.

[84] E. F. DeLong and A. A. Yayanos. Adaptation of the membrane lipids of a deep-sea bacterium to changes in hydrostatic pressure. *Science*, 228(4703):1101–1103, 1985.

[85] M. Deserno and C. Holm. How to mesh up ewald sums. i. a theoretical and numerical comparison of various particle mesh routines. *The Journal of chemical physics*, 109(18):7678–7693, 1998.

[86] A. H. Dewald, J. C. Hodges, and L. Columbus. Physical determinants of¡ i¿ β¡/i¿-barrel membrane protein folding in lipid vesicles. *Biophysical journal*, 100(9):2131–2140, 2011.

[87] N. Di Pasquale, D. Marchisio, and P. Carbone. Mixing atoms and coarse-grained beads in modelling polymer melts. *J. Chem. Phys.*, 137(16):164111, 2012.

[88] C. J. Dickson, B. D. Madej, ge A. Skjevik, R. M. Betz, K. Teigen, I. R. Gould, and R. C. Walker. Lipid14: The amber lipid force field. *Journal of chemical theory and computation*, 10(2):865, 2014.

[89] K. A. Dill, T. M. Truskett, V. Vlachy, and B. Hribar-Lee. Modeling water, the hydrophobic effect, and ion solvation. *Annu. Rev. Biophys. Biomol. Struct.*, 34:173–199, 2005.

[90] W. Ding, M. Palaiokostas, and M. Orsi. Stress testing the elba water model. *Mol. Simulat.*, 42(4):337–346, 2016.

[91] W. Ding, M. Palaiokostas, and M. Orsi. Stress testing the elba water model. *Molecular Simulation*, 42(4):337–346, 2016.

[92] W. Ding, M. Palaiokostas, W. Wang, and M. Orsi. Effects of lipid composition on bilayer membranes quantified by all-atom molecular dynamics. *The Journal of Physical Chemistry B*, 119(49):15263–15274, 2015.

[93] A. R. Dinner, T. Lazaridis, and M. Karplus. Understanding β-hairpin formation. *Proc. Natl. Acad. Sci. U.S.A.*, 96(16):9068–9073, 1999.

[94] R. C. Dougherty and L. N. Howard. Equilibrium structural model of liquid water: evidence from heat capacity, spectra, density, and other properties. *J. Chem. Phys.*, 109(17):7379–7393, 1998.

[95] W. Dowhan and M. Bogdanov. Functional roles of lipids in membranes. *New comprehensive biochemistry*, 36:1–35, 2002.

[96] J. Dreyer, C. Zhang, E. Ippoliti, and P. Carloni. Role of the membrane dipole potential for proton transport in gramicidin a embedded in a dmpc bilayer. *Journal of chemical theory and computation*, 9(8):3826–3831, 2013.

[97] S. R. Durell, B. R. Brooks, and A. Ben-Naim. Solvent-induced forces between two hydrophilic groups. *J. Phys. Chem.*, 98(8):2198–2202, 1994.

[98] D. J. Earl and M. W. Deem. Parallel tempering: theory, applications, and new perspectives. *Physical Chemistry Chemical Physics Pccp*, 7(23):3910–6, 2005.

[99] E. Egberts and H. J. C. Berendsen. Molecular dynamics simulation of a smectic liquid crystal with atomic detail. *The Journal of Chemical Physics*, 89(6):3718–3732, 1988.

[100] M. Elimelech and W. A. Phillip. The future of seawater desalination: energy, technology, and the environment. *Science*, 333(6043):712–717, 2011.

[101] E. Fahy, S. Subramaniam, H. A. Brown, C. K. Glass, A. H. Merrill, R. C. Murphy, C. R. Raetz, D. W. Russell, Y. Seyama, W. Shaw, et al. A comprehensive classification system for lipids. *Journal of lipid research*, 46(5):839–862, 2005.

[102] C. J. Fennell and J. D. Gezelter. On the structural and transport properties of the soft sticky dipole and related single-point water models. *J. Chem. Phys.*, 120(19):9175–9184, 2004.

[103] C. J. Fennell and J. D. Gezelter. Computational free energy studies of a new ice polymorph which exhibits greater stability than ice ih. *J. Chem. Theory Comput.*, 1:662–667, 2005.

[104] A. Z. Fernandis and M. R. Wenk. Membrane lipids as signaling molecules. *Current opinion in lipidology*, 18(2):121–128, 2007.

[105] A. M. Ferrenberg and R. H. Swendsen. Optimized monte carlo data analysis. *Phys. Rev. Lett.*, 63(12):1195–1198, 1989.

[106] A. Filippov, G. Orädd, and G. Lindblom. The effect of cholesterol on the lateral diffusion of phospholipids in oriented bilayers. *Biophysical journal*, 84(5):3079–3086, 2003.

[107] D. Fincham. Leapfrog rotational algorithms for linear molecules. *Mol. Simul.*, 11:79–89, 1993.

[108] R. F. Flewelling and W. L. Hubbell. The membrane dipole potential in a total membrane potential model. applications to hydrophobic ion interactions with membranes. *Biophysical journal*, 49(2):541–552, 1986.

[109] H. Flyvbjerg and H. G. Petersen. Error estimates on averages of correlated data. *J. Chem. Phys.*, 91(1):461–466, 1989.

[110] N. Foloppe and A. D. MacKerell Jr. All-atom empirical force field for nucleic acids: I. parameter optimization based on small molecule and condensed phase macromolecular target data. *Journal of computational chemistry*, 21(2):86–104, 2000.

[111] S. Funamoto, K. Nam, T. Kimura, A. Murakoshi, Y. Hashimoto, K. Niwaya, S. Kitamura, T. Fujisato, and A. Kishida. The use of high-hydrostatic pressure treatment to decellularize blood vessels. *Biomaterials*, 31(13):3590–3595, 2010.

[112] H. C. Gaede and K. Gawrisch. Lateral diffusion rates of lipid, water, and a hydrophobic drug in a multilamellar liposome. *Biophysical journal*, 85(3):1734–1740, 2003.

[113] A. E. Garca and K. Y. Sanbonmatsu. -helical stabilization by side chain shielding of backbone hydrogen bonds. *Proceedings of the National Academy of Sciences of the United States of America*, 99(5):2782–7, 2002.

[114] L. P. Gaspar, A. C. Silva, A. M. Gomes, M. S. Freitas, A. P. A. Bom, W. D. Schwarcz, J. Mestecky, M. J. Novak, D. Foguel, and J. L. Silva. Hydrostatic pressure induces the fusion-active state of enveloped viruses. *Journal of Biological Chemistry*, 277(10):8433–8439, 2002.

[115] K. Gawrisch and L. L. Holte. Nmr investigations of non-lamellar phase promoters in the lamellar phase state. *Chemistry and physics of lipids*, 81(2):105–116, 1996.

[116] K. Gawrisch, V. A. Parsegian, D. A. Hajduk, M. W. Tate, S. M. Gruner, N. L. Fuller, and R. P. Rand. Energetics of a hexagonal-lamellar-hexagonal-phase transition sequence in dioleoylphosphatidylethanolamine membranes. *Biochemistry*, 31(11):2856–2864, 1992.

[117] K. Gawrisch, D. Ruston, J. Zimmerberg, V. A. Parsegian, R. P. Rand, and N. Fuller. Membrane dipole potentials, hydration forces, and the ordering of water at membrane surfaces. *Biophys. J.*, 61:1213–1223, 1992.

[118] T. Ghosh, A. E. García, and S. Garde. Molecular dynamics simulations of pressure effects on hydrophobic interactions. *J. Am. Chem. Soc.*, 123(44):10997–1003, Nov. 2001.

[119] A. Glättli, X. Daura, and W. F. Van Gunsteren. Derivation of an improved simple point charge model for liquid water: Spc/a and spc/l. *J. Chem. Phys.*, 116(22):9811–9828, 2002.

[120] Z. Gombos, H. Wada, E. Hideg, and N. Murata. The unsaturation of membrane lipids stabilizes photosynthesis against heat stress. *Plant Physiology*, 104(2):563–567, 1994.

[121] H. C. Gonzalez, L. Darré, and S. Pantano. Transferable mixing of atomistic and coarse-grain water models. *J. Phys. Chem. B*, 117:14438–14448, 2013.

[122] A. I. Greenwood, S. Tristram-Nagle, and J. F. Nagle. Partial molecular volumes of lipids and cholesterol. *Chem. Phys. Lip.*, 143(12):1 – 10, 2006.

[123] S. M. Gruner. Intrinsic curvature hypothesis for biomembrane lipid composition: a role for nonbilayer lipids. *Proc. Natl. Acad. Sci. U.S.A.*, 82:3665–3669, 1985.

[124] S. M. Gruner, M. Tate, G. Kirk, P. So, D. Turner, D. Keane, C. Tilcock, and P. Cullis. X-ray diffraction study of the polymorphic behavior of n-methylated dioleoylphosphatidylethanolamine. *Biochemistry*, 27(8):2853–2866, 1988.

[125] A. V. Gubskaya and P. G. Kusalik. The total molecular dipole moment for liquid water. *J. Chem. Phys.*, 117:5290–5302, 2002.

[126] G. Guevara-Carrion, J. Vrabec, and H. Hasse. Prediction of self-diffusion coefficient and shear viscosity of water and its binary mixtures with methanol and ethanol by molecular simulation. *J. Chem. Phys.*, 134(7):074508, 2011.

[127] B. Guillot. A reappraisal of what we have learnt during three decades of computer simulations on water. *J. Mol. Liq.*, 101(1):219–260, 2002.

[128] B. Guillot. A reappraisal of what we have learnt during three decades of computer simulations on water. *J. Mol. Liq.*, 101:219–260, 2002.

[129] A. A. Gurtovenko and I. Vattulainen. Membrane potential and electrostatics of phospholipid bilayers with asymmetric transmembrane distribution of anionic lipids. *J. Phys. Chem. B*, 112:4629–4634, 2008.

[130] K. R. Hadley and C. McCabe. Coarse-grained molecular models of water: a review. *Mol. Simul.*, 38:671–681, 2012.

[131] B. Hafskjold and T. Ikeshoji. Microscopic pressure tensor for hard-sphere fluids. *Physical Review E*, 66(1 Pt 1):011203, 2002.

[132] C. V. Hague, A. D. Postle, G. S. Attard, and M. K. Dymond. Cell cycle dependent changes in membrane stored curvature elastic energy: evidence from lipidomic studies. *Faraday Discuss.*, 161:481–497, 2013.

[133] W. Han and K. Schulten. Further optimization of a hybrid united-atom and coarse-grained force field for folding simulations: Improved backbone hydration and interactions between charged side chains. *J. Chem. Theory Comput.*, 8(11):4413–4424, 2012.

[134] W. Han, C.-K. Wan, F. Jiang, and Y.-D. Wu. Pace force field for protein simulations. 1. full parameterization of version 1 and verification. *J. Chem. Theory Comput.*, 6(11):3373–3389, 2010.

[135] A. Harasima. Molecular theory of surface tension. *Adv. Chem. Phys.*, 1:203–237, 1958.

[136] K. R. Harris and P. J. Newitt. Self-diffusion of water at low temperatures and high pressure. *J. Chem. Eng. Data*, 42(2):346–348, 1997.

[137] S. C. Harvey, R. K. Z. Tan, and T. E. Cheatham III. The flying ice cube: Velocity rescaling in molecular dynamics leads to violation of energy equipartition. *J. Comput. Chem.*, 19:726–740, 1998.

[138] X. He, W. Shinoda, R. DeVane, and M. L. Klein. Exploring the utility of coarse-grained water models for computational studies of interfacial systems. *Mol. Phys.*, 108:2007–2020, 2010.

[139] B. Hess, H. Bekker, H. J. Berendsen, J. G. Fraaije, et al. Lincs: a linear constraint solver for molecular simulations. *Journal of computational chemistry*, 18(12):1463–1472, 1997.

[140] B. Hess, C. Kutzner, D. van der Spoel, and E. Lindahl. Gromacs 4: Algorithms for highly efficient, load-balanced, and scalable molecular simulation. *J. Chem. Theory Comput.*, 4:435–447, 2008.

[141] S. Hladky and D. Haydon. Membrane conductance and surface potential. *Biochimica et Biophysica Acta (BBA)-Biomembranes*, 318(3):464–468, 1973.

[142] R. W. Hockney and J. W. Eastwood. *Computer Simulation Using Particles*. CRC Press, New York, 1st edition, 1989.

[143] R. W. Hockney and J. W. Eastwood. *Computer simulation using particles*. CRC Press, 2010.

[144] M. Holz, S. R. Heil, and A. Sacco. Temperature-dependent self-diffusion coefficients of water and six selected molecular liquids for calibration in accurate 1h nmr pfg measurements. *Phys. Chem. Chem. Phys.*, 2(20):4740–4742, 2000.

[145] W. G. Hoover. Canonical dynamics - equilibrium phase-space distributions. *Phys. Rev. A*, 31:1695–1697, 1985.

[146] H. W. Horn, W. C. Swope, J. W. Pitera, J. D. Madura, T. J. Dick, G. L. Hura, and T. Head-Gordon. Development of an improved four-site water model for biomolecular simulations: TIP4P-Ew. *J. Chem. Phys.*, 120:9665–9678, 2004.

[147] H.-W. Huang, H.-M. Lung, B. B. Yang, and C.-Y. Wang. Responses of microorganisms to high hydrostatic pressure processing. *Food Control*, 40:250–259, 2014.

[148] K. Hukushima and K. Nemoto. Exchange monte carlo method and application to spin glass simulations. *Journal of the Physical Society of Japan*, 65(6):1604–1608, 2012.

[149] W. Humphrey, A. Dalke, and K. Schulten. Vmd: visual molecular dynamics. *J. Mol. Graphics*, 14(1):33–38, 1996.

[150] C. L. B. Iii and D. J. Wales. Taking a walk on a landscape. *Science*, 293:612–613, 2001.

[151] H. I. Ingólfsson, C. A. Lopez, J. J. Uusitalo, D. H. Jong, S. M. Gopal, X. Periole, and S. J. Marrink. The power of coarse graining in biomolecular simulations. *WIREs: Comput. Mol. Sci.*, 4:225–248, 2013.

[152] J. H. Irving and J. G. Kirkwood. The statistical mechanical theory of transport processes. iv. the equations of hydrodynamics. *J. Chem. Phys.*, 18:817–829, 1950.

[153] S. Izvekov, M. Parrinello, C. J. Burnham, and G. A. Voth. Effective force fields for condensed phase systems from ab initio molecular dynamics simulation: A new method for force-matching. *J. Chem. Phys.*, 120:10896–10913, 2004.

[154] S. Izvekov and G. A. Voth. Multiscale coarse graining of liquid-state systems. *J. Chem. Phys.*, 123(13):134105, 2005.

[155] S. Izvekov and G. A. Voth. Multiscale coarse graining of liquid-state systems. *J. Chem. Phys.*, 123:134105, 2005.

[156] W. J, W. RM, C. JW, K. PA, and C. DA. Development and testing of a general amber force field. *Journal of computational chemistry*, 25(9):1157, 2004.

[157] J. P. Jambeck and A. P. Lyubartsev. An extension and further validation of an all-atomistic force field for biological membranes. *Journal of chemical theory and computation*, 8(8):2938–2948, 2012.

[158] L. JB, R. B, and K. JB. Update of the cholesterol force field parameters in charmm. *J Phys Chem B.*, 116(1):203–210, 2012.

[159] L. E. Johnson, R. Barnes, T. W. Draxler, B. E. Eichinger, and B. H. Robinson. Dielectric constants of simple liquids: Stockmayer and ellipsoidal fluids. *J. Phys. Chem. B*, 114:8431–8440, 2010.

[160] W. L. Jorgensen, J. Chandrasekhar, J. D. Madura, R. W. Impey, and M. L. Klein. Comparison of simple potential functions for simulating liquid water. *J. Chem. Phys.*, 79(2), 1983.

[161] W. L. Jorgensen and C. Jenson. Temperature dependence of tip3p, spc, and tip4p water from npt monte carlo simulations: Seeking temperatures of maximum density. *J. Comput. Chem.*, 19(10):1179–1186, 1998.

[162] W. L. Jorgensen and J. D. Madura. Temperature and size dependence for monte carlo simulations of tip4p water. *Mol. Phys.*, 56(6):1381–1392, 1985.

[163] M. A. Jr. Empirical force fields for biological macromolecules: overview and issues. *Journal of Computational Chemistry*, 25(13):1584–604, 2004.

[164] K. Kamimura, H. Fuse, O. Takimura, and Y. Yamaoka. Effects of growth pressure and temperature on fatty acid composition of a barotolerant deep-sea bacterium. *Applied and Environmental Microbiology*, 59(3):924–6, 1993.

[165] T. Kamo, T. Handa, and M. Nakano. Lateral pressure change on phase transitions of phosphatidylcholine/diolein mixed membranes. *Colloids and surfaces. B, Biointerfaces*, 104:128–132, 2013.

[166] T. Kamo, M. Nakano, Y. Kuroda, and T. Handa. Effects of an amphipathic α-helical peptide on lateral pressure and water penetration in phosphatidylcholine and monoolein mixed membranes. *J. Phys. Chem. B*, 110:24987–24992, 2006.

[167] M. Karplus and J. A. McCammon. Molecular dynamics simulations of biomolecules. *Nat. Struct. Mol. Biol.*, 9(9):646–652, 2002.

[168] B. Ketterer, B. Neumcke, and P. Läuger. Transport mechanism of hydrophobic ions through lipid bilayer membranes. *J. Membrane Biol.*, 5(3):225–245, 1971.

[169] S. Khalid and P. Bond. Multiscale molecular dynamics simulations of membrane proteins. In L. Monticelli and E. Salonen, editors, *Biomolecular Simulations*, volume 924 of *Methods in Molecular Biology*, pages 635–657. Humana Press: New York, 2013.

[170] K. Kiyohara, K. E. Gubbins, and A. Z. Panagiotopoulos. Phase coexistence properties of polarizable water models. *Mol. Phys.*, 94(5):803–808, 1998.

[171] J. B. Klauda, R. M. Venable, J. A. Freites, J. W. O'Connor, D. J. Tobias, C. Mondragon-Ramirez, I. Vorobyov, A. D. MacKerell, and R. W. Pastor. Update of the CHARMM all-atom additive force field for lipids: Validation on six lipid types. *J. Phys. Chem. B*, 114:7830–7843, 2010.

[172] J. B. Klauda, R. M. Venable, J. A. Freites, J. W. OConnor, D. J. Tobias, C. Mondragon-Ramirez, I. Vorobyov, A. D. MacKerell Jr, and R. W. Pastor. Update of the charmm all-atom additive force field for lipids: validation on six lipid types. *The journal of physical chemistry B*, 114(23):7830–7843, 2010.

[173] J. B. Klauda, R. M. Venable, J. A. Freites, J. W. O'Connor, D. J. Tobias, C. Mondragon-Ramirez, I. Vorobyov, A. D. MacKerell Jr, and R. W. Pastor. Update of the charmm all-atom additive force field for lipids: validation on six lipid types. *J. Phys. Chem. B*, 114(23):7830–7843, 2010.

[174] J. H. Kleinschmidt and L. K. Tamm. Secondary and tertiary structure formation of the β-barrel membrane protein ompa is synchronized and depends on membrane thickness. *Journal of molecular biology*, 324(2):319–330, 2002.

[175] D. Knorr, V. Heinz, and R. Buckow. High pressure application for food biopolymers. *Biochimica et Biophysica Acta (BBA)-Proteins and Proteomics*, 1764(3):619–631, 2006.

[176] A. G. Kohli, P. H. Kierstead, V. J. Venditto, C. L. Walsh, and F. C. Szoka. Designer lipids for drug delivery: From heads to tails. *Journal of Controlled Release*, 190:274–287, 2014.

[177] M. Kranenburg, M. Vlaar, and B. Smit. Simulating induced interdigitation in membranes. *Biophys. J.*, 87:1596–1605, 2004.

[178] N. Kučerka, J. F. Nagle, J. N. Sachs, S. E. Feller, J. Pencer, A. Jackson, and J. Katsaras. Lipid bilayer structure determined by the simultaneous analysis of neutron and x-ray scattering data. *Biophys. J.*, 95(5):2356–2367, 2008.

[179] N. Kučerka, S. Tristram-Nagle, and J. Nagle. Structure of fully hydrated fluid phase lipid bilayers with monounsaturated chains. *J. Membr. Biol.*, 208(3):193–202, 2006.

[180] N. Kučerka, S. Tristram-Nagle, and J. F. Nagle. Structure of fully hydrated fluid phase lipid bilayers with monounsaturated chains. *The Journal of membrane biology*, 208(3):193–202, 2006.

[181] C. V. Kulkarni, O. Ces, R. H. Templer, and J. M. Seddon. Pressure effects on a protein–lipid model membrane. *Soft Matter*, 9(28):6525–6531, 2013.

[182] A.-P. E. Kunz, J. R. Allison, D. P. Geerke, B. A. C. Horta, P. H. Hünenberger, S. Riniker, N. Schmid, and W. F. van Gunsteren. New functionalities in the gromos biomolecular simulation software. *J. Comput. Chem.*, 33(3):340–353, 2012.

[183] M. G. Kurnikova, D. H. Waldeck, and R. D. Coalson. A molecular dynamics study of dielectric friction. *Journal of Chemical Physics*, 105(2):628–638, 1996.

[184] P. G. Kusalik and I. M. Svishchev. The spatial structure in liquid water. *Science*, 265(5176):1219–1221, 1994.

[185] K. Lai, B. Wang, Y. Zhang, and Y. Zhang. High pressure effect on phase transition behavior of lipid bilayers. *Physical Chemistry Chemical Physics*, 14(16):5744–5752, 2012.

[186] F. Lairion and E. A. Disalvo. Effect of phloretin on the dipole potential of phosphatidylcholine, phosphatidylethanolamine, and phosphatidylglycerol monolayers. *Langmuir*, 20(21):9151–9155, 2004.

[187] A. R. Leach. *Molecular Modelling - Principles and Applications*. Prentice Hall, Harlow, second edition, 2001.

[188] E. Lemmon, M. McLinden, and D. Friend. Thermophysical properties of fluid systems. In W. G. Mallard and P. Linstrom, editors, *NIST chemistry webbook, NIST standard reference database*, volume 69. Gaithersburg, MD, 20899, 2011. http://webbook.nist.gov.

[189] P. A. Leventis and S. Grinstein. The distribution and function of phosphatidylserine in cellular membranes. *Annual review of biophysics*, 39:407–427, 2010.

[190] Z. A. Levine, R. M. Venable, M. C. Watson, M. G. Lerner, J.-E. Shea, R. W. Pastor, and F. L. H. Brown. Determination of biomembrane bending moduli in fully atomistic simulations. *J. Am. Chem. Soc.*, 136(39):13582–13585, 2014.

[191] M. Levitt. Protein folding by restrained energy minimization and molecular dynamics. *J. Mol. Biol.*, 170(3):723–764, 1983.

[192] E. Liberman and V. Topaly. Permeability of bimolecular phospholipid membranes for fat-soluble ions. *Biofizika*, 14(3):452–461, 1968.

[193] S. V. Lishchuk, N. P. Malomuzh, and P. V. Makhlaichuk. Contribution of h-bond vibrations to heat capacity of water. *Phys. Lett. A*, 375(27):2656 – 2660, 2011.

[194] Y. Liu and T. Ichiye. Soft sticky dipole potential for liquid water. *J. Phys. Chem.*, 100:2723–2730, 1996.

[195] K. Lohner and E. J. Prenner. Differential scanning calorimetry and x-ray diffraction studies of the specificity of the interaction of antimicrobial peptides with membrane-mimetic systems. *Biochimica Et Biophysica Acta*, 1462(12):141–156, 1999.

[196] C. F. Lopez, S. O. N. And, M. L. Klein, and P. B. Moore. Hydrogen bonding structure and dynamics of water at the dimyristoylphosphatidylcholine lipid bilayer surface from a molecular dynamics simulation. *Journal of Physical Chemistry B*, 108(21):6603–6610, 2004.

[197] M. Luckey. *Membrane structural biology: with biochemical and biophysical foundations*. Cambridge University Press, 2014.

[198] A. P. Lyubartsev and A. L. Rabinovich. Recent development in computer simulations of lipid bilayers. *Soft Matter*, 7:25–39, 2011.

[199] A. D. Mackerell. Empirical force fields for biological macromolecules: Overview and issues. *J. Comput. Chem.*, 25:1584–1604, 2004.

[200] A. D. MacKerell, D. Bashford, M. Bellott, R. L. Dunbrack, J. D. Evanseck, M. J. Field, S. Fischer, J. Gao, H. Guo, S. Ha, D. Joseph-McCarthy, L. Kuchnir, K. Kuczera, F. T. K. Lau, C. Mattos, S. Michnick, T. Ngo, D. T. Nguyen,

B. Prodhom, W. E. Reiher, B. Roux, M. Schlenkrich, J. C. Smith, R. Stote, J. Straub, M. Watanabe, J. Wirkiewicz-Kuczera, D. Yin, and M. Karplus. All-atom empirical potential for molecular modeling and dynamics studies of proteins. *The Journal of Physical Chemistry B*, 102(18):3586–3616, 1998. PMID: 24889800.

[201] A. D. MacKerell, Jr., D. Bashford, M. Bellott, R. Dunbrack Jr., J. Evanseck, M. Field, S. Fischer, J. Gao, H. Guo, S. Ha, and et al. All-atom empirical potential for molecular modeling and dynamics studies of proteins. *J. Phys. Chem. B*, 102:3586–3616, 1998.

[202] B. Maggio. Modulation of phospholipase a2 by electrostatic fields and dipole potential of glycosphingolipids in monolayers. *Journal of lipid research*, 40(5):930–939, 1999.

[203] M. W. Mahoney and W. L. Jorgensen. A five-site model for liquid water and the reproduction of the density anomaly by rigid, nonpolarizable potential functions. *J. Chem. Phys.*, 112(20), 2000.

[204] M. W. Mahoney and W. L. Jorgensen. A five-site model for liquid water and the reproduction of the density anomaly by rigid, nonpolarizable potential functions. *J. Chem. Phys.*, 112:8910–8922, 2000.

[205] S. Manno, Y. Takakuwa, and N. Mohandas. Identification of a functional role for lipid asymmetry in biological membranes: Phosphatidylserine-skeletal protein interactions modulate membrane stability. *Proc. Natl. Acad. Sci. U.S.A.*, 99(4):1943–1948, 2002.

[206] S. J. Marrink, A. H. de Vries, and A. E. Mark. Coarse grained model for semiquantitative lipid simulations. *J. Phys. Chem. B*, 108(2):750–760, 2004.

[207] S.-J. Marrink, H. J. Risselada, S. Yefimov, D. P. Tieleman, and A. H. de Vries. The MARTINI force field: coarse grained model for biomolecular simulations. *J. Phys. Chem. B*, 111:7812–7824, 2007.

[208] D. Marsh. Lateral pressure profile, spontaneous curvature frustration, and the incorporation and conformation of proteins in membranes. *Biophys. J.*, 93(11):3884 – 3899, 2007.

[209] D. Marsh. Lateral pressure profile, spontaneous curvature frustration, and the incorporation and conformation of proteins in membranes. *Biophysical journal*, 93(11):3884–3899, 2007.

[210] D. Marsh. Lateral pressure profile, spontaneous curvature frustration, and the incorporation and conformation of proteins in membranes. *Biophys. J.*, 93:3884–3899, 2007.

[211] D. Marsh. Protein modulation of lipids, and vice-versa, in membranes. *Biochim. Biophys. Acta*, 1778:1545–1575, 2008. Protein Modulation of Membrane Structure.

[212] D. Marsh. Protein modulation of lipids, and vice-versa, in membranes. *Biochimica et Biophysica Acta (BBA)-Biomembranes*, 1778(7):1545–1575, 2008.

[213] L. J. Martin, R. Chao, and B. Corry. Molecular dynamics simulation of the partitioning of benzocaine and phenytoin into a lipid bilayer. *Biophys. Chem.*, 185(0):98 – 107, 2014.

[214] B. Martinac and O. P. Hamill. Gramicidin a channels switch between stretch activation and stretch inactivation depending on bilayer thickness. *Proceedings of the National Academy of Sciences of the United States of America*, 99(7):4308–4312, 2002.

[215] L. Martínez, R. Andrade, E. G. Birgin, and J. M. Martínez. Packmol: A package for building initial configurations for molecular dynamics simulations. *J. Comput. Chem.*, 30(13):2157–2164, 2009.

[216] M. Masella, D. Borgis, and P. Cuniasse. Combining a polarizable force-field and a coarse-grained polarizable solvent model: Application to long dynamics simulations of bovine pancreatic trypsin inhibitor. *J. Comput. Chem.*, 29(11):1707–1724, 2008.

[217] M. Masella, D. Borgis, and P. Cuniasse. Combining a polarizable force-field and a coarse-grained polarizable solvent model. ii. accounting for hydrophobic effects. *J. Comput. Chem.*, 32(12):2664–2678, 2011.

[218] C. McCabe. Coarse-grained molecular models of water: a review. *Molecular simulation*, 38(8-9):671, 2012.

[219] T. P. McMullen and R. N. McElhaney. Physical studies of cholesterol-phospholipid interactions. *Current Opinion in Colloid & Interface Science*, 1(1):83–90, 1996.

[220] F. Meersman, I. Daniel, D. H. Bartlett, R. Winter, R. Hazael, and P. F. Mcmillan. High-pressure biochemistry and biophysics. *Reviews in Mineralogy & Geochemistry*, 75(1):607–648, 2013.

[221] J. Michel, M. Orsi, and J. W. Essex. Prediction of partition coefficients by multiscale hybrid atomic level/coarse-grain simulations. *J. Phys. Chem. B*, 112:657–660, 2008.

[222] S. Miyamoto and P. A. Kollman. Settle: an analytical version of the shake and rattle algorithm for rigid water models. *Journal of computational chemistry*, 13(8):952–962, 1992.

[223] P. Moe and P. Blount. Assessment of potential stimuli for mechano-dependent gating of mscl: effects of pressure, tension, and lipid headgroups. *Biochemistry*, 44(36):12239–12244, 2005.

[224] V. Molinero and E. B. Moore. Water modeled as an intermediate element between carbon and silicon. *J. Phys. Chem. B*, 113(13):4008–4016, 2008.

[225] P. B. Moore, C. F. Lopez, and M. L. Klein. Dynamical properties of a hydrated lipid bilayer from a multinanosecond molecular dynamics simulation. *Biophys. J.*, 81:2484–2494, 2001.

[226] G. P. Moss. Nomenclature of steroids (recommendations 1989). *Pure and Applied Chemistry*, 61(10):1783–1822, 1989.

[227] O. G. Mouritsen. *Life - As a Matter of Fat. The Emerging Science of Lipidomics.* Springer, Berlin, first edition, 2005.

[228] O. G. Mouritsen. *Life-as a matter of fat.* Springer, 2005.

[229] A. Mrozik, Z. Piotrowskaseget, and S. Labuzek. Cytoplasmic bacterial membrane response to environmental perturbations. *Polish Journal of Environmental Studies*, 13(5):487, 2004.

[230] S. I. Mukhin and S. Baoukina. Analytical derivation of thermodynamic characteristics of lipid bilayer from a flexible string model. *Phys. Rev. E*, 71:061918, 2005.

[231] A. Nagarajan, C. Junghans, and S. Matysiak. Multiscale simulation of liquid water using a four-to-one mapping for coarse-graining. *J. Chem. Theory Comput.*, 9:5168–5175, 2013.

[232] J. F. Nagle and S. Tristram-Nagle. Structure of lipid bilayers. *Biochim. Biophys. Acta*, 1469(3):159 – 195, 2000.

[233] M. Neumann. Dipole moment fluctuation formulas in computer simulations of polar systems. *Mol. Phys.*, 50:841–858, 1983.

[234] S. O. Nielsen, C. F. Lopez, G. Srinivas, and M. L. Klein. Coarse grain models and the computer simulation of soft materials. *J. Phys.: Condens. Matter*, 16(15):R481, 2004.

[235] G. O. Nobuhiro and H. Taketomi. Studies on protein folding, unfolding and fluctuations by computer simulation iii. effect of shortrange interactions. *Chemical Biology and Drug Design*, 13(3):445–459, 1979.

[236] T. Norton and D.-W. Sun. Recent advances in the use of high pressure as an effective processing technique in the food industry. *Food and Bioprocess Technology*, 1(1):2–34, 2008.

[237] B. O, E. O, and J. F. Molecular dynamics simulations of a fluid bilayer of dipalmitoylphosphatidylcholine at full hydration, constant pressure, and constant temperature. *Biophys J.*, 72(5):2002–2013, 1997.

[238] K. Olbrich, W. Rawicz, D. Needham, and E. Evans. Water permeability and mechanical strength of polyunsaturated lipid bilayers. *Biophysical Journal*, 79(1):321–327, 2000.

[239] O. S. Ollila, T. Rog, M. Karttunen, and I. Vattulainen. Role of sterol type on lateral pressure profiles of lipid membranes affecting membrane protein functionality: comparison between cholesterol, desmosterol, 7-dehydrocholesterol and ketosterol. *Journal of structural biology*, 159(2):311–323, 2007.

[240] O. S. Ollila and I. Vattulainen. Lateral pressure profiles in lipid membranes: Dependence on molecular composition. *Molecular simulations and biomembranes: from biophysics to function*, (20):26, 2010.

[241] S. Ollila, M. T. Hyvönen, and I. Vattulainen. Polyunsaturation in lipid membranes: dynamic properties and lateral pressure profiles. *J. Phys. Chem. B*, 111(12):3139–3150, 2007.

[242] M. Orsi. Comparative assessment of the ELBA coarse-grained model for water. *Mol. Phys.*, 112:1566–1576, 2014.

[243] M. Orsi. Comparative assessment of the elba coarse-grained model for water. *Molecular Physics*, 112(11):1566–1576, 2014.

[244] M. Orsi, W. Ding, and M. Palaiokostas. Direct mixing of atomistic solutes and coarse-grained water. *J. Chem. Theory Comput.*, 10:4684–4693, 2014.

[245] M. Orsi and J. W. Essex. Chapter 4 passive permeation across lipid bilayers: a literature review. In M. S. P. Sansom and P. C. Biggin, editors, *Molecular Simulations and Biomembranes: From Biophysics to Function*, pages 76–90. The Royal Society of Chemistry, 2010.

[246] M. Orsi and J. W. Essex. Permeability of drugs and hormones through a lipid bilayer: insights from dual-resolution molecular dynamics. *Soft Matter*, 6:3797–3808, 2010.

[247] M. Orsi and J. W. Essex. Permeability of drugs and hormones through a lipid bilayer: insights from dual-resolution molecular dynamics. *Soft Matter*, 6:3797–3808, 2010.

[248] M. Orsi and J. W. Essex. The ELBA force field for coarse-grain modeling of lipid membranes. *PLoS One*, 6:e28637, 2011.

[249] M. Orsi and J. W. Essex. The elba force field for coarse-grain modeling of lipid membranes. *PLoS One*, 6(12):e28637, 2011.

[250] M. Orsi and J. W. Essex. The elba force field for coarse-grain modeling of lipid membranes. *PLoS ONE*, 6(12):e28637, 12 2011.

[251] M. Orsi and J. W. Essex. Physical properties of mixed bilayers containing lamellar and nonlamellar lipids: insights from coarse-grain molecular dynamics simulations. *Faraday Discussions*, 161:249–272, 2013.

[252] M. Orsi, D. Y. Haubertin, W. E. Sanderson, and J. W. Essex. A quantitative coarse-grain model for lipid bilayers. *J. Phys. Chem. B*, 112:802–815, 2008.

[253] M. Orsi, D. Y. Haubertin, W. E. Sanderson, and J. W. Essex. A quantitative coarse-grain model for lipid bilayers. *J. Phys. Chem. B*, 112:802–815, 2008.

[254] M. Orsi, J. Michel, and J. W. Essex. Coarse-grain modelling of dmpc and dopc lipid bilayers. *J. Phys.: Condens. Matter*, 22(15):155106, 2010.

[255] M. Orsi, J. Michel, and J. W. Essex. Coarse-grain modelling of DMPC and DOPC lipid bilayers. *J. Phys.: Condens. Matter*, 22:155106, 2010.

[256] M. Orsi, M. G. Noro, and J. W. Essex. Dual-resolution molecular dynamics simulation of antimicrobials in biomembranes. *J. R. Soc. Interface*, 8:826–841, 2011.

[257] M. Orsi, M. G. Noro, and J. W. Essex. Dual-resolution molecular dynamics simulation of antimicrobials in biomembranes. *J. R. Soc. Interface*, 8:826–841, 2011.

[258] M. Orsi, W. Sanderson, and J. W. Essex. Coarse-grain modelling of lipid bilayers: a literature review. In M. G. Hicks and C. Kettner, editors, *Molecular Interactions - Bringing Chemistry to Life*, pages 185–205. Beilstein-Institut: Frankfurt, 2007.

[259] M. Orsi, W. Sanderson, and J. W. Essex. *Molecular Interactions - Bringing Chemistry to Life*, pages 85–205. Beilstein-Institut, Frankfurt, Germany, 2007.

[260] M. Orsi, W. E. Sanderson, and J. W. Essex. Permeability of small molecules through a lipid bilayer: a multiscale simulation study. *J. Phys. Chem. B*, 113:12019–12029, 2009.

[261] J. Pan, S. Tristram-Nagle, N. Kučerka, and J. F. Nagle. Temperature dependence of structure, bending rigidity, and bilayer interactions of dioleoylphosphatidylcholine bilayers. *Biophys. J.*, 94(1):117–124, 2008.

[262] J. Pan, S. Tristram-Nagle, N. Kučerka, and J. F. Nagle. Temperature dependence of structure, bending rigidity, and bilayer interactions of dioleoylphosphatidylcholine bilayers. *Biophys. J.*, 94:117–124, 2008.

[263] M. Parrinello and A. Rahman. Polymorphic transitions in single crystals: A new molecular dynamics method. *Journal of Applied physics*, 52(12):7182–7190, 1981.

[264] D. L. Parton, J. W. Klingelhoefer, and M. S. P. Sansom. Aggregation of model membrane proteins, modulated by hydrophobic mismatch, membrane curvature, and protein class. *Biophys. J.*, 101:691–699, 2011.

[265] D. Paschek. Temperature dependence of the hydrophobic hydration and interaction of simple solutes: An examination of five popular water models. *J. Chem. Phys*, 120(14):6674–6690, 2004.

[266] M. Patra. Lateral pressure profiles in cholesterol–DPPC bilayers. *Eur. Biophys. J.*, 35(1):79–88, 2005.

[267] E. Perozo and D. C. Rees. Structure and mechanism in prokaryotic mechanosensitive channels. *Current opinion in structural biology*, 13(4):432–442, 2003.

[268] J. Perram, H. Petersen, and S. D. Leeuw. An algorithm for the simulation of condensed matter which grows as the 3/2 power of the number of particles. *Molecular Physics*, 65(4):875–893, 1988.

[269] B. S. Perrin Jr., A. J. Sodt, M. L. Cotten, and R. W. Pastor. The curvature induction of surface-bound antimicrobial peptides piscidin 1 and piscidin 3 varies with lipid chain length. *J. Membr. Biol.*, 248(3):455–467, 2015.

[270] J. C. Phillips, R. Braun, W. Wang, J. Gumbart, E. Tajkhorshid, E. Villa, C. Chipot, R. D. Skeel, L. Kale, and K. Schulten. Scalable molecular dynamics with namd. *J. Comput. Chem.*, 26(16):1781–1802, 2005.

[271] A. Picard and I. Daniel. Pressure as an environmental parameter for microbial life - a review. *Biophysical Chemistry*, 183:30 – 41, 2013.

[272] A. D. Pickar and R. Benz. Transport of oppositely charged lipophilic probe ions in lipid bilayer membranes having various structures. *J. Membr. Biol.*, 44:353–376, 1978.

[273] T. J. Piggot, A. Pineiro, and S. Khalid. Molecular dynamics simulations of phosphatidylcholine membranes: a comparative force field study. *Journal of chemical theory and computation*, 8(11):4593–4609, 2012.

[274] S. Plimpton. Fast parallel algorithms for short-range molecular dynamics. *J. Comput. Phys.*, 117(1):1–19, 1995.

[275] S. Plimpton. Fast parallel algorithms for short-range molecular dynamics. *J. Comput. Phys.*, 117:1–19, 1995.

[276] D. Poger, W. F. van Gunsteren, and A. E. Mark. A new force field for simulating phosphatidylcholine bilayers. *J. Comput. Chem.*, 31:1117–1125, 2010.

[277] A. A. Polyansky, P. E. Volynsky, D. E. Nolde, A. S. Arseniev, and R. G. Efremov. Role of lipid charge in organization of water/lipid bilayer interface: Insights via computer simulations. *J. Phys. Chem. B*, 109:15052–15059, 2005.

[278] D. W. Pond, G. A. Tarling, and D. J. Mayor. Hydrostatic pressure and temperature effects on the membranes of a seasonally migrating marine copepod. *Plos One*, 9(10):e111043–e111043, 2013.

[279] M. Praprotnik, L. Delle Site, and K. Kremer. Adaptive resolution molecular-dynamics simulation: Changing the degrees of freedom on the fly. *J. Chem. Phys.*, 123, 2005.

[280] M. Praprotnik, L. Delle Site, and K. Kremer. A macromolecule in a solvent: Adaptive resolution molecular dynamics simulation. *J. Chem. Phys.*, 126:134902, 2007.

[281] M. R. Prausnitz and R. Langer. Transdermal drug delivery. *Nature Biotechnol.*, 26(11):1261–1268, 2008.

[282] D. J. Price and C. L. Brooks III. A modified tip3p water potential for simulation with ewald summation. *J. Chem. Phys.*, 121(20):10096–10103, 2004.

[283] S. Price, A. Stone, and M. Alderton. Explicit formulae for the electrostatic energy, forces and torques between a pair of molecules of arbitrary symmetry. *Mol. Phys.*, 52(4):987–1001, 1984.

[284] S. Purushothaman, P. Cicuta, O. Ces, and N. J. Brooks. Influence of high pressure on the bending rigidity of model membranes. *The Journal of Physical Chemistry B*, 119(30):9805–9810, 2015.

[285] L. Qiu, S. A. Pabit, A. E. Roitberg, and S. J. Hagen. Smaller and faster: the 20-residue trp-cage protein folds in 4 s. *J. Am. Chem. Soc.*, 124(44):12952–12953, 2002.

[286] G. Raabe and R. J. Sadus. Molecular dynamics simulation of the dielectric constant of water: The effect of bond flexibility. *J. Chem. Phys.*, 134(23):234501, 2011.

[287] G. Raabe and R. J. Sadus. Molecular dynamics simulation of the effect of bond flexibility on the transport properties of water. *J. Chem. Phys.*, 137(10):104512, 2012.

[288] M. Raghunathan, Y. Zubovski, R. M. Venable, R. W. Pastor, J. F. Nagle, and S. Tristram-Nagle. Structure and elasticity of lipid membranes with genistein and daidzein bioflavinoids using x-ray scattering and md simulations. *J. Phys. Chem. B*, 116(13):3918–3927, 2012.

[289] R. Rand and N. Fuller. Structural dimensions and their changes in a reentrant hexagonal-lamellar transition of phospholipids. *Biophys. J.*, 66(6):2127, 1994.

[290] R. Rand, N. Fuller, S. Gruner, and V. Parsegian. Membrane curvature, lipid segregation, and structural transitions for phospholipids under dual-solvent stress. *Biochemistry*, 29(1):76–87, 1990.

[291] R. Rand and V. Parsegian. Hydration forces between phospholipid bilayers. *Biochim. Biophys. Acta*, 988(3):351–376, 1989.

[292] D. C. Rapaport. *The art of molecular dynamics simulation*. Cambridge university press, 2004.

[293] W. Rawicz, K. Olbrich, T. McIntosh, D. Needham, and E. Evans. Effect of chain length and unsaturation on elasticity of lipid bilayers. *Biophysical journal*, 79(1):328–339, 2000.

[294] A. S. Reddy, D. T. Warshaviak, and M. Chachisvilis. Effect of membrane tension on the physical properties of dopc lipid bilayer membrane. *Biochim. Biophys. Acta*, 1818(9):2271 – 2281, 2012.

[295] J. Rice. *Mathematical statistics and data analysis*. Cengage Learning, 2006.

[296] S. Riniker, J. R. Allison, and W. F. van Gunsteren. On developing coarse-grained models for biomolecular simulation: a review. *Phys. Chem. Chem. Phys.*, 14(36):12423–12430, 2012.

[297] S. Riniker, A. P. Eichenberger, and W. F. van Gunsteren. Solvating atomic level fine-grained proteins in supra-molecular level coarse-grained water for molecular dynamics simulations. *Eur. Biophys. J.*, 41:647–661, 2012.

[298] S. Riniker, A. P. Eichenberger, and W. F. van Gunsteren. Structural effects of an atomic-level layer of water molecules around proteins solvated in supra-molecular coarse-grained water. *J. Phys. Chem. B*, 116(30):8873–8879, 2012.

[299] S. Riniker and W. F. van Gunsteren. A simple, efficient polarizable coarse-grained water model for molecular dynamics simulations. *The Journal of chemical physics*, 134(8):084110, 2011.

[300] M. Ritz, J. Tholozan, M. Federighi, and M. Pilet. Physiological damages of listeria monocytogenes treated by high hydrostatic pressure. *International Journal of Food Microbiology*, 79(1):47–53, 2002.

[301] N. Rivalain, J. Roquain, and G. Demazeau. Development of high hydrostatic pressure in biosciences: Pressure effect on biological structures and potential applications in biotechnologies. *Biotechnology advances*, 28(6):659–672, 2010.

[302] M. Roca, B. Messer, D. Hilvert, and A. Warshel. On the relationship between folding and chemical landscapes in enzyme catalysis. *Proceedings of the National Academy of Sciences of the United States of America*, 105(37):13877–82, 2008.

[303] T. I. Rokitskaya, E. A. Kotova, and Y. N. Antonenko. Membrane dipole potential modulates proton conductance through gramicidin channel: movement of negative ionic defects inside the channel. *Biophysical journal*, 82(2):865–873, 2002.

[304] J.-P. Ryckaert, G. Ciccotti, and H. J. Berendsen. Numerical integration of the cartesian equations of motion of a system with constraints: molecular dynamics of n-alkanes. *J. Comput. Phys.*, 23:327–341, 1977.

[305] A. J. Rzepiela, M. Louhivuori, C. Peter, and S. J. Marrink. Hybrid simulations: combining atomistic and coarse-grained force fields using virtual sites. *Phys. Chem. Chem. Phys.*, 13(22):10437–10448, 2011.

[306] E. Sackmann. Supported membranes: scientific and practical applications. *Science*, 271(5245):43–48, 1996.

[307] R. Salomon-Ferrer, D. A. Case, and R. C. Walker. An overview of the amber biomolecular simulation package. *WIREs: Comput. Mol. Sci.*, 3(2):198–210, 2013.

[308] R. SalomonFerrer, D. A. Case, and R. C. Walker. An overview of the amber biomolecular simulation package. *Wires Computational Molecular Science*, 3(2):198–210, 2013.

[309] A. Samad, Y. Sultana, and M. Aqil. Liposomal drug delivery systems: an update review. *Current drug delivery*, 4(4):297–305, 2007.

[310] J. Schamberger and R. J. Clarke. Hydrophobic ion hydration and the magnitude of the dipole potential. *Biophysical journal*, 82(6):3081–3088, 2002.

[311] J. Schamberger and R. J. Clarke. Hydrophobic ion hydration and the magnitude of the dipole potential. *Biophys. J.*, 82(6):3081 – 3088, 2002.

[312] H. A. Scheraga, M. Khalili, and A. Liwo. Protein-folding dynamics: Overview of molecular simulation techniques. *Annual Review of Physical Chemistry*, 58(1):57, 2007.

[313] T. Schneider and E. Stoll. Molecular-dynamics study of a three-dimensional one-component model for distortive phase transitions. *Phys. Rev. B*, 17(3):1302, 1978.

[314] T. Schneider and E. Stoll. Molecular-dynamics study of a three-dimensional one-component model for distortive phase transitions. *Phys. Rev. B*, 17:1302–1322, Feb 1978.

[315] L. D. Schuler, X. Daura, and W. F. V. Gunsteren. An improved gromos96 force field for aliphatic hydrocarbons in the condensed phase. *Journal of Computational Chemistry*, 22(11):1205–1218, 2001.

[316] A. M. Seddon, M. Lorch, O. Ces, R. H. Templer, F. Macrae, and P. J. Booth. Phosphatidylglycerol lipids enhance folding of an α helical membrane protein. *Journal of molecular biology*, 380(3):548–556, 2008.

[317] J. M. Seddon and R. H. Templer. Polymorphism of lipid-water systems. *Handbook of Biological Physics*, 1:97–160, 1995.

[318] G. Shearman, G. Attard, A. Hunt, S. Jackowski, M. Baciu, S. Sebai, X. Mulet, J. Clarke, R. Law, C. Plisson, et al. Using membrane stress to our advantage. *Biochemical Society Transactions*, 35(3):498–501, 2007.

[319] G. Shearman, O. Ces, R. Templer, and J. Seddon. Inverse lyotropic phases of lipids and membrane curvature. *Journal of Physics: Condensed Matter*, 18(28):S1105, 2006.

[320] P. Sherwood, B. R. Brooks, and M. S. P. Sansom. Multiscale methods for macromolecular simulations. *Curr. Opin. Struct. Biol.*, 18:630–640, 2008.

[321] Q. Shi, S. Izvekov, and G. A. Voth. Mixed atomistic and coarse-grained molecular dynamics: simulation of a membrane-bound ion channel. *J. Phys. Chem. B*, 110:15045–15048, 2006.

[322] K. Shinoda, W. Shinoda, T. Baba, and M. Mikami. Comparative molecular dynamics study of ether-and ester-linked phospholipid bilayers. *J. Chem. Phys.*, 121(19):9648–9654, 2004.

[323] R. Shrestha, A. E. Cardenas, R. Elber, and L. J. Webb. Measurement of the membrane dipole electric field in dmpc vesicles using vibrational shifts of p-cyanophenylalanine and molecular dynamics simulations. *J. Phys. Chem. B*, 119(7):2869–2876, 2015.

[324] D. Siegel and R. Epand. The mechanism of lamellar-to-inverted hexagonal phase transitions in phosphatidylethanolamine: implications for membrane fusion mechanisms. *Biophysical journal*, 73(6):3089–3111, 1997.

[325] F. Simonato, S. Campanaro, F. M. Lauro, A. Vezzi, M. D'Angelo, N. Vitulo, G. Valle, and D. H. Bartlett. Piezophilic adaptation: a genomic point of view. *Journal of biotechnology*, 126(1):11–25, 2006.

[326] K. Simons and D. Toomre. Lipid rafts and signal transduction. *Nature reviews Molecular cell biology*, 1(1):31–39, 2000.

[327] S. W. Siu, R. Vácha, P. Jungwirth, and R. A. Böckmann. Biomolecular simulations of membranes: physical properties from different force fields. *The Journal of chemical physics*, 128(12):125103, 2008.

[328] S. W. I. Siu, R. Vacha, P. Jungwirth, and R. A. Bockmann. Biomolecular simulations of membranes: Physical properties from different force fields. *J. Chem. Phys.*, 128:125103, 2008.

[329] I. D. Skanes, J. Stewart, K. M. W. Keough, and M. R. Morrow. Effect of chain unsaturation on bilayer response to pressure. *Physical Review E*, 74:051913, Nov 2006.

[330] A. J. Sodt and R. W. Pastor. Bending free energy from simulation: correspondence of planar and inverse hexagonal lipid phases. *Biophys. J.*, 104(10):2202–2211, 2013.

[331] A. J. Sodt and R. W. Pastor. Molecular modeling of lipid membrane curvature induction by a peptide: more than simply shape. *Biophys. J.*, 106(9):1958–1969, 2014.

[332] J. Sonne, M. . Jensen, F. Y. Hansen, L. Hemmingsen, and G. H. Peters. Reparameterization of all-atom dipalmitoylphosphatidylcholine lipid parameters enables simulation of fluid bilayers at zero tension. *Biophysical Journal*, 92(12):4157–67, 2007.

[333] T. Starke-Peterkovic and R. J. Clarke. Effect of headgroup on the dipole potential of phospholipid vesicles. *Eur. Biophys. J.*, 39(1):103–110, 2009.

[334] T. Starke-Peterkovic, N. Turner, P. L. Else, and R. J. Clarke. Electric field strength of membrane lipids from vertebrate species: membrane lipid composition and Na^+-K^+-ATPase molecular activity. *Am. J. Physiol. Regul. Integr. Comp. Physiol.*, 288(3):R663–R670, 2005.

[335] T. L. Steck and Y. Lange. Cell cholesterol homeostasis: mediation by active cholesterol. *Trends in cell biology*, 20(11):680–687, 2010.

[336] S. D. Stoddard and J. Ford. Numerical experiments on the stochastic behavior of a lennard-jones gas system. *Phys. Rev. A*, 8(3):1504, 1973.

[337] W. W. Streicher and G. I. Makhatadze. Unfolding thermodynamics of trp-cage, a 20 residue miniprotein, studied by differential scanning calorimetry and circular dichroism spectroscopy. *Biochemistry*, 46(10):2876–2880, 2007.

[338] Y. Sugita and Y. Okamoto. Replica-exchange molecular dynamics method for protein folding. *Chemical Physics Letters*, 314(12):141–151, 1999.

[339] S. Suladze, S. Cinar, B. Sperlich, and R. Winter. Pressure modulation of the enzymatic activity of phospholipase a2, a putative membrane-associated pressure sensor. *Journal of the American Chemical Society*, 137(39):12588–12596, 2015.

[340] I. Szleifer, D. Kramer, A. Ben-Shaul, W. M. Gelbart, and S. A. Safran. Molecular theory of curvature elasticity in surfactant films. *J. Chem. Phys.*, 92:6800–6817, 1990.

[341] C. Tanford. *The Hydrophobic Effect: Formation of Micelles and Biological Membranes 2d Ed.* J. Wiley., 1980.

[342] M. Tate, E. Eikenberry, D. Turner, E. Shyamsunder, and S. Gruner. Nonbilayer phases of membrane lipids. *Chemistry and physics of lipids*, 57(2):147–164, 1991.

[343] R. H. Templer, S. J. Castle, A. R. Curran, G. Rumbles, and D. R. Klug. Sensing isothermal changes in the lateral pressure in model membranes using di-pyrenyl phosphatidylcholine. *Faraday Discuss.*, 111:41–53, 1998.

[344] R. H. Templer, S. J. Castle, A. R. Curran, G. Rumbles, and D. R. Klug. Sensing isothermal changes in the lateral pressure in model membranes using di-pyrenyl phosphatidylcholine. *Faraday Discuss.*, 111:41–53, 1999.

[345] R. H. Templer, B. J. Khoo, and J. M. Seddon. Gaussian curvature modulus of an amphiphilic monolayer. *Langmuir*, 14:7427–7434, 1998.

[346] M. Thomas and B. Corry. A computational assessment of the permeability and salt rejection of carbon nanotube membranes and their application to water desalination. *Phil. Trans. R. Soc. A*, 374(2060):20150020, 2016.

[347] D. P. Tieleman, S. J. Marrink, and H. J. Berendsen. A computer perspective of membranes: molecular dynamics studies of lipid bilayer systems. *Biochimica et biophysica acta*, 1331(3):235–70, Nov. 1997.

[348] I. G. Tironi and W. F. Van Gunsteren. A molecular dynamics simulation study of chloroform. *Mol. Phys.*, 83(2):381–403, 1994.

[349] A. Torres-Sánchez, J. M. Vanegas, and M. Arroyo. Examining the mechanical equilibrium of microscopic stresses in molecular simulations. *Physical review letters*, 114(25):258102, 2015.

[350] S. Tristram-Nagle and J. F. Nagle. Lipid bilayers: thermodynamics, structure, fluctuations, and interactions. *Chem. Phys. Lipids*, 127:3–14, 2004.

[351] D. Trzesniak, R. D. Lins, and W. F. van Gunsteren. Protein under pressure: molecular dynamics simulation of the arc repressor. *Proteins: Structure, Function, and Bioinformatics*, 65(1):136–144, 2006.

[352] E. van den Brink-van der Laan, V. Chupin, J. A. Killian, and B. de Kruijff. Small alcohols destabilize the kcsa tetramer via their effect on the membrane lateral pressure. *Biochemistry*, 43(20):5937–5942, 2004.

[353] E. van den Brink-van der Laan, J. A. Killian, and B. de Kruijff. Nonbilayer lipids affect peripheral and integral membrane proteins via changes in the lateral pressure profile. *Biochim. Biophys. Acta*, 1666(1-2):275–88, Nov. 2004.

[354] E. van den Brink-van der Laan, J. A. Killian, and B. de Kruijff. Nonbilayer lipids affect peripheral and integral membrane proteins via changes in the lateral pressure profile. *Biochim. Biophys. Acta*, 1666:275–288, 2004.

[355] W. F. van Gunsteren, D. Bakowies, R. Baron, I. Chandrasekhar, M. Christen, X. Daura, P. Gee, D. P. Geerke, A. Glättli, P. H. Hünenberger, et al. Biomolecular modeling: goals, problems, perspectives. *Angewandte Chemie International Edition*, 45(25):4064–4092, 2006.

[356] G. van Meer, D. R. Voelker, and G. W. Feigenson. Membrane lipids: where they are and how they behave. *Nature reviews. Molecular cell biology*, 9(February):112–124, 2008.

[357] J. M. Vanegas, A. Torres-Sánchez, and M. Arroyo. Importance of force decomposition for local stress calculations in biomembrane molecular simulations. *Journal of chemical theory and computation*, 10(2):691–702, 2014.

[358] K. Vanommeslaeghe, E. Hatcher, C. Acharya, S. Kundu, S. Zhong, J. Shim, E. Darian, O. Guvench, P. Lopes, I. Vorobyov, and A. D. Mackerell. Charmm general force field: A force field for drug-like molecules compatible with the charmm all-atom additive biological force fields. *J. Comput. Chem.*, 31(4):671–690, 2010.

[359] F. Varnik, J. Baschnagel, and K. Binder. Molecular dynamics results on the pressure tensor of polymer films. *J. Chem. Phys.*, 113:4444–4453, 2000.

[360] C. Vega and J. L. Abascal. Simulating water with rigid non-polarizable models: a general perspective. *Phys. Chem. Chem. Phys.*, 13:19663–19688, 2011.

[361] C. Vega, J. L. F. Abascal, M. M. Conde, and J. L. Aragones. What ice can teach us about water interactions: a critical comparison of the performance of different water models. *Faraday Discuss.*, 141:251–276, 2009.

[362] R. M. Venable, A. J. Sodt, B. Rogaski, H. Rui, E. Hatcher, A. D. MacKerell Jr, R. W. Pastor, and J. B. Klauda. CHARMM all-atom additive force field for sphingomyelin: elucidation of hydrogen bonding and of positive curvature. *Biophys. J.*, 107(1):134 – 145, 2014.

[363] L. Verlet. Computer experiments on classical fluids. *Phys. Rev*, 159:98–103, 1967.

[364] G. Vitiello, A. Falanga, M. Galdiero, D. Marsh, S. Galdiero, and G. D'Errico. Lipid composition modulates the interaction of peptides deriving from herpes simplex virus type i glycoproteins b and h with biomembranes. *Biochimica et Biophysica Acta (BBA)-Biomembranes*, 1808(10):2517–2526, 2011.

[365] I. Vorobyov and T. W. Allen. The electrostatics of solvent and membrane interfaces and the role of electronic polarizability. *J. Chem. Phys.*, 132:185101, 2010.

[366] H. Wang, C. Junghans, and K. Kremer. Comparative atomistic and coarse-grained study of water: What do we lose by coarse-graining? *Eur. Phys. J. E*, 28(2):221–229, 2009.

[367] J. M. Wang, R. M. Wolf, J. W. Caldwell, P. A. Kollman, and D. A. Case. Development and testing of a general Amber force field. *J. Comput. Chem.*, 25:1157–1174, 2004.

[368] L. Wang. Measurements and implications of the membrane dipole potential. *Annual review of biochemistry*, 81:615–35, Jan. 2012.

[369] W. Wang, J. Swendsen, and H. Swendsen. Replica monte carlo simulation of spin glasses. *Physical Review Letters*, 57(21):2607, 1986.

[370] D. T. Warshaviak, M. J. Muellner, and M. Chachisvilis. Effect of membrane tension on the electric field and dipole potential of lipid bilayer membrane. *Biochim. Biophys. Acta*, 1808(10):2608–2617, 2011.

[371] A. Warshel. Calculations of chemical processes in solutions. *Journal of Physical Chemistry*, 83(12):1640–1652, 1979.

[372] A. Warshel. Calculations of chemical processes in solutions. *J. Phys. Chem.*, 83:1640–1652, 1979.

[373] T. A. Wassenaar, H. I. Ingólfsson, M. Prieß, S. J. Marrink, and L. V. Schäfer. Mixing martini: Electrostatic coupling in hybrid atomistic–coarse-grained biomolecular simulations. *J. Phys. Chem. B*, 117(13):3516–3530, 2013.

[374] J. B. Willett and J. D. Singer. Another cautionary note about r^2: Its use in weighted least-squares regression analysis. *The American Statistician*, 42(3):236–238, 1988.

[375] G. Wilson, S. P. Rose, and C. F. Fox. The effect of membrane lipid unsaturation on glycoside transport. *Biochemical and biophysical research communications*, 38(4):617–623, 1970.

[376] R. Winter and W. Dzwolak. Exploring the temperature–pressure configurational landscape of biomolecules: from lipid membranes to proteins. *Philosophical Transactions of the Royal Society of London A: Mathematical, Physical and Engineering Sciences*, 363(1827):537–563, 2005.

[377] R. Winter and C. Jeworrek. Effect of pressure on membranes. *Soft Matter*, 5(17):3157–3173, 2009.

[378] Y.-T. Wong, T. W. Clark, J. Shen, and J. A. McCammon. Molecular dynamics simulation of substrate-enzyme interactions in the active site channel of superoxide dismutase. *Molecular Simulation*, 10(2-6):277–289, 1993.

[379] Z. Wu, Q. Cui, and A. Yethiraj. A new coarse-grained model for water: the importance of electrostatic interactions. *J. Phys. Chem. B*, 114(32):10524–10529, 2010.

[380] Z. Wu, Q. Cui, and A. Yethiraj. Driving force for the association of hydrophobic peptides: The importance of electrostatic interactions in coarse-grained water models. *J. Phys. Chem. Lett.*, 2:1794–1798, 2011.

[381] B. Yang, Y. Shi, X. Xia, M. Xi, X. Wang, B. Ji, and J. Meng. Inactivation of foodborne pathogens in raw milk using high hydrostatic pressure. *Food Control*, 28(2):273–278, 2012.

[382] S. O. Yesylevskyy, L. V. Schäfer, D. Sengupta, and S. J. Marrink. Polarizable water model for the coarse-grained martini force field. *PLoS Comput. Biol.*, 6:e1000810, 2010.

[383] R. Zhou. Trp-cage: folding free energy landscape in explicit water. *Proc. Natl. Acad. Sci. U.S.A.*, 100(23):13280–13285, 2003.

[384] R. Zhou. Exploring the protein folding free energy landscape: coupling replica exchange method with P3ME/RESPA algorithm. *J. Mol. Graphics Modell.*, 22(5):451–63, May 2004.

[385] R. Zhou. Replica exchange molecular dynamics method for protein folding simulation. In Y. Bai and R. Nussinov, editors, *Protein Folding Protocols*, volume 350 of *Methods in Molecular Biology*, pages 205–223. Humana Press, New York, 2006.

[386] R. Zhou, B. J. Berne, and R. Germain. The free energy landscape for β hairpin folding in explicit water. *Proc. Natl. Acad. Sci. U.S.A.*, 98(26):14931–14936, 2001.

[387] F. Zhu, E. Tajkhorshid, and K. Schulten. Pressure-induced water transport in membrane channels studied by molecular dynamics. *Biophysical journal*, 83(1):154–160, 2002.

[388] X. Zhuang, J. R. Makover, W. Im, and J. B. Klauda. A systematic molecular dynamics simulation study of temperature dependent bilayer structural properties. *Biochimica et Biophysica Acta (BBA)-Biomembranes*, 1838(10):2520–2529, 2014.